Bentonite bonded moulding sands

New insights in the interplay of heat and mass transport and mechanical properties

KORBINIAN LEONHARD THOMAS SCHIEBEL

Dissertation zur Erlangung des Doktorgrades
an der Fakultät für Geowissenschaften
der Ludwig-Maximilians-Universität München

München 06.03.2018

Erstgutachter: Prof. Dr. Guntram Jordan
Zweitgutachter: Prof. Wolfgang W. Schmahl
Tag der mündlichen Prüfung: 02.07.2018

Abstract

Sand moulded casting is still one of the most efficient and cheapest methods to produce metal parts of complex shapes. Due to their cyclic reusability and low emission of particles and organic compounds during casting, bentonite bonded sands have an excellent environmental performance. Moreover, sands discarded after a maximum of cycles can be reused as raw material for in various applications.

Wet tensile strength testing is a common method to assess the quality of bentonite bonded moulding sands. For wet tensile strength testing, a specimen is first heated from above in order to simulate heat-driven moisture transport induced by the casting process. Then, stress is applied until the specimen ruptures. In the first part of this study, neutron radiography imaging was applied to moulding sands in-situ during heating and wet tensile strength testing in order to investigate the effects of water kinematics on the tensile strength.

Neutron radiography allowed the localization of the rupture plane and the quantitative determination of the local water content with sub-mm resolution. Quantification of the temperature of the rupture plane and of the heat kinematics within the specimen was accomplished by temperature measurements both in-situ and ex-situ. In this way, experimental data correlating the wet tensile strength with the specific conditions of moulding sands at the rupture plane were obtained for the first time.

Series of experiments with different initial sand moisture contents were conducted. The results show that the weakest location within a sand profile can be pinpointed at the interface between evaporation and condensation zone (i.e., at the 100°C isotherm), where water vaporisation starts and the water bridges connecting the sand grains collapse.

During casting, however, the moulding sand undergoes irreversible alterations, which deteriorate its properties. Aim of this work, therefore, was to gain accurate insights into the relation between sand alteration and property change. To this end, the wet tensile strengths of heat pre-treated and cyclically reused sands were related to the kinematics of water within the sand as measured by in-situ neutron radiography and neutron diffraction.

Sands subjected to 22 cycles of drying (T = 120°C) and remoistening (3 wt.%) revealed modifications in smectite lattice spacings and in water release behaviour from smectite interlayers. No significant change of tensile strength, however, was associated with these modifications. Contrarily, sands pre-treated with temperatures as low as 225°C revealed a reduction of tensile strength which was correlated with irreversible modifications of the structural and compositional integrity of the smectites as manifested by substantially altered water kinematics. The results show that cyclic

use of moulding sand has little impact on the sand quality as long as the temperature of the sand remains low. For the practice in foundry, the results imply that a rigorous separation of heat-exposed sand is advantageous.

Sands bonded with sodium- and calcium-bentonite were studies in order to unravel the influence of the exchangeable cation on the binding properties. Changes in tensile strength as well as in heat and mass transport within the sand were investigated. Heat pre-treated Ca- and Na-bentonite bonded sand revealed differences in tensile strength. Although no major differences in the swelling behaviour could be detected, Na-bentonite bonded sands have a better mechanical performance than Ca-bentonite bonded sands both before and after the pre-treatment. The measured changes in tensile strength of both Ca- and Na-bentonite bonded sand correspond well with the irreversible alterations of the smectites.

Contents

List of Figures

Nomenclature

A	Sectional area of the specimen (m^2)
$b(t)$	Correction factor for beam fluctuation
$B1, B2$	Background parameters
c	Full half maximum of the d_{001} reflection (°)
C_s	Specific heat of the moulding sand (kJ/(kgK))
C_w	Specific heat of water (kJ/(kgK))
d_{001}	d-spacing of the 100 lattice planes (Å)
F_g	Weight of the upper sample part (kN/m^2)
F_r	Maximum measured tensile force (kg/m^2)
F_t	Tearing tension (kN)
$g(y)$	Geometry normalization factor
I	Transmitted intensity
I_0	Initial intensity
I_d	Intensity of dark images
I_{001}	Calculated amplitude of the d_{001}-peak
I_{calc}	Calculated intensity
L_w	Latent heat of evaporation (kJ/(kg))
m	Mass (kg)
q	Propagation constant (mm/($\sqrt{s}$))
S	Saturation (vol.%)
V	Volume (mm^3)
w	Water content
w_0	Initial water content (wt.%)
w_{max}	Maximal water content (wt.%)

Greek symbols:

Δz_W	Water thickness in beam direction (m)
Δz_S	Sand thickness in beam direction (m)
λ	Wave length of the neutron beam (μm)
Φ	Porosity (vol.%)
ρ	Density (kg/m^3)
Σ	Macroscopic cross section (b)
σ_t	Wet tensile strength (kN/m^2)
τ	Transmission
Θ	Diffraction angle (°)
Θ_W	Correlation factor between water content and transmission

Subscripts:

0	Time zero
Cor	Corrected
i	Phase
max	Maximum
Nor	Normalized
S	Sand
t	Time (s)
x, y, z	Coordinates

1 Introduction

1.1 Bentonite as binding agent in foundry industries

Clays, which consist of more than 50% smectite, are called bentonite (Odom 1984). Sodium-bentonites with a smectite composition of more than 70% montmorillonite are the most commonly used binder for quartz sand utilised as mould material in foundry industries (Campbell 2011). Compared to other clay minerals, the plate-shaped montmorillonite particles with an average diameter of 1 μm show a better binding capacity than larger clays, like illite or kaolinite (Patterson & Boenisch 1961*a*).

Typically, the bentonite content in so called "green moulding sands" varies between 5 to 10 wt.% (Fiore & Zanetti 2007). Depending on the bentonite content and quality, bentonite bonded moulding sands contain 2-5 wt.% water (Paluszkiewicz et al. 2008). Sometimes optional additives such as carbon are added to improve the surface of the casting product. Carbon forms a reducing atmosphere during casting at the mould-metal interface (Melcher & Schaefer 1978, Loto & Adebayo 1990, Parappagoudar et al. 2008).

Sand moulded casting is still one of the most efficient and cheapest methods to produce metal parts even of complex shapes. Besides simplicity and cost efficiency, bentonite bonded sands have an excellent environmental performance (Wang et al. 2007) compared to oil or resin bonded sands. Bentonite bonded sands have lower particulate and organic emission during casting and, moreover, they can be reused for mould production many times (Zabat & Van Damme 2000). Sands discarded after a maximum of cycles can be reused as raw material for concrete (Siddique et al. 2009, Guney et al. 2010) and ceramics production (Raupp-Pereira et al. 2006, Alonso-Santurde et al. 2012), or as hydraulic barrier for landfills (Zanetti & Godio 2006).

The mechanical properties of bentonite bonded sand moulds strongly depend on temperature, the amount of water, and the mineralogical composition of the bentonite (Grim & Guven 1978). During casting, a temperature gradient is induced within the sand mould. Water near the mould cavity evaporates and migrates into the colder mould interior where it condenses. As the heat advances further into the mould, evaporation continuous and the steam migrates further into the mould interior. The resulting total heat and moisture transport is composed of a number of different individual processes like heat conduction and convection, water vaporisation and condensation (Kubo & Pehlke 1986) as well as water uptake and release within the interlayer space of the smectites composing the bentonite.

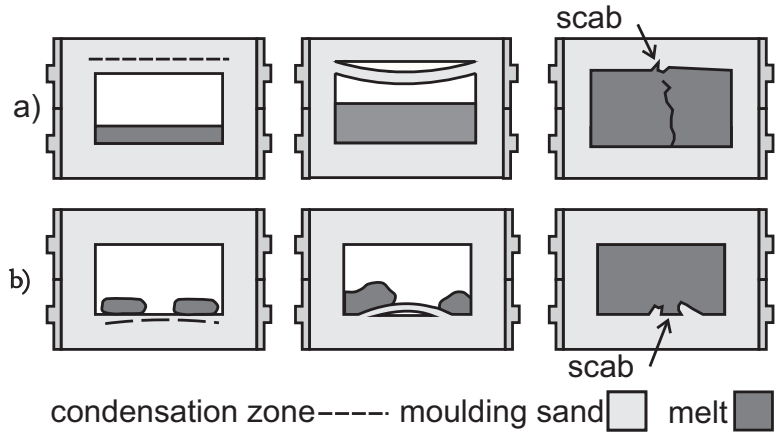

Fig. 1.1: Scrap development at the top (a) and bottom (b). After the metal melt enters the mould, sand layers next to the mould cavity flake off, causing casting defects like srabs or rat tails. (Modified after Hasse (2007))

The spatial and temporal gradients of heat and water concentration within the mould result in mobile zones of different mechanical properties of the moulding sand, notably of different tensile strength (Patterson & Boenisch 1964). In the condensation zone facing away from the melt, increasing moisture causes a significant decrease of tensile strength. In the hot sand layers facing towards the melt, i.e. the dry zone, quartz crystals expand and compressive stress arises. Together, the decrease of tensile strength and the increase of compressive stress cause spalling of sand layers - especially at the top of the mould cavity (Patterson & Boenisch 1964). The casting flaws of metal parts casted in a defective mould are called scabs (Fig. 1.1). Scabs are among the most frequently occurring casting defects associated with bentonite bonded sands (Campbell 2011). The quality of bentonite bonded sand in general and the tendency towards scabbing in particular can be determined by the ratio of compressive strength and wet tensile strength (Patterson & Boenisch 1964). Therefore, wet tensile strength is one of the key parameters to define the mechanical properties of bentonite bonded moulding sands.

1.2 Crystal structure of smectites

Montmorillonite, like all smectites, is a 2:1 phyllosilicate. Chemically, montmorillonite is a hydrous sodium calcium aluminium magnesium silicate hydroxide (Anthony et al. 2000) with a general formula of $(Na,Ca)_{0.33}(Al,Mg)_2(Si_4O_{10})(OH)_2 \cdot nH_2O$. Potassium, iron, and other cations are common substitutes. The exact cation ratio varies with the source. The crystal structure can be described by two tetrahedral sheets (*T-sheets*) of silica enclosing a central octahedral sheet (*O-sheet*) of aluminium oxy-hydroxide (Fig. 1.2). Each SiO_4^{4-} tetrahedron is connected to three other SiO_4^{4-} tetrahedrons by shared oxygen atoms. Consequently, each tetrahedron has three binding oxygen atoms and one non-binding oxygen. In an individual T-sheet, all non-binding oxygen atoms are pointing towards the same direction. Substitution of ions in the TOT-layer (mainly in

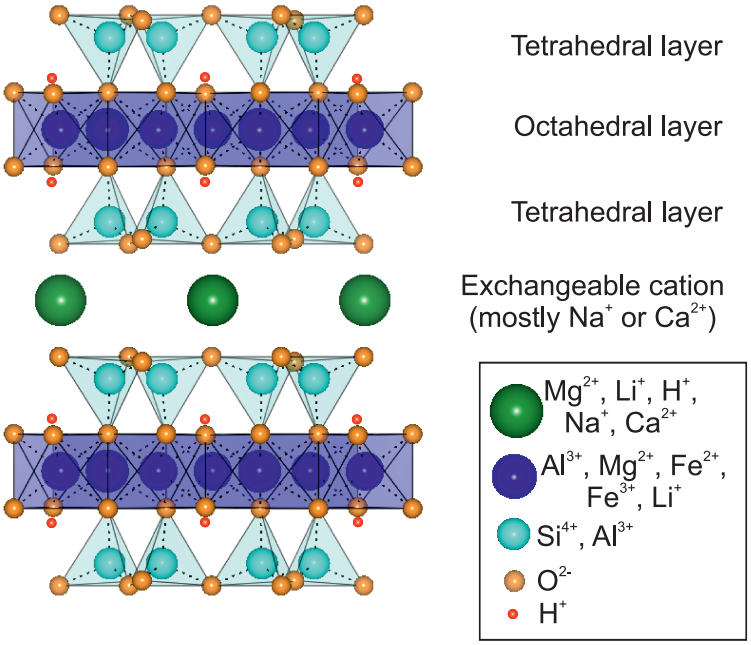

Fig. 1.2: Crystal structure of a dehydrated smectite. In the interlayer space, i.e. between two neighbouring TOT layers, exchangeable cations are positioned. In montmorillonite, the centre atoms of the octahedral sheets are typically Al^{3+} and Mg^{2+}, the exchangeable cation mostly is Ca^{2+} or Na^{+}. Created with VESTA (Momma & Izumi 2008, 2011) after entry 1100106 of the Crystallography Open Database (Gražulis et al. 2009, 2012)

the octahedral sheet) results in a charge of up to -0.6 per formula unit. This charge is balanced by monovalent cations such as K^+ or Na^+ or bivalent cations such as Ca^{2+}. These cations are located within the interlayer space and can be surrounded by water molecules. Hydration causes an expansion of the smectite structure in c-direction. Therefore, the smectite volume can swell. The water molecules taken up by the cations form layers (Hendricks & Jefferson 1938, Mering 1946). The number of water layers depends on the stage of hydration. However, the exact value of d_{001} lattice spacing also depends to the packing manner of the water molecules within the interlayer space (Barshad 1949). The arrangement and the swelling capacity and related properties of all smectites, therefore, strongly depend on the type of the exchangeable cation (Bergaya & Lagaly 2006).

1.3 Current state of research

1.3.1 Capillary force and tensile strength

Tensile strength bears an important role in stress and strain behaviour of unsaturated granular materials, being important for many fields from ceramic production (e.g. Israelachvili 2011) to oil and gas exploration (e.g. Falode et al. 2008, Barry et al.

2015). The basic physics behind wet granular materials such as moist quartz sand is qualitatively well understood (e.g. Haines 1925, Kohonen et al. 2004, Rabinovich et al. 2005, Zheng et al. 2010). In the past several decades, considerable advances have been made understanding the capillary attraction in unsaturated granular materials quantitatively.

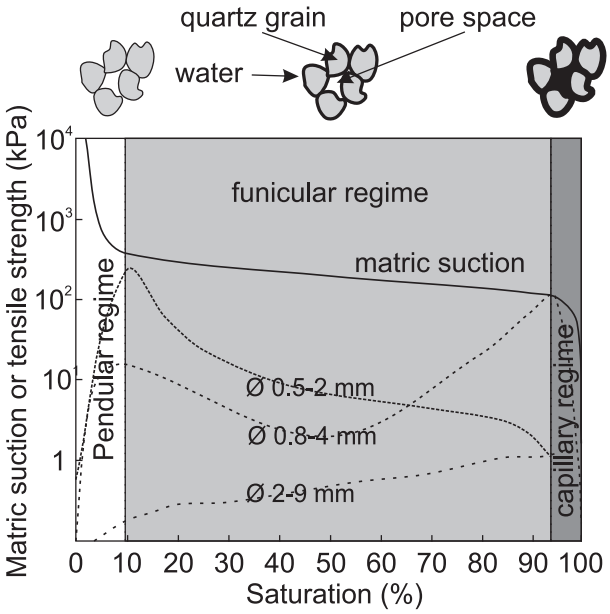

Fig. 1.3: Illustration of soil–water retention regimes (white: pendular regime, bright grey: funicular regime, dark grey: capillary regime) and tensile strength characteristics in unsaturated sands (dashed lines: silty sand ∅0.5 -2 mm, fine sand ∅0.8 -4 mm, and medium sand ∅2-9 mm). (Modified after Lu et al. (2007))

Capillary attraction between to grains is in general inversely proportional to particle size and degree of saturation (e.g. Orr et al. 1975, Dobbs & Yeomans 1992). Because capillary attraction depends on sand moisture and, therefore, on saturation, the tensile strength of moist granular media is normally given as a function of saturation or water content (e.g. Schubert 1968, Pierrat & Caram 1997, Heibrock et al. 2005, Lu et al. 2009, 2007, 2010). As the behaviour of wet granular materials differs strongly with the degree of saturation and, therefore, with the retention capacity of the porous medium, three different regimes are distinguished (Fig. 1.3): The pendular regime, the funicular regime, and the capillary regime (e.g. Schubert 1968, Orr et al. 1975).

To date, most of the current theories on capillary attraction are based on interaction between two particles within the pendular regime (e.g. Orr et al. 1975, Dobbs & Yeomans 1992, Lian et al. 1993, Molenkamp & Nazemi 2003). Theories about the tensile strength in the funicular and capillary regimes are rare (e.g. Lechman et al. 2006). Most of the models, which have been developed for the pendular regime, have in common that the system normally is simplified to a two-particle systems represented by smooth spheres, rough spheres, parallel plates, and other geometries (e.g. Fisher 1926, Mehrotra & Sastry 1980, Schubert 1968, Likos & Lu 2004). Therefore, an explicit knowledge of particle shape, surface roughness, size, separation distance, surface tension, and solid-liquid contact angle is required. A new approach is to derive the tensile strength of moist granular media by considering the suction stress of the granular material (Lu et al. 2010).

Despite these advances made so far, the relationship between the mechanical properties and sand moisture is still insufficiently understood and predictions of the tensile strength are imprecise. In general, however, it can be noted when the amount of water exceeds the pendular regime, capillary bridges merge and tensile strength decreases.

For clayey sands like moulding sands, the exact prediction of the tensile strength is even more challenging because the tensile strength in clayey sands is related to different forces and bonds (e.g. Wiebe et al. 1998, Lu et al. 2007, Tang et al. 2015). In general, four different forces and bonds can be distinguished: (1) van der Waals forces, (2) electrical double layer forces between clay mineral surfaces, (3) capillary forces at water bridges, and (4) bonds between grains caused by mineral precipitates from evaporating water.

The presence of clays makes precise predictions of the tensile strength very demanding. Due to the swelling behaviour of smectites, precise predictions of the amount of water within the pore space is difficult and no models exist to calculate the tensile strength in smectite rich sands or soils. Furthermore, the changes in temperature cause changes of the tensile strength during casting. Bentonite bonded moulding sands during casting, therefore, are among the most challenging wet granular media for the prediction of tensile strength. This is the reason why up to date only experimental work on the tensile strength of bentonite bonded moulding exists Patterson & Boenisch (e.g. 1961*a*,*b*, 1964, 1966). To obtain experimental access to the lowest tensile strength during casting, Wilhelm & Dietmar (1964) invented a new tensile testing method, in which the sample is heated from above before testing the tensile strength (i.e., wet tensile testing).

From such experiments (Patterson & Boenisch 1961*a*), it is well known that the strength of the moulding sand containing the same amount of water is considerably reduced with increasing temperature from room temperature up to the boiling point of water. Reaching temperatures above 90°C, capillary forces are considered to be of no effect on the strength of the moulding sand any longer Khanna & Swarup (1961) and the residual tensile strength is only related to the hydration state of the adsorbed cations. Therefore, the exact behaviour of a capillary bridges during evaporation is still vague (Maeda et al. 2003). With an increasing hydration of the cations, the tensile strength further decreases Khanna & Swarup (1961).

Due to condensation of water that evaporates in the mould region next to the metal melt, sand moisture exceeds the ideal amount and the tensile strength decreases. Therefore, the preferred location of rupture is somewhere in the condensation zone where the water amount is high and the temperature is near to the boiling point of water Patterson & Boenisch (1961*a*). If the moulding sand contains a large amount of Na-smectite, the excess water is absorbed on the clay surface in an organised structure. If Ca-smectite is the predominant clay, the water remains in liquid form (Odom 1984). Consequently, Na-bentonite bonded sands have a much higher wet tensile strength than Ca-bentonite bonded sands Patterson & Boenisch (1961*a*).

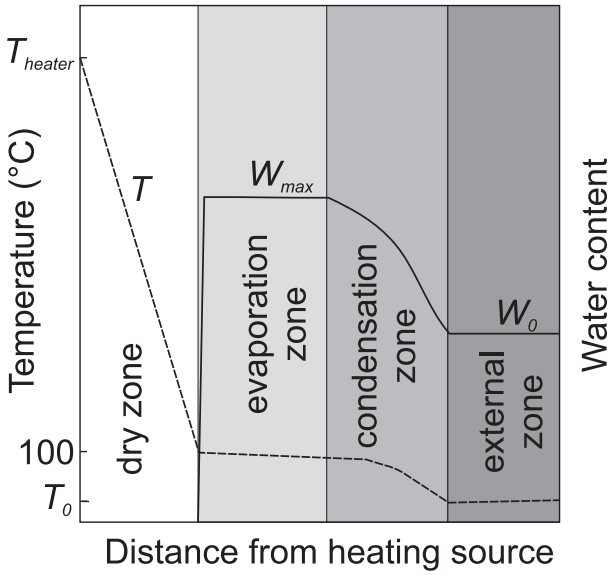

Fig. 1.4: Schematic distributions of temperature (dashed line) and moisture content (straight line) in a sand mould containing water (modified after Kubo & Pehlke (1986)). The different zones are illustrated by different grey scales.

1.3.2 Temperature and moisture kinematics during casting

Because tensile strength is strongly related to the sand moisture and temperature, the moisture and temperature profile within the sand during casting is of major importance. A model for the heat-driven mass transport in bentonite bonded moulding sands was stated by Patterson & Boenisch (1964) and improved by Kubo & Pehlke (1986). Further general models for heat-driven mass transport in porous media comparable to bentonite bonded moulding sand were described e.g. by Schröder & Macherauch (1977), Udell (1983), Starobin et al. (2011). Among these models, the model of Kubo & Pehlke (1986) is the most detailed one for coupled heat and mass transfer occurring during casting. Heat conduction, heat convection, condensation and evaporation were taken into account. At a given distance from the melt, equality of temperatures of water, quartz, and bentonite was assumed. Furthermore, heat transport by vapour transfer and by heat conduction between sand particles and vapour were taken into account. With respect to temperature, Kubo & Pehlke (1986) and Udell (1983) distinguished four zones with different transport characteristics (Fig. 1.4). These four zones can be described in the non-steady state system of this work in the following way:

1. The dry zone where the water has been vaporized completely. Here, the moisture content is zero and the temperature is above 100°C.

2. The evaporation zone where the temperature is 100°C and moisture is decreasing at a certain position over time.

3. The condensation zone where the temperatures are between 100°C and room temperature and the moisture content is increasing at a certain position over time.

4. The external zone where temperature and moisture are unaffected by the casting process.

In the dry zone, heat is mainly transported by conduction in the solid phases. In the evaporation and condensation zone, heat transport additionally takes place by water vapour flow within the open pore space. This moisture transport is driven by pressure difference, diffusion, vaporisation, and condensation.

1.3.3 Smectite alteration and the influence on the properties of bentonite bonded sands

Caused by the high temperatures during casting and the generated steam, the smectites within the moulding sand alter. These structural alterations, which are partly reversible and partly irreversible, lead to changes of the properties of the smectites.

At temperatures below 100°C, montmorillonite loses interlayer water in a step-wise manner (Schnetzer et al. 2016). While this process is assumed to be reversible, the influences of steam and temperatures above 100°C on the behaviour of smectites remain ambiguously. In contrast to the findings of Couture (1985) and Oscarson & Dixon (1989), Heuser et al. (2014) measured significant changes in cation exchange capacity only in the case of monovalent interlayer cations and, additionally, detected no effects on the internal structure of the mineral. Furthermore, no significant changes of hydraulic and mechanical properties have been reported for bentonite materials exposed to temperatures of 120°C under wet conditions (Wersin et al. 2007). At temperatures higher than 220°C, reports are unequivocally: At T = 220-350°C, OH-groups bonded at montmorillonite surfaces are removed (Drits et al. 1995). However, there are publications, which postulate that dehydroxylated smectites regain many of the lost hydroxyl groups if treated with steam at temperatures between 200-300°C (e.g., Grim and Bradley, 1948; Jonas, 1954; Heller et al., 1962; Hamilton, 1971; Alvero et al., 1994). Finally, at 500-800°C, intra-layer hydroxyl groups are removed (Emmerich et al. 1999) and the montmorillonite structure disintegrates irreversibly.

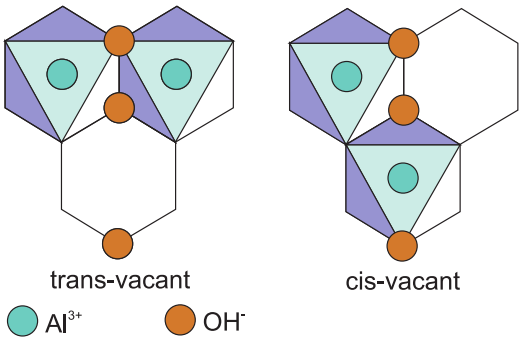

Fig. 1.5: Distribution of Al^{3+}-ions in octahedral sheets with cis- or trans-vacant sites (modified after Emmerich & Kahr (2001)).

The dehydroxylation temperature is related to the position of the Al^{3+} cations and their movement to other sites in the octahedral sheet (Drits et al. 1995). During dehydroxylation, Al^{3+} ions can move from trans-octahedral sites into cis-octahedral sites

(Fig. 1.5). For the movement additional thermal energy is required, being the reason for higher dehydroxylation temperature of smectites with Al^{3+} in trans-octahedral sites. By observing two dehydroxylation peaks after rehydroxylation of preheated montmorillonites, Drits et al. (1995) assumed that the transformation from trans-octahedral sites into cis-octahedral sites occurs partially. Furthermore, Drits et al. (1995) noted that structural changes and Al^{3+} movement during dehydroxylation are not restricted by the interlayer cations.

While Al^{3+} can move between different sites, Fe^{3+} does not migrate (Heller-Kallai & Rozenson 1980). The movement of small Li^{+}, Cu^{2+}, or Zn^{2+} cations from the interlayer to the hexagonal cavities of the tetrahedral sheet and then to the vacant octahedral positions of dioctahedral clays upon heating is a well-known phenomenon (e.g. Hofmann & Klemen 1950, Greene-Kelly 1955, Calvet & Prost 1971, Emmerich et al. 1999).

1.4 Aim of this thesis

Although, bentonite is widely used as binder for quartz sand in foundry industries, its binding mechanisms are poorly understood. The motivation of the present study, therefore, was not only to contribute to the improvement of the most sustainable mould material, but also to acquire fundamental scientific knowledge about the effects of heat-driven moisture transport on the mechanical properties of bentonite bonded sands.

Even though scabs are by far the most common casting defect in green sand casting, neither the exact location of rupture nor the reasons for the strong decrease in tensile strength were determined precisely, until today. Therefore, the aim of the first part of this study was to locate the exact fracture position and to determine the exact temperature and moisture at this location of lowest strength. An exact localisation provides an understanding of the massive decrease in tensile strength and, therefore, a better understanding of the binding mechanisms of smectites.

The second part of this work focuses on the reusability of bentonite bonded sand as mould material. Exposed to temperatures above 100°C, montmorillonite loses interlayer water in a stepwise manner and dehydrates. Whereas this process is reversible, the loss of OH-groups (dehydroxylation) at higher temperatures (beginning at 300°C) likely is irreversible (see above) (Schultz 1969, Wolters & Emmerich 2007) and influences the smectites properties as binding agent permanently (Żymankowska-Kumon et al. 2012, Bobrowski & Grabowska 2012). While the structural changes of smectites with temperature are well understood, the changes in binding and transport properties caused by the alteration of bentonite bonded sand with temperature are still insufficiently examined. Therefore, aim of the second part of this thesis is to qualify the transport and mechanical properties of cyclically reused moulding sands (i.e., sands exposed to drying and remoistening cycles) and of sands, which were exposed to temperatures above the dehydroxylation temperature of smectite. Understanding the interplay between smectite alteration and sand properties is an important step forward in improving the recycling and reuse of moulding sands. Furthermore, better knowledge about the

influence of smectite alteration on the properties of bentonite bonded sand enhances the understanding of the binding mechanism within bentonite bonded sands, which also is of tremendous importance for related processes like transport properties in bentonite based disposal sites for radionuclides (Emmerich 2000).

In the third part of this study, the differences between Ca-montmorillonites and Na-montmorillonites were investigated. For this, the changes of mechanical properties and transport properties of cyclically reused and heat pre-treated Ca-bentonite bonded sands were investigated and compared with the results of the second part of this study. Elaborating the differences between Ca-bentonite and Na-bentonite bonded sands is explicitly apt to provide a better understanding of the specific changes induced by heat pre-treatment and cyclic reuse in Na-bentonite bonded sands, which are by far the preferentially used ones in foundry industry.

1.5 Author contributions

This thesis is the detailed report of the author's Ph.D. research work on bentonite bonded moulding sands. Three chapter of thesis are based on scientific research manuscripts, which were published as a journal article (chapter 3), accepted for publication (chapter 4), and in preparation for submission (chapter 5). The author of this thesis, Korbinian Leonhard Thomas Schiebel, is the principal author of all three of these manuscripts. The remaining chapters of the thesis comprise a general introduction, methodological aspects, and conclusions.

Chapter 3 was published with the title "Neutron Radiographic Study of the Effect of Heat-Driven Water Transport on the Tensile Strength of Bentonite-Bonded Moulding Sand" by Korbinian Schiebel, Guntram Jordan, Anders Kaestner, Burkhard Schillinger, Sandra Boehnke, and Wolfgang W. Schmahl in TRANSPORT OF POROUS MEDIA. Supervised by GJ, the principal author was designing the neutron-compatible tensile strength testing device, applying for beam time at FRMII and PSI, planning and conducting the experiments, analysing and interpreting the data, and writing the manuscript. The remaining authors contributed to the experiments as beam line scientists and/or helped to improve the manuscript.

Chapter 4 is accepted for publication in EUROPEAN JOURNAL OF MINERALOGY with the title "Effects of heat and cyclic reuse on the properties of bentonite-bonded sand" by Korbinian Schiebel, Guntram Jordan, Anders Kaestner, Burkhard Schillinger, Robert Georgii, Kai-Uwe Hess, Sandra Boehnke, and Wolfgang W Schmahl. Supervised by GJ, the principal author was designing the neutron-compatible tensile strength testing device, applying for beam time at FRMII and PSI, planning and conducting the neutron experiments, analysing and interpreting the data, and writing the manuscript. AK, BS, RG contributed to the experiments as beam line scientists and helped to improve the manuscript. KUH conducted the gravimetric and calorimetric experiments and, together with SB and WWS, helped to improve the manuscript.

Chapter 5 is in preparation for submission as journal article. Together with GJ, the principle author was supervising the master student Sophie Wunderlich, who contributed

to this chapter. The master student used the experimental setup, which was provided by the author and the thesis supervisor, and conducted the Ca-bentonite experiments, which were designed by the author and the thesis supervisor. Analysis of the data was performed with Matlab scripts written by the author. Interpretation of the data was performed by SW together with the author and thesis supervisor. The neutron experiments were made possible by the beam line scientists AK, BS, and RG.

2 Methods

2.1 Wet tensile testing

As mentioned before, a temperature gradient is induced into the mould by heat transport from the metal melt into the moulding sand. The heat is transported connectively and conductively. By the progressing heat, the water in the mould next to the mould cavity evaporates. The steam diffuses into colder mould regions where it condensates. The so-called condensation zone is formed. The condensation zone is characterized by a considerably an increased water content. The temperature in the condensation zone is close to the boiling point of water (approx. 100°C) mainly due to the heat of condensation provided by the incoming steam.

The increased water content of the condensation zone causes a reduction of the tensile strength. The significant decrease of the tensile strength has a considerable influence on the formation of casting defects (scabs, buckles, rat tails, veining). Wet tensile strength testing, therefore, is the most suitable method to characterise the mechanical strength of a sand mould during casting.

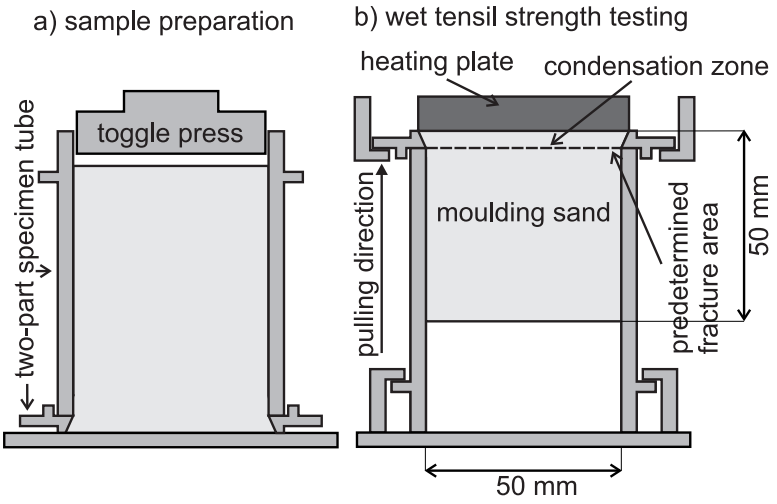

Fig. 2.1: Sketch of a wet tensile testing apparatus (modified after Hasse (2007)). a) The two-part tensile specimen tube is turned upside down, filled with moist moulding sand, and compressed with 2.5 kN. b) After heating the sample from above by a heating plate, tensile testing is conducted.

For wet tensile testing, a specimen (standardized in dimension and compaction, Fig. 2.1) is heated from above (heater temperature = 310°C) to induce temperature

and moisture gradients within the sample (BDG 1997). Once the condensation zone approximately reaches an intended rupture position within the sand specimen, the tensile force (F_r) is measured. Subtraction of the weight of the upper sample part (F_g) from the tensile force, then, provides the net tensile force (F_t). The ratio of the measured net tensile force and the sectional area of the specimen (A) yields the wet tensile strength (σ_t):

$$\sigma_t = \frac{F_t}{A} \tag{2.1}$$

2.2 Neutron radiography

2.2.1 Basics and experimental set up

In the past, high precision in-situ measurements of heat-driven moisture transfer within porous media were extremely challenging. Due to recent advances, neutron radiography became a powerful method to determine the water kinematics within porous media quantitatively (Schillinger et al. 2006, Kaestner et al. 2008).

Neutron radiography is a non-destructive imaging method that works analogously to X-ray radiography. Unlike X-ray, however, neutrons interact exclusively with the atomic nuclei. Possible reactions of neutrons with atomic nuclei are neutron absorption or coherent and incoherent scattering. The attenuation of a neutron by matter, therefore, is different to X-ray attenuation. While the attenuation of X-ray continuously increases with the electron density (Hubbell & Seltzer 1995), there is no significant correlation between attenuation of neutrons and the atomic number (Lindner et al. 1976). A neutron radiography system consists of a nearly parallel neutron beam and a detector system. The neutron source can be a reactor like the Neutronenquelle Heinz Maier-Leibnitz (FRM II) or a spallation source like the Swiss Spallation Neutron Source (SINQ) (Fischer 1997).

The sample to be investigated is placed in the beam, the neutrons transmitted through the sample are measured by a detector. Because different materials have different attenuation coefficients, information about sample composition and structure can be obtained by the transmitted beam by the Beer-Lambert law (Lambert 1760, Beer 1852):

$$\tau = \frac{I}{I_0} = e^{-\Sigma_i \Delta z_i} \tag{2.2}$$

where τ is the local transmission of a parallel neutron beam in beam direction. I and I_0 are the transmitted and the initial intensity. Σ_i is the macroscopic cross section of phase i and Δz_i is the thickness of phase i in beam direction (note: the Einstein summation convention is used (Einstein 1916), therefore Σ is not used as summation operator).

The macroscopic cross (Fig. 2.2) section and, thus, the attenuation of neutrons by most elements forming silicate minerals (Si, Al, Ca, Fe, Mg, Na, O ...) is at least one order of magnitude smaller than attenuation by hydrogen. Neutron radiography, therefore,

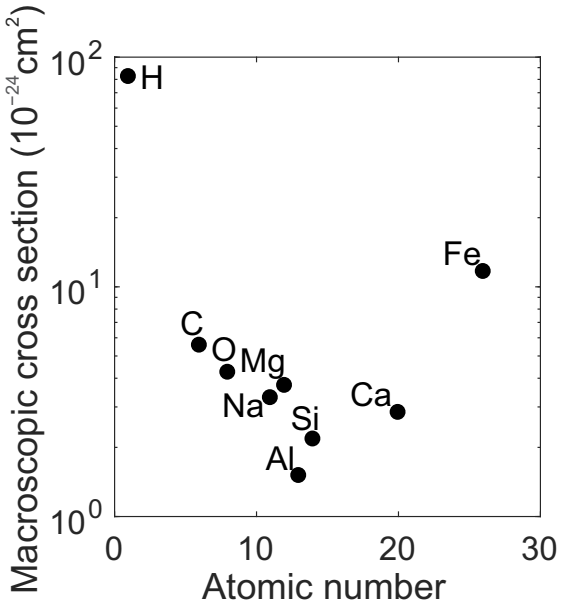

Fig. 2.2: Macroscopic cross sections of smectite forming elements in their natural isotopic composition after Sears (1992).

can quantify water transfer within porous media such as quartz sands, concretes, plants, rocks and soils in-situ (Hassanein et al. 2006, Shokri et al. 2008, Schillinger et al. 2011, Sedighi-Gilani et al. 2013, Shokri & Or 2013, Hall 2013, Jordan et al. 2013, Villman et al. 2014, Boon et al. 2015) and is the most suitable method to determine the water transport during wet tensile with a high spatial and temporal resolution. Therefore, it is the ideal tool to measure the water kinematics in bentonite bonded moulding sands in-situ during the complete wet tensile testing procedure.

For the neutron radiography experiments, a wet tensile testing apparatus was constructed, which is compatible with simultaneous exposure to neutron radiation. The specimen tube (Fig 2.4) was constructed with a square cross section to avoid complicated geometric aftermaths of a round sample. Heating and tensile testing was imaged by taking neutron radiography time series. Evaluating the radiographs, the water content in beam direction could be calculated for each pixel.

2.2.2 Image analysis

As mentioned above, the local transmission $\tau(x, y)$ of a parallel neutron beam through a specimen in beam direction z is given by Beer-Lambert law:

$$\tau(x, y, t) = \frac{I(x, y, t)}{I_0(x, y)} = e^{-\Sigma_i \Delta z_i(x,y,t)} \tag{2.3}$$

where $I(x, y, t)$ and $I_0(x, y)$ are the transmitted and the initial intensity, respectively, at the pixel-position x, y and time t. Σ_i is the macroscopic cross section of phase i and $\Delta z_i(x, y, t)$ is the thickness of phase i in beam direction z. The initial intensity at each pixel $I_0(x, y)$ is determined by the median intensity of ten open beam images. To eliminate the influence of camera offset and dark current, all images were black

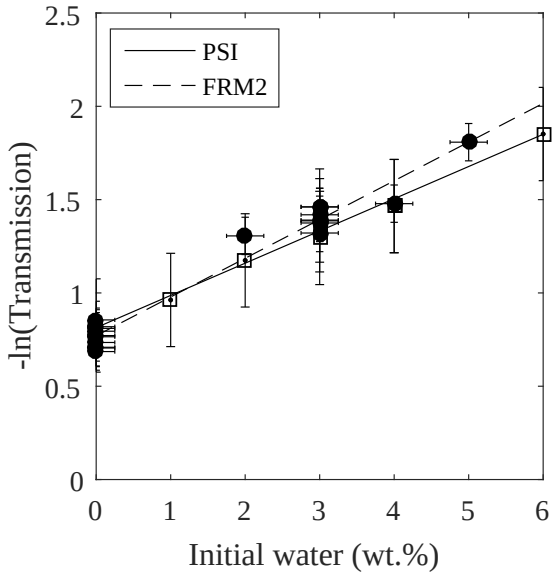

Fig. 2.3: Calibration of correlation between neutron transmission and water thickness: Negative natural logarithm of the corrected and normalized neutron transmissions $-ln(\tau^{cor,nor})$ is plotted versus the known sand moisture for a sample thickness of 50 mm (44 mm sand, 2x3 mm aluminium). Linear regressions of the transmissions measured at the two neutron beam lines are inserted (PSI solid line, empty symbols; FRM II dashed line, filled symbols). The correlation factor Θ_W can be determined by the slope of the linear regressions. The negative natural logarithm of the transmission through the dry sand $-ln(\tau_S^{cor,nor})$ is equivalent to the interception of the ordinate.

field corrected. At each pixel (x, y), therefore, the median intensity of ten dark images $I_d(x, y)$ was subtracted from each experimental radiograph as well as from the open beam images:

$$\tau(x, y, t)^{Cor} = \frac{I(x, y, t) - I_d(x, y)}{I_0(x, y) - I_d(x, y)} \tag{2.4}$$

Intensity fluctuations of the neutron beam while taking the radiography image sequence were corrected by an individual image correction factor $b(t)$ according to Hassanein (2006). The factor equals the ratio of the average brightness of an open beam area $I(x_o, y_o, t)$ within a radiograph and the average brightness of the same area in the open beam images $I_0(x_o, y_o)$. Additionally, the factor has to include a black field correction for the selected area $I_d(x_o, y_o)$ which needs to be subtracted from both values:

$$b(t) = \frac{I(x_o, y_o, t) - I_d(x_o, y_o)}{I_0(x_o, y_o) - I_d(x_o, y_o)} \tag{2.5}$$

The transmission then is:

$$\tau^{Cor}(x, y, t) = \frac{I(x, y, t) - I_d(x, y)}{I_0(x, y) - I_d(x, y)} / b(t) \tag{2.6}$$

Using the above corrections, the measured neutron transmission can be correlated with the water thickness $\Delta z_W(x, y, t)$ in a porous medium like quartz sand:

$$ln\left(\tau^{Cor}(x, y, t)\right) = -\Delta z_S \Sigma_S - \Delta z_W(x, y, t)\Sigma_W \tag{2.7}$$

where the index S stands for the dehydrated moulding sand and the tube walls.

For an exact value of Σ_S a precise chemical analysis of the moulding sand is required. For a constant sand thickness Δz_S, this can be avoided by measuring the neutron transmission of the dry sand τ_S. Accordingly, $\Delta z_S \Sigma_S$ can be replaced by $-ln(\tau_S)$:

$$ln\left(\tau^{Cor}(x,y,t)\right) = ln(\tau_S^{Cor}) - \Delta z_W(x,y,t)\Sigma_W \tag{2.8}$$

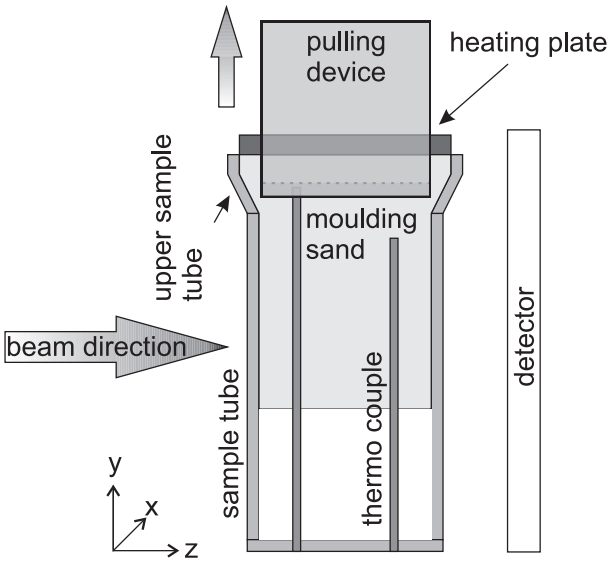

Fig. 2.4: Sketch of the two-part specimen tube and the heating plate used for the wet tensile testing.

In this work, the specimen thickness in beam direction is not constant but well defined (Fig. 2.4). The sand and water transmission of the pyramidal part of the sample tube, therefore, can be normalized to the prismatic part of the sample tube by inserting a normalization factor $g(y)$:

$$g(y) = \begin{cases} 1.227 \text{ for } y \leq 0.5 \\ 1.341 - 0.227y \text{ for } 0.5 < y < 1.5 \\ 1 \text{ for } y \geq 1.5 \end{cases} \tag{2.9}$$

The relation for the corrected and normalized transmission then is:

$$ln\left(\tau^{Cor,Nor}(x,y,t)\right) = \frac{ln\left(\tau^{Cor}(x,y,t)\right)}{g(y)} = ln\left(\tau_S^{Cor,Nor}\right) - \frac{\Delta z_W(x,y,t)\Sigma_W}{g(y)} \tag{2.10}$$

With increasing water thickness, the relevance of multi scattering effects on the measured intensities increases. For a constant thickness of the porous medium, multi scattering can be taken into account by reference calibration measurements (Kang et al. 2013). Exchanging the product of the water thickness ($\Delta z_W(x,y,t)$) and the macroscopic cross section of water (Σ_W) by the water content ($w(x,y,t)$) and a correlation factor (Θ_W), the corrected and normalized transmission data ($-ln(\tau^{Cor,Nor}(x,y))$) of the reference measurements can be plotted versus the moisture content of the reference sample (Fig. 2.3).

$$ln\left(\tau_{Ref}^{Cor,Nor}(x,y)\right) = ln\left(\tau_{S}^{Cor,Nor}\right) - \Theta_W w(x,y,t) \tag{2.11}$$

The slope and the intercept of the ordinate of the linear regression of reference transmission data yield the correlation factor (Θ_W) and the transmission of the dry sand ($ln(\tau_S^{Cor,Nor})$) respectively. Therefore, the total moisture amount can be calculated by:

$$w(x,y,t) = \left(ln\left(\tau_{S}^{Cor,Nor}\right) - ln\left(\tau^{Cor,Nor}(x,y,t)\right)\right)/\Theta_W \tag{2.12}$$

For the calculation of the error of both the initial water content and the measured transmission, the equations from York et al. (2004) where applied using the matlab script from Thirumalai et al. (2011). In accordance with the law of error propagation, the maximum uncertainty in calculating the absolute water content can be assumed to be $\pm 0.65 wt.\%$

$$\delta_w = \sqrt{\delta\Theta_W^2 + \delta\left(ln(\tau_S^{Cor,Nor})\,{\Theta_W}^{-1}\right)^2} = 0.65\,wt.\% \tag{2.13}$$

The high thermal conductivity of aluminium causes condensation of water at the tube walls. This condensation leads to water gradients in beam direction z. However, the water distribution in beam direction cannot be imaged in radiographs. Only the total transmission in z-direction can be measured. In order to assess the water inhomogeneity in beam direction, profiles were measured along the y-axes. In these y-profiles, the deviations between the average intensity and the intensity measured in the centre of the profile were never bigger than 1%. Assuming the y-profiles being representative for the beam direction z, water condensation at the tube walls contributes to the total uncertainty of the calculation of the water amounts by approximately less than 1%.

In combination with temperature measurements and mechanical testing, neutron radiography is not only a suitable method to investigate the coupling of heat and moisture transport but also to assess the relation between transport and material property (Schiebel et al. 2017). Furthermore, if water is the only mobile phase, plots of local moisture content vs. temperature can be taken as local thermo-gravimetric measurements within a large scale sample (Jordan et al. 2013).

2.3 Neutron diffraction

Neutron diffraction is the application of neutron scattering to determine the crystal structure of solid matter. For this, a sample is placed in a neutron beam and the measured diffraction pattern provides the structural information of the sample. The technique is analogously to X-ray diffraction but due to the different scattering properties, neutrons and X-rays provide complementary information. Neutron diffraction is the perfect tool to determine the amount of water within the interlayers of the smectites. Because of the small smectite content in the moulding sand (8 wt.% or less), the smectite interlayer spacing cannot be measured by X-ray diffraction. The hydration state of the interlayer

can directly be assessed by the d_{001}-values of the smectite minerals. The $_{001}$-values can be calculated from the peak position of the diffraction pattern by Bragg's law (Bragg & Bragg 1913):

$$d_{001} = \frac{\lambda}{2sin(\Theta_{001})} \tag{2.14}$$

where d_{001} is the d-spacing, λ is the wave length of the neutron beam and Θ_{001} is the diffraction angle of the 001-reflection.

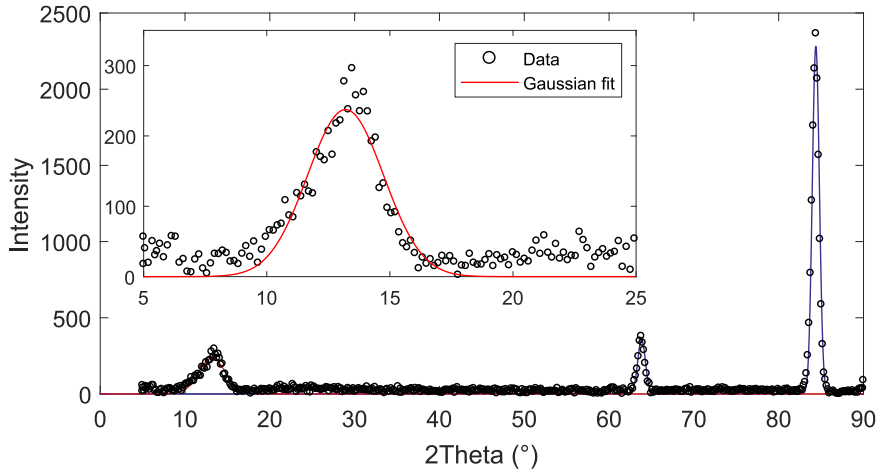

Fig. 2.5: Neutron diffraction pattern of the reference sand at room temperature. The background-corrected fit according to Eqn. 2.15 is included.

After subtracting the background, the diffraction angle (Θ_{001}) can be determined by fitting the 001-peak in the powder pattern with a Gaussian function (Fig. 2.5).

$$I_{calc}(2\Theta) = I_{001}e^{\frac{-2(\Theta-\Theta_{001})}{c^2}} + B_1 2\Theta^{B_2} \tag{2.15}$$

$I_{calc}(2\Theta)$ is the calculated intensity as function of the diffraction angle Θ. I_{001} is the calculated amplitude (peak intensity) of the 001-peak, Θ_{001} is the calculated centre peak position of the 001-peak, c is the full half maximum of the 001-peak. The background of each diffraction pattern was fitted by a Matlab algorithm with an exponential function, therefore, $B1$ and $B2$ are the background fitting parameters.

Following the diffraction angle is:

$$\Theta_{001} = \left(2\Theta + c^2 ln\left(\frac{I_{calc}(2\Theta) - B_1 2\Theta^{B_2}}{I_{001}}\right)\right)/2 \tag{2.16}$$

The d_{001}-spacing varies between approx. 10 and 20 Å depending on the amount of interlayer water (Holmboe & Bourg 2013, Villar et al. 2012, Ferrage et al. 2010, Zheng

et al. 2010, Collins et al. 1992, Bird 1984)). Particular details, like the used wave length, of the performed diffraction analyses are given in the specific methodological sections of the following chapters.

2.4 SEM

Scanning electron microscopy (SEM) is a non-destructive imaging technique, which images the surface of a sample by scanning it with a focused electron beam. Various signals are generated such as secondary electrons (SE), reflected or back-scattered electrons (BSE) or characteristic X-rays. The spatial resolution of SEM images is high enough to resolve the microstructure within the moulding sand. This microstructure depicts the specific arrangement of clay particles and quartz grains within the compacted moulding sand. The energy-dispersive X-ray spectroscopy (EDX) thereby helps to distinguish between clay and quartz grains. Particular details of the performed electron microscopy analyses are given in the specific methodological sections of the following chapters.

2.5 TG & DSC

Thermogravimetry (TG) or thermal gravimetric analysis (TGA) is a method, which determines the mass of a sample over time as the temperature changes. The sensitivity of modern devices is high enough to measure not only the dehydration process within the sand during heating, it also makes it possible to determine the dehydroxylation temperatures of the smectites within the moulding during heating. The data, thus, enable inferring on structural changes of the smectites. Also differential scanning calorimetry (DSC) is a thermoanalytical technique. It measures the difference in heat, which is required to increase the temperature of a sample and a reference. The heat difference allows the determination of the dehydration and dehydroxylation temperature precisely. Particular details of the conducted thermal analyses are explained in detail in the specific methodological sections of the following chapters.

3 Neutron radiographic study of the effect of heat-driven water transport on the tensile strength of bentonite bonded moulding sand

3.1 Open questions

In spite of the common use of wet tensile testing in industries (Campbell 2011), water and heat kinematics within the specimen were never quantitatively measured in-situ during wet tensile testing. Thus, the dependencies of fracture plane position and tensile strength on moisture and temperature were never determined precisely. Aim of the first part of this study was, therefore, to follow the location of the weakest point within the moulding sand quantitatively during time and to determine the effects of heat and water kinematics on fracture location and tensile strength.

3.2 Materials and methods

Neutron radiography time series were performed both at the cold neutron imaging facility ICON (SINQ, Paul Scherrer Institute, Villigen, Switzerland, (Kaestner et al. 2011)) and at the imaging beamline ANTARES (FRM II, Heinz-Maier-Leibnitz-Zentrum, Garching, Germany, (Schulz & Schillinger 2015)). At ICON wet tensile strength testing (from the begin of heating to the moment of rupture) was followed using a CMOS camera (image frequency: 4 frames per second, field of view: 105 mm x 72 mm, spatial resolution 0.047 mm/pixel, sample detector distance 4 cm). At ANTARES, heating and tensile testing was imaged with a CMOS camera (image frequency: 0.55 frames per second, field of view: 100 mm x 80 mm, spatial resolution 0.047 mm/pixel, sample detector distance 12 cm).

From the evaluation of the radioraphs the water kinematics was quantified. According to Hassanein et al. (2006) the radiographs were corrected for white and dark spots, background noise, and beam fluctuation. The local water content was calculated from the corrected radiographs by:

$$w(x,y,t) = \left(ln\left(\frac{\tau_s^{cor}}{g(y)}\right) - ln\left(\frac{\tau(x,y,t)^{cor}}{g(y)}\right)\right) / \Theta_W \tag{3.1}$$

Green sand consisting of quartz (average grain size approx. 0.3 mm) and 8 wt.% of natural sodium bentonite (Wyoming) was obtained from S&B Minerals (Imerys, Marl, Germany). The sand has been dried at 120°C for at least 24 hours before it was remoistened with defined water quantities (2, 3, 4, and 5 wt.% H_2O) and aged for at least 24 hours in air-tight bags. The aged sand, then, was sieved into a two-part aluminium specimen tube Fig. (2.4). The lower prismatic part of the specimen tube has a quadratic 44 mm x 44 mm cross section and a height of 100 mm. The quadratic cross section of the upper pyramidal part (height 20 mm) increased from 44 mm x 44 mm to 54 mm x 54 mm. The aluminium walls of the tube (thickness 3 mm) were almost transparent in the neutron radiographs. The two-part specimen tube was turned upside down and filled with sieved sand. Subsequently, the sand within the tube was compressed with 1 MPa. Compaction depth Δy_C was measured to determine the sample volume and to calculate porosity Φ and saturation S. For this, porosity and saturation are defined by:

$$\Phi = \frac{V_{St} - \Delta y_C A - m_S/\rho_S}{V_{St} - \Delta y_C A} \tag{3.2}$$

(V_{St} is the volume of the complete sample tube, $m_S$is the mass of the dry sand, ρ_S is the density of the dry sand, A is the cross section area of the lower sample tube), and

$$S = \frac{m_W/\rho_W}{V_{St} - \Delta y_C A - m_S/\rho_S} \tag{3.3}$$

(ρ_W is the density of water, m_W is the mass of water) respectively.

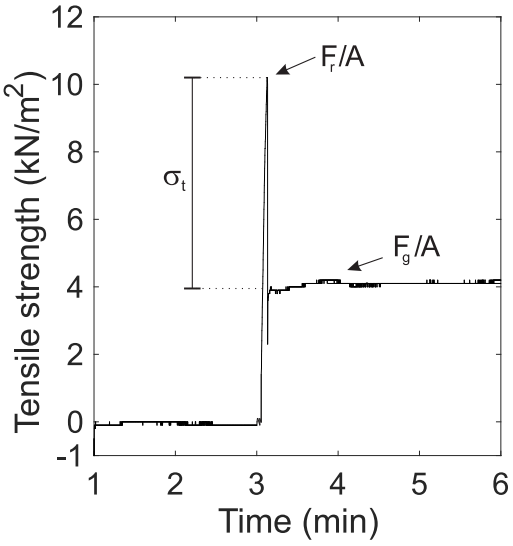

Fig. 3.1: Tensile strength testing signal.

To induce moisture and temperature gradients within the sample, the sand was contacted from above with a heater which had been preheated to 310°C according to VDG norm P38 (BDG 1997). After a defined heating period, tensile force was increased by 50 N/s and continuously measured by a stress gauge with a frequency of 200 data points per second. After rupture, the tensile strength σ_t was determined by subtracting the weight of the upper sample part F_g (specimen and specimen tube) from the maximum measured tensile force F_r and normalizing this net tensile force to the cross sectional area A at the specimen neck (Fig. 3.1).

$$\sigma_t = \frac{F_r - F_g}{A} \tag{3.4}$$

Thermocouples provided temperature data integrated over a sample volume of several cubic millimetres. Temperature gradients on the scale of individual sand grains and pores (filled or unfilled) were not accessible. The comparison of temperature measurements at a given position in different experiments performed under same conditions (moisture, porosity) showed that a temperature can be assigned to a certain position with an accuracy of approximately ±2.5 mm. This limited spatial resolution mainly results from the low accuracy of the determination of the thermocouple position in the radiographs.

The evolution of the local temperature was continuously measured during the experiments at four different positions below the specimen neck with a frequency of two measurements per second. In order to determine the temperature distribution in the upper pyramidal part, additional reference experiments without tensile testing were conducted. The local temperature, thereby, was measured in steps of 5 mm from the heating plate with a frequency of two measurements per second for at least 330 seconds.

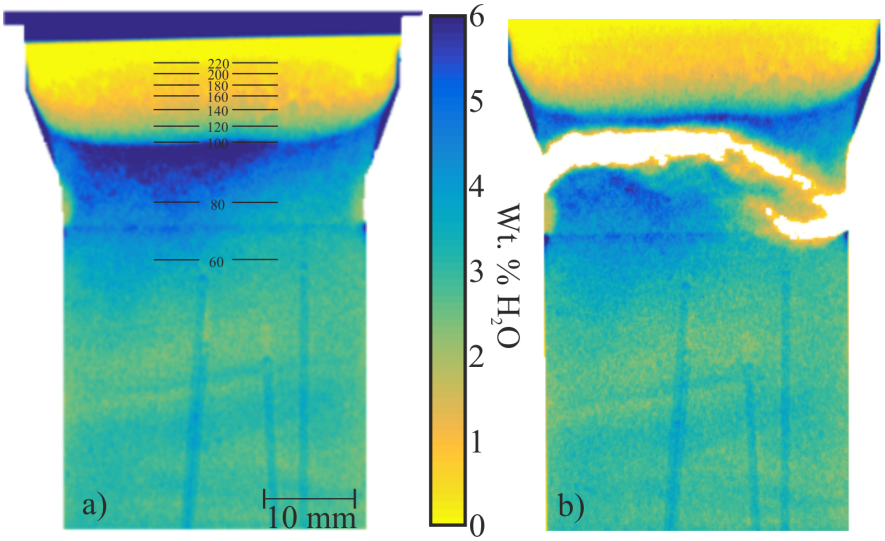

Fig. 3.2: Moisture distribution (colour coded) calculated by equation 2.12 from the radiographs taken 0.5 seconds before (a) and 0.5 seconds after (b) rupture. The temperature profile before rupture is given by isotherms (black lines in radiography a).

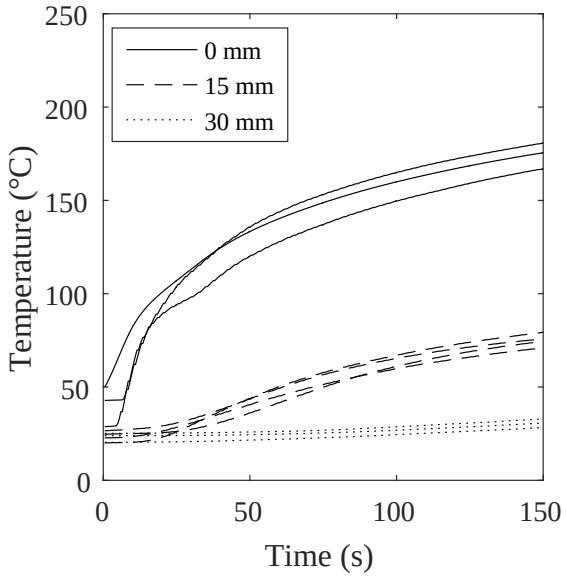

Fig. 3.3: Temperature evolution with time in three different experiments with an initial water content of 3 wt.% measured with thermocouples at three positions below the heating plate (0, 15, 30 mm).

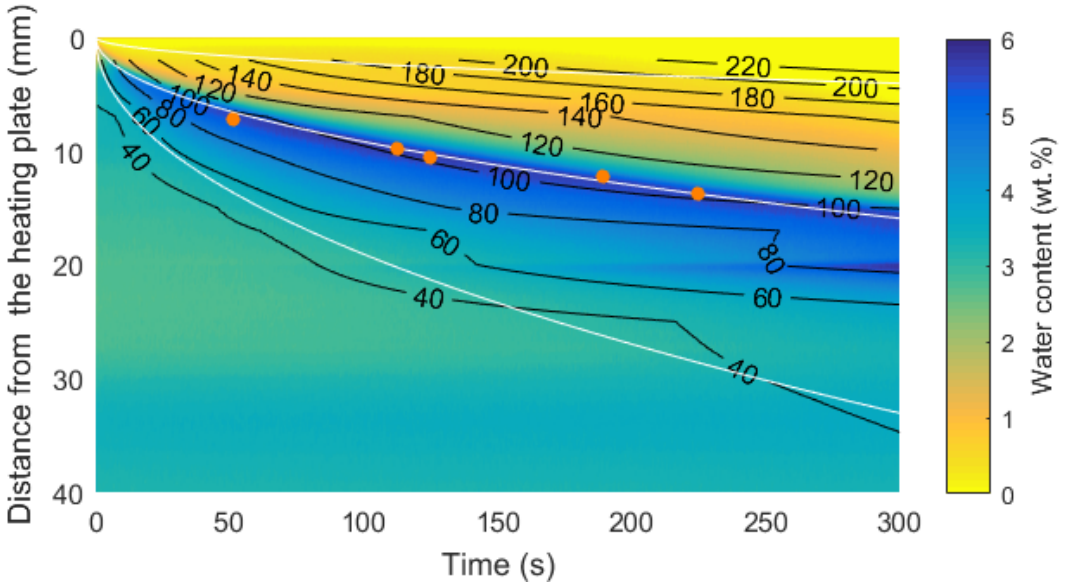

Fig. 3.4: Evolution of the moisture (colour coded) and temperature (black isotherms) during heating. The rupture positions from tensile tests after different heating times are marked by orange dots. Note, the different rupture positions were determined in a series of experiments with identical parameters and, therefore, identical heat and water kinematics. The white lines mark the boundaries between (from top to bottom) the dry zone, evaporation zone, condensation zone, and the external zone, respectively.

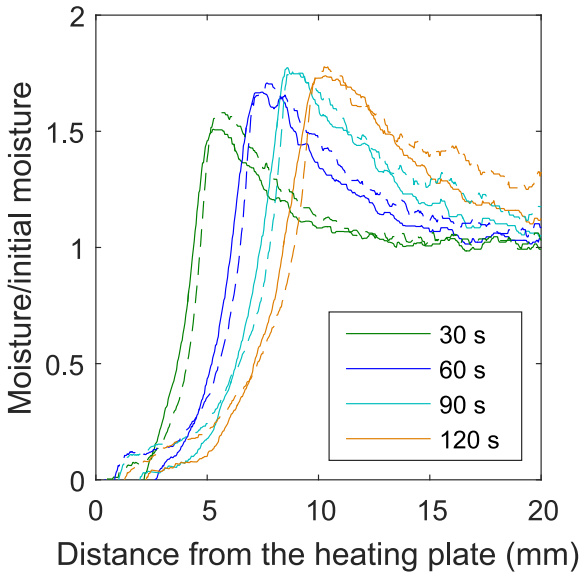

Fig. 3.5: Moisture distribution 30 (green), 60 (blue), 90 (turquoise), and 120 seconds (orange) after start of heating plotted versus the distance from the heating plate for sands with different initial moistures (solid line: 3 wt.% water, dashed line: 5 wt.% water).

3.3 Results

From individual neutron radiographs taken at a given time (Fig. 3.2), the water contents were calculated along the central vertical profile by equation 2.12. The corresponding temperatures (Fig. 3.3) were allocated (Fig. 3.2 a). All data were plotted versus time (Fig. 3.4). In experiments with identical parameters (initial sand moisture, sand compaction, heater temperature, heater power), water kinematics is highly reproducible. Within the spatial accuracy of water detection by neutron radiography, therefore, the moisture vs. time plots of different experiments with identical parameters are coincident.

Water evaporation starts instantaneously upon contact of sand specimen and heating plate. Steam diffuses into the sand interior where it condenses. An increase in the local water content in the condensation zone is the consequence (Fig. 3.5). After approximately 120 seconds, condensing steam reaches the interstice of the specimen tube (joining of lower base part and upper pyramidal part of the tube; Fig. 2.4). At the interstice, condensation is increased and, eventually, water is lost from the specimen by steam venting through the slit. Ignoring the interstice effect, the position of maximum local moisture correlates well with the 100°C isotherm.

In the radiographs, water content can be measured at any given time and point of the sample - for instance at the position of a thermocouple. This water content can be plotted vs. the momentary temperature reading of the thermocouple (Fig. 3.6). The experiments show that the water content first increases with increasing temperature and at $T \geq 100$°C rapidly decreases. Dehydration continues to temperatures of approximately 140°C. Between 140°C and 310°C no further increase of the neutron transmission (i.e. release of water or hydroxyls) can be observed.

If tensile stress is applied to the sample, neutron radiography allows an exact determination of the rupture location. Vertical profiles of the neutron transmissions were

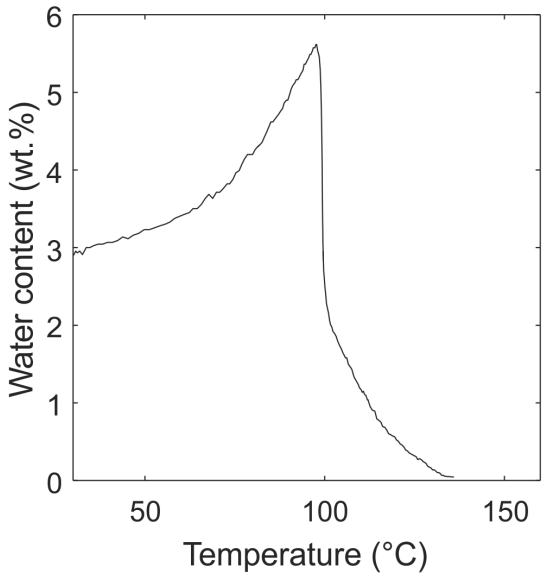

Fig. 3.6: Evolution of the water content measured at a thermocouple 5 mm beneath the heating plate versus the local temperature.

taken from the last radiograph recorded before rupture and from the directly subsequent radiograph (image acquisition frequency: 4 Hz). The negative natural logarithms of the transmissions were plotted together with the difference of the two profiles. The rupture position was allocated to the maximum difference (Fig. 3.7). The rupture positions were then inserted into the plots with the local water contents and temperatures (Fig. 3.4).

The rupture positions (within the tube interior) obtained by tensile testing at 51, 112, 125, 189, 225, and 315 seconds after contact with the heating plate (but otherwise identical parameters) were inserted in Figure 3.4. The positions of the rupture plane within the tube interior closely follow the positions of the highest moisture content.

From the measured tensile forces, wet tensile strengths (i.e. heated samples) and green tensile strengths (i.e. unheated samples) were calculated by equation 3.4. Both wet and green tensile strength depend on the initial moisture of the sand (Fig. 3.8). Green tensile strength initially increases for sands with increasing moisture, then shows a maximum of 12 kN/m^2 at approximately 3 wt.% water, which corresponds to a saturation S of 0.09 (Fig. 3.9). Finally, the green tensile strength decreases to 7.8 kN/m^2 at 5 wt.% initial water content with a saturation of 0.13. At all moisture contents, green tensile strength is higher than the related wet tensile strength. The wet tensile strength increases from 18 to 5.8 kN/m^2 for sands with 2 wt.% and 3 wt.% initial water, respectively. A further increase of the initial moisture to 5 wt.% only causes a weak increase of wet tensile strength to 6 kN/m^2.

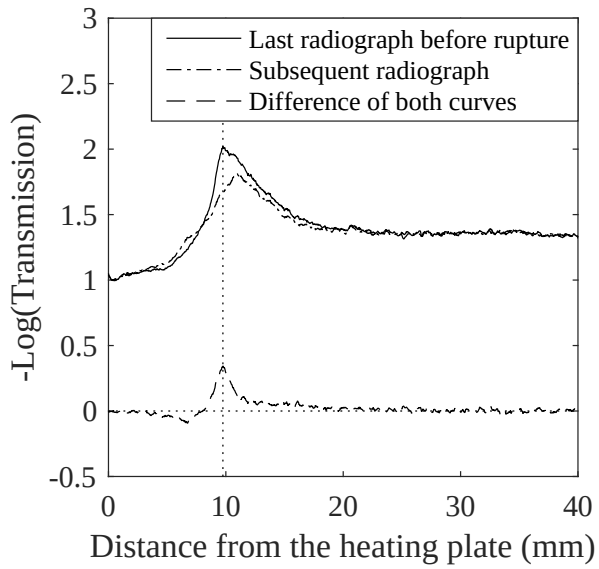

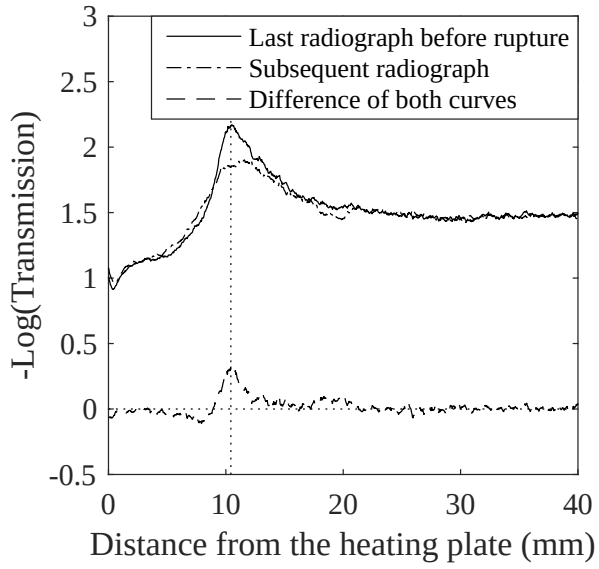

Fig. 3.7: Negative natural logarithm of the horizontal transmission profiles of moulding sands (3 wt.% initial moisture) before rupture (solid line), 0.25 s later (dash-dot line), and their difference (dash line). Upper image and lower image taken after a heating period of 125 and 189 s, respectively. The maximum change indicates the rupture position exactly.

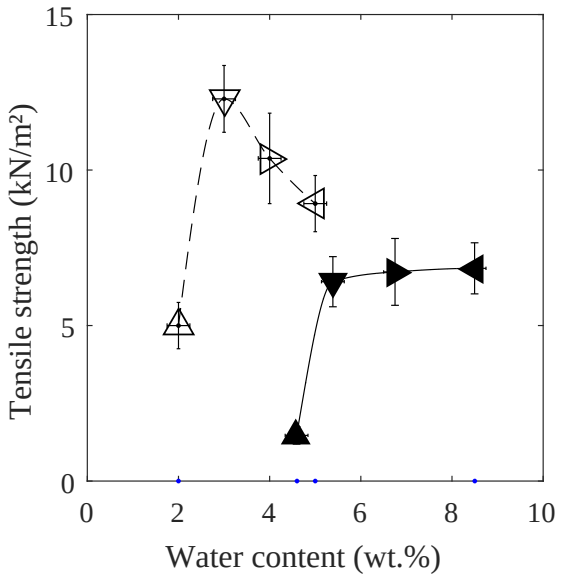

Fig. 3.8: Green (empty triangles) and wet (filled triangles) tensile strength versus moisture at the location of fracture. Triangles pointing in the same direction link experiments performed with identical moulding sand parameters i.e., link green tensile strength of a given moulding sand with the respective wet tensile strength of this sand.

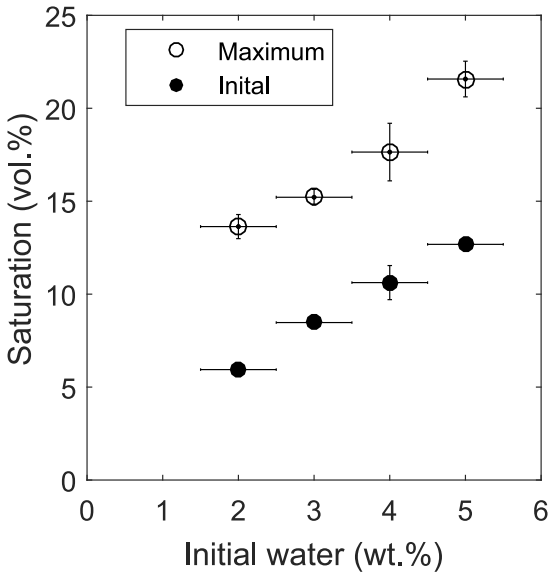

Fig. 3.9: Initial (filled dots) and maximum saturation (empty dots) plotted versus initial moisture. Saturation was calculated according to Eqn. 3.3.

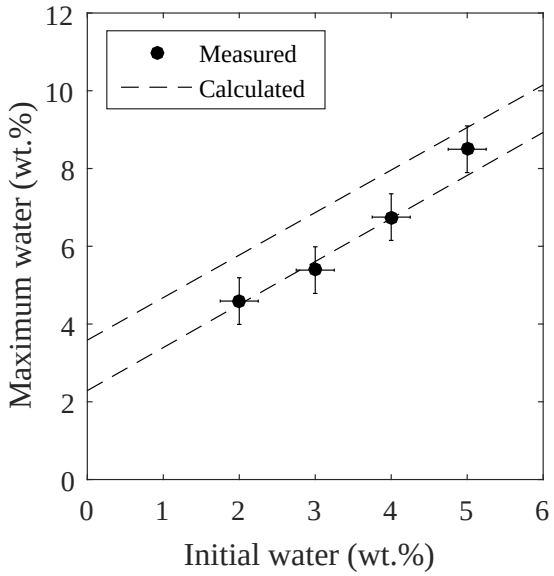

Fig. 3.10: Measured and calculated maximum water contents versus initial moisture. The calculations were performed with eq. 3.5 using a specific heat C_s of moulding sand of 0.84 and 1.26 $kJ/(kgK)$ as a lower and upper limit, respectively.

3.4 Discussion

3.4.1 Transport dependence on initial moisture

Like mentioned in the introduction, the model for water and heat transport within bentonite bonded moulding sands during casting of Kubo & Pehlke (1986) is the most detailed model, today. However, Kubo & Pehlke (1986) defined the zone boundaries by isotherms assuming that the complete pore water evaporates at 100°C. Exchange between pore water and water within the interlayers of the clay minerals was not taken into account. However, Figure 3.6 shows that water does not completely evaporate from the moulding sand at 100°C. This finding is in agreement with literature data which show that due to diffusion controlled dehydration of water within the interlayers of smectites, some water can remain within the interlayers well above 100°C (Odom 1984, Ferrage et al. 2010, Bray & Redfern 1999, Zabat & Van Damme 2000). As water remains in the moulding sand at temperatures up to 140°C, the boundary between dry zone and evaporation zone has to be moved from the 100°C isotherm to much higher temperatures.

The boundary between evaporation zone and condensation zone is marked by the location where the temperature of the sand is just reaching the boiling point of bulk water (i.e., pore water). The boundary, therefore, simultaneously represents the location of maximum water content (max). This maximum value of moisture is predominantly controlled by the heat capacity of the moulding sand environment (Kubo & Pehlke 1986, Patterson & Boenisch 1961a). Once the heat of condensation raises the temperature up to the boiling point, maximum moisture is reached and the boundary between the evaporation and the condensation zone passes this location. According to Carslaw & Jaeger (1959), maximum moisture w_{max} can be approximated by:

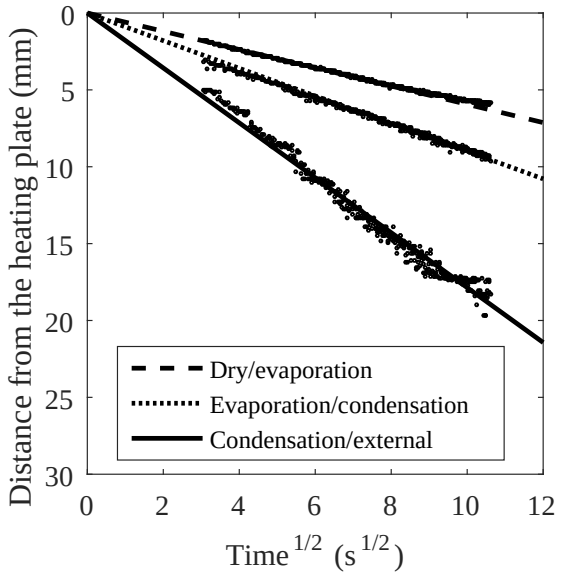

Fig. 3.11: Evolution of the zone boundaries with the square root of time in experiments with an initial moisture of 3 wt.%.

$$w_{max} = w_0 + (w_0 C_w + (1 - w_0) C_s) \frac{373 - T_0}{L_W} \tag{3.5}$$

where w_0 is the initial water, C_W the specific heat of water (approx. 4.2 $kJ/(kgK)$), C_s the specific heat of moulding sand, T_0 the initial temperature, and L_W the latent heat of evaporation (kJ/kg). The specific heat of moulding sand is between 0.84 and 1.26 $kJ/(kgK)$ (Schröder & Macherauch 1977). The water contents calculated by equation 3.5 fit well with the measured uevalues (Fig. 3.10).

Heat transfer in completely dry sand is maintained without vapour transfer i.e., mainly by conduction. Therefore, the vertical extension (Δy_{Dry}) of the dry sand zone can be approximated by (Kubo & Pehlke 1986):

$$\Delta y_{Dry} = q\sqrt{t} \tag{3.6}$$

where q is the propagation constant. In foundry industries, equation 3.6 is also commonly used to describe the movement of the boundary between evaporation and condensation zone i.e., the location of maximum moisture (Campbell 2011). In order to verify the applicability of equation 3.6 for the various zone boundaries, in-situ neutron radiography can provide the required accurate experimental data. From moisture profiles along the centre of the specimen tube, the positions of the boundaries were determined in the radiographs. The boundary between the evaporation and condensation zone was allocated by the moisture maximum during the initial 120 seconds of the experiments (after this period, water begins to vent through the tube interstice and positioning of the boundary becomes less accurate). Allocation of the boundaries between dry and evaporation zone as well as condensation and external zone is more problematic because the moisture gradients are asymptotic at these boundaries. The boundary

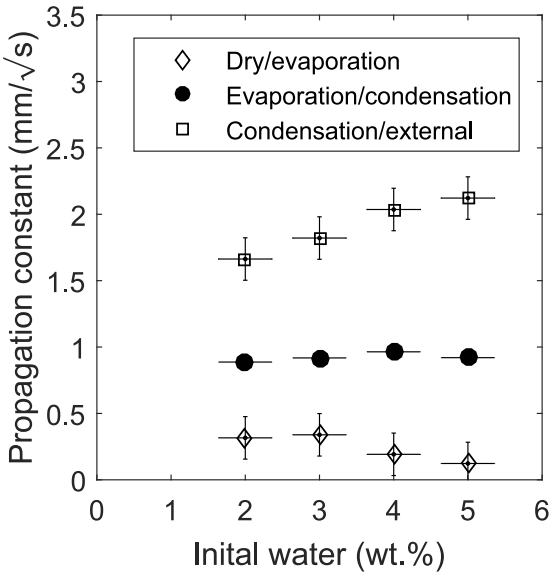

Fig. 3.12: Propagation constants of zone boundaries in moulding sands with different initial moisture contents.

between condensation and external zone, therefore, was defined by the position where the local moisture exceeds the initial water by more than 1%. The extent of the dry zone was defined by the range in which the local moisture content is less than 1% larger than at the end of the experimental run. The obtained positions of the zone boundaries can then be plotted versus the square root of time (Fig. 3.11). The data show that the propagation of all zone boundaries can be approximated by equation 3.6.

From the data in Fig. 3.11, the propagation constants q of the boundaries were calculated by least square fits. Boundary propagation constants were calculated from experiments with different initial moisture contents (2, 3, 4, and 5 wt.%; Fig. 3.12). The propagation constants of the boundary between dry and evaporation zone, which is primarily driven by heat conduction (Udell 1983, Kubo & Pehlke 1986), are nearly independent of the initial water content.

The propagation constants of the boundary between evaporation and condensation zone (Fig. 3.12) are in good agreement with Udell (1983). This author showed that the movement of the boundary is dominated by the vapour pressure gradient between dry and condensation zone, which is largely independent from initial moisture contents of the sand.

The propagation of the boundary between condensation and external zone (Fig. 3.12) is driven by water and steam diffusion (Udell 1983). The temperature at the hot end of the condensation zone is always 100°C. Consequently, the gas pressure difference between both ends of the condensation zone is constant. With increasing initial moisture both the porosity (Fig. 3.13) and the saturation of the pore space (Fig. 3.9) increase. Although the saturation of the pore space (Fig. 3.9) increases with increasing initial moisture, a significant effect of initial water content on gas permeability is not likely in the range of initial water contents of this experiment. However, the heat capacity of the mould increases with increasing initial moisture and causes an increase of the heat flux

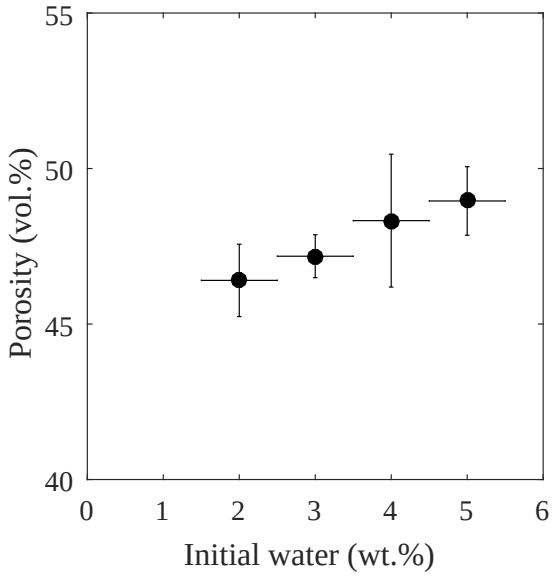

Fig. 3.13: Porosity calculated by equation 3.2 versus initial moisture.

(Fan & Wen 2002). Consequently, the propagation constant of the boundary between condensation and external zone increases (Popielarski & Ignaszak 2016).

3.4.2 Differences in tensile strength with changes in initial moisture

The dependence of green tensile strength (i.e., the tensile strength of the unheated sand) on sand moisture agrees well with the data of Patterson and Patterson & Boenisch (1961*a*), who also observed a positive correlation of tensile strength with water content followed by a negative correlation at water contents larger than approx. 3 wt.%. The observed initial increase of green tensile strength with water content is in accordance to the numerical model derived by Lu et al. (2009) for the tensile strength of moist sands. For clay, the numerical model of Lu et al. (2010) yields a negative correlation of tensile strength with increasing moisture. The observed decrease of the green tensile strength at water contents higher than 3 wt.% (which corresponds to a saturation of less than 10 vol.%), therefore, may indicate that the mechanical behaviour of the moulding sand is increasingly dominated by the clay minerals. In this context, it has to be noted that the clay minerals in moulding sands are rolled onto the quartz grains by a milling process rather than loosely mixed with quartz grains. The porosity and texture of moulding sands, therefore, is strongly influenced by the quartz grains while the clay minerals may affect the surface properties strongly.

The tensile strength of the unheated sand corresponds with the data of Patterson & Boenisch (1961*a*) which also observed a strong increase of tensile strength with an increasing water content from 2 to 3 wt.% and a strong decrease when the water content increases further. The increase in tensile strength is in accordance to the theoretical

model of Lu et al. (2009) for sands. The decrease at higher water contents indeed indicate a clay like behaviour (Lu et al. 2010).

The quantitative transport data as obtained from neutron radiographs coupled with the quantitative mechanical data obtained from tensile strength testing allow for an investigation of the effect of heat and mass transfer on the tensile strength as one of the most important properties of bentonite bonded moulding sands. The data show that the tensile strength of moulding sands, which contain heat driven evaporation and condensation zones, is significantly lower than the tensile strength of the same sands at room temperature (Fig. 3.8). Furthermore, the data show that this decrease in strength is taking place not homogeneously over the entire specimen. Consequently, a point of lowest tensile strength can be located which moves away from the heat source. The position of this weakest point depends on temperature and moisture content, both the present and in the past. In neutron radiographs, the weakest position can clearly be identified by the rupture plane. This plane coincides with the location of maximum water content and the position where the sand temperature reaches the boiling point of bulk water. The rupture plane, therefore, corresponds to the boundary of condensation and evaporation zone.

These findings partially contradict Patterson & Boenisch (1961*a*) who assumed that the supersaturation in the condensation zone (i.e, in the zone of temperatures below the boiling point of water) is the main reason for spalling. Even though water contents exceeding approx. 3 wt.% cause decreasing tensile strengths within the condensation zone, the rupture positions observed in the present experiments clearly correlate with the distinct temperature and moisture conditions marked by the boundary of condensation and evaporation zone. As the position of this boundary depends on heat and moisture transfer, the location of minimum tensile strength is transient and moves into the mould interior continuously with time.

Following the reasoning of Munkholm & Kay (2002), Heibrock et al. (2005), Forsmo et al. (2006), Zeh & Witt (2007), Vanicek (2013), capillary force is the major force binding sand grains in moist sand. With increasing water content, the saturation increases. At first, more water bridges are formed and the number of capillary contacts between water and solid surfaces increases. With a further increase of the water content, however, the pore space becomes more saturated and the water bridges merge (Lu et al. 2007, Tang et al. 2015, Song et al. 2012). The surfaces of more and more grains become completely wetted and the cohesion between the particles decreases. Above a critical water content, therefore, tensile strength decreases again.

Water content is not the only factor affecting tensile strength. The experiments show (Fig. 3.8) that the tensile strength of moulding sands with a water content for instance of 5% varies significantly with temperature. This is in accordance with Patterson & Boenisch (1961*a*) who reported that moist sand has the highest tensile strength at room temperature. The decrease of tensile strength can be explained by the temperature dependence of capillary forces. Higher temperatures lead to a decrease of the surface tension of water (Young & Harkins 1928) and lower the capillary forces. At the boiling

point, surface tension of water and capillary forces become zero. The majority of water bridges therefore do not collapse within the condensation zone but at the boiling point.

Within the evaporation zone (i.e., the zone of temperatures at and above the boiling point of water), the residual tensile strength is related to both the binding capacity of bentonite, which is largely facilitated by the remaining water molecules still adsorbed at the clay surfaces, and the cementation caused by precipitation of solutes between the sand grains from evaporating water. While the binding capability of the first decreases with increasing temperature due to increasing water desorption from the surfaces, the binding capability of the latter increases with increasing temperature. Above 140°C, finally, cementation within the virtually dry sand leads to a tensile strength which is much higher than that of moist sand (Patterson & Boenisch 1961*a*). By image analyses and consideration of earlier works, the minimum tensile strength can be precisely located at the front of the evaporation zone.

4 Effects of heat and cyclic reuse on the properties of bentonite-bonded sand

4.1 Introduction

Although the general heat-induced effects on the montmorillonite structure have been examined intensively, the effects of heat on moisture transport and, therefore, on the binding properties of bentonite-bonded moulding sands were subject to only very few studies (Holtzer et al. 2011, Bobrowski & Grabowska 2012, Żymankowska-Kumon et al. 2012). Likewise, effects of cyclic reuse on the properties of moulding sand are far from being known satisfactorily. Altered water transport within the sand during casting often is correlated with decreased wet tensile strength, which substantially degrades the quality of moulding sand. In order to study both mechanical strength and water transport properties, wet tensile testing (Schiebel et al. 2018), neutron radiography (Schillinger et al. 2011, Hall 2013, Sedighi-Gilani et al. 2013), and neutron diffraction was applied here. The simultaneous application of wet tensile testing and neutron radiography, in particular, allowed for a correlation of tensile strength with both the position of the rupture plane and the local water content of the sand with a spatial resolution in the sub-mm range and a sub-second temporal resolution (Schiebel et al. 2018). Neutron diffraction gave information about water residing within the smectite interlayers at given time and temperature. Altogether, the experiments allowed a detailed evaluation of the sand properties induced by heat and cyclic reuse. The aim of this work, therefore, was to gain deeper insights into the changes of the properties of moulding sand induced by heat or its continuous reuse.

4.2 Materials and method

4.2.1 Materials

Bentonite-bonded sand consisting of 92 wt.% quartz (average grain size approx. 0.3 mm) and 8 wt.% natural bentonite (Wyoming) was obtained from S&B Minerals (Imerys, Marl, Germany). Analysis of comparable bentonite from the same source yielded approx. 87 wt.% smectite and 13 wt.% of other minerals (mainly feldspar, quartz, and calcite; Jordan et al. (2013)).

Two suites of experiments were performed. For the first suite of experiments, aliquots of approx. 1 kg of the sand were dried at 120°C for 24 h in a drying chamber. While continuously mingling with an electric blender, the aliquots were remoistened to 3 wt.% H_2O by slowly adding approx. 30 ml water. After a further mixing for 10 min, the remoistened sand was finally aged for 24 h in an airtight bag. In total, this drying, remoistening, blending and ageing procedure was cyclically repeated 13, 22 or 25 times (the latter was used for propagation constant measurements only). The exact amount of water added in each cycle was referred to the dry weight measured directly before remoistening. For the second suite of experiments, aliquots of approx. 1 kg of moulding sand containing 3 wt.% H_2O were heat-treated for 24 h in a muffle furnace at T = 225, 330, 390, 435, 540, 645, or 750°C, remoistened (3 wt.% H_2O), blended for 10 min and aged in airtight bags for at least 24 h. As reference in both experimental suites, fresh and unused sand was dried once at 120°C for 24 h in a drying chamber, remoistened to 3 wt.% H_2O, blended for 10 min and aged in airtight bags for at least 24 h. This single drying-remoistening procedure was essential in order to obtain sand with a defined amount of water.

4.2.2 DSC and TG

The dried and un-remoistened reference moulding sand was simultaneously examined by differential scanning calorimetry (DSC) and thermogravimetry (TG) in order to determine dehydroxylation temperatures of the smectite within the moulding sand precisely. These DSC and TG data could be correlated with the temperatures of the dehydration and dehydroxylation of the moulding sand observed by neutron radiography and neutron diffraction. For the thermal analysis (Thermo Microbalance STA 449 F1; Netzsch), 63.05 mg of the sand was heated in a static argon atmosphere in a Pt-crucible (256.74 mg), which was closed with a lid with a small hole. As reference, an empty crucible of the same shape and weight was used. The heating rate was 10 K/min. The final temperature was 1000°C. A temperature calibration has been performed by using the extrapolated onset of the melting points of indium and zinc. The uncertainty of the temperature measurement is smaller than 1 K.

4.2.3 Neutron radiography time series of heated tensile testing

For the tensile tests, a two part aluminium tube was used (Fig. 2.4). The lower prismatic part had a quadratic cross section (44 mm x 44 mm) and a height of 100 mm. The quadratic cross section of the upper pyramidal part (height 20 mm) increased from 44 mm x 44 mm to 54 mm x 54 mm. The two-part specimen tube was turned upside down and filled with sieved sand. Subsequently, the sand within the tube was compressed with 1 MPa, yielding a porosity of 48 $\pm$ 3 vol.%. To simulate the casting conditions, a temperature and moisture gradient was induced by heating the sample from above with a heating plate (T = 310°C). The temperature within the sand sample was monitored

with type J thermocouples at four different distances to the heating plate. After defined heating periods (120 or 180 s), tensile tests were performed (loading ramp 50 N/s). These heating periods yielded flat rupture planes at the intended position within the sample tube. In order to quantify the binding properties of the differently treated sands, at least five wet tensile tests were performed. At least two of these tests were imaged by neutron radiography which revealed the water kinematics during the entire heating and tensile testing period. The neutron radiography time series were performed at ICON (SINQ, Paul Scherrer Institute, Switzerland; Kaestner et al. (2011)) and ANTARES (FRM II, Heinz-Maier-Leibnitz-Zentrum, Germany; Schulz & Schillinger (2015)). At ICON, samples with cyclically dried and remoistened sands were investigated using a CMOS camera (4 frames/s, spatial resolution = 0.05 mm/pixel). At ANTARES, tensile tests of heat pre-treated sands were conducted using a CCD camera (0.55 frames/s, 2x2 binning, spatial resolution = 0.15 mm/pixel). Tensile strength σ_t was calculated according to Eqn. 4.1, where Fr is the measured maximum tensile force, Fg is the weight of the upper sample part (Fig. 2.4), and A is the cross sectional area at the specimen neck.

$$\sigma_t = \frac{F_r - F_g}{A} \tag{4.1}$$

Water kinematics was quantified from neutron radiographs. The radiographs were corrected for white and dark spots, background noise, and beam fluctuations according to Hassanein et al. (2006). The local water content was calculated from corrected radiographs according to the procedure explained in detail by (Schiebel et al. 2018). In short, the water content w at the pixel position x, y and time t is:

$$w(x,y,t) = \left(ln\left(\frac{\tau_s^{cor}}{g(y)}\right) - ln\left(\frac{\tau(x,y,t)^{cor}}{g(y)}\right)\right) / \Theta_W \tag{4.2}$$

where τ^{cor} is the corrected intensity of the transmitted neutron beam measured at each pixel (x, y) in the radiograph taken at time t; τ_s^{cor} is the corrected transmission of the beam transmitting the dry sand; Θ_W is the correlation factor between water content and neutron transmission calculated from calibration measurements (Schiebel et al. 2018); $g(y)$ is the sample geometry normalisation factor, which takes account for the specific geometry of the two-part specimen tube.

Using Eq. 4.2, the local water content could be assigned to all sample positions within the radiographs (Fig. 4.1). From each radiograph, a vertical profile of water content was taken along the centre of the sample tube. In these profiles, the positions of the boundaries between the dry zone, evaporation zone, condensation zone, and external zone were determined. The boundary between evaporation zone and condensation zone was assigned to the moisture maximum. Allocation of the boundaries between dry zone and evaporation zone as well as between condensation zone and external zone was not trivial. At both boundaries, the water content of one zone continuously approached

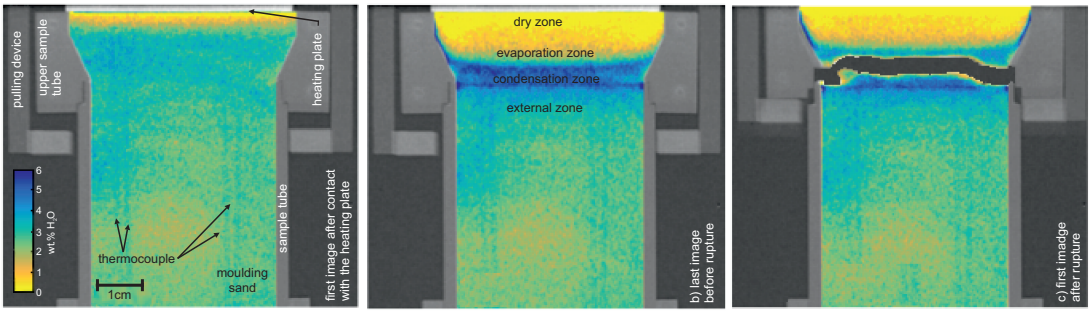

Fig. 4.1: Neutron radiographs of wet tensile testing of the reference sand. a) First radiograph taken after contact of the heater. The moisture of the sand is colour coded. b) Last radiograph taken before rupture. Dry zone, evaporation zone, condensation zone, and external zone are labelled. c) First radiograph taken after rupture.

the water content of the neighbouring zone. The boundary between condensation zone and external zone, therefore, was allocated to the position where the local moisture exceeded the initial water by more than 1%. The position of the boundary between the dry zone and the evaporation zone was assigned to the location where the moisture content is less than 0.03 wt.% H_2O.

Heat driven water kinematics within the sample tube could be characterized by the propagation constants q of the zone boundaries. According to Kubo & Pehlke (1986), these propagation constants could be approximated by:

$$q = \frac{\Delta y}{\sqrt{t}} \tag{4.3}$$

where Δy are the positions of the respective zone boundaries in the radiographs taken at time t. The propagation constants presented here were computed by linear regressions of data in plots of Δy versus $\sqrt{t}$.

4.2.4 Neutron diffraction

At the neutron diffraction beam line MIRA (FRM II, Heinz-Maier-Leibnitz-Zentrum, Germany; Georgii & Seemann (2015), Georgii et al. (2018)), both heat pre-treated and cyclically reused sands were investigated at defined conditions in order to estimate the amount of water located within the smectite interlayers. Compared to X-ray, neutrons strongly interact with water, leading to higher intensities of the smectite reflections in moist condition. With decreasing water content, the intensities also decrease.

For the experiments, the moist sand (3 wt.% H_2O) was filled into an aluminium vial (Ø 18 mm, height 50 mm) and compressed with 1 MPa. Immediately after compaction, a lid was screwed on the vial. The lid had a hole (Ø 3 mm) for pressure release by venting air and water vapour. Through the hole, a thermocouple (Ø 2 mm) was fed into the vial. The thermocouple tip was positioned in the centre of the sample. The semi-open vial

design closely matched the conditions within the moulding sand during casting, where ambient pressure was fairly maintained in the open pore system by transport of air and water vapour away from the hot mould cavity towards the neighbouring colder areas.

The vial with the moist sand was heated with a furnace mounted on the instrument thus allowing for in-situ neutron diffraction from room temperature to 135 °C in steps of 5 or 10 K. At each step, the temperature was held for 40 or 60 min to evaluate the swelling state of smectites. During both heating and holding, diffraction patterns were continuously taken at 5-35° 2Θ with a step width of 0.4° 2Θ and an exposure time of 2 s. Before heating and at the end of each experiment, diffraction patterns were taken from 5° to 120° 2Θ. By the positions of the quartz peaks (determined by basic Gaussian fitting after background subtraction), the wavelength (4.502 ± 0.009 Å) was continuously monitored. The quartz reflection data used for the calculation were taken from Ogata et al. (1987) (d_{100} = 4.2277 Å, d_{101} = d_{011} = 3.3230 Å). From each diffraction pattern, the average d_{001} value of the smectite was calculated by fitting the peak with a single Gaussian function after a background subtraction and an integration of the previous and subsequent scan.

4.2.5 SEM

Scanning electron microscopy images were taken from sand flakes coated with a carbon layer (≈ 10 nm). The sand flakes were made from moist sand (3 wt.% H_2O) by compression with 1 MPa and vacuum drying of the pressed flakes at room temperature. Images were taken with a Hitachi SU5000 microscope equipped with a field emission gun. Semi-quantitative chemical analyses by energy-dispersive spectroscopy (EDX, AzTec, Oxford Instruments) were performed using an accelerating voltage of 20 kV and a working distance of 10 mm.

4.3 Results

4.3.1 Thermal analyses

Between room temperature and 200°C, TG showed a weight loss of only 0.06 wt.%, which can be regarded as meaningless. From 200°C to 670°C, a continuous mass loss of 0.043 wt.% occurred (Fig. 4.2). At 500°C, a significant change of the mass loss rate took place. At 725°C, the mass loss rate decreased to almost zero. Therefore, the weight loss from 725-1000°C was smaller than 0.05 wt.%.

DSC (Fig. 4.2) showed an endothermic peak beginning at 400°C with a maximum at 500°C, correlating with the observed change in mass loss rate by TG. The peak at 500°C overlapped with a large endothermic peak at 576°C. A third peak with a maximum at 670°C (ending at 720°C) correlated with a strong mass loss in TG. Further extensively overlapping endothermic peaks could be observed at temperatures above 800°C.

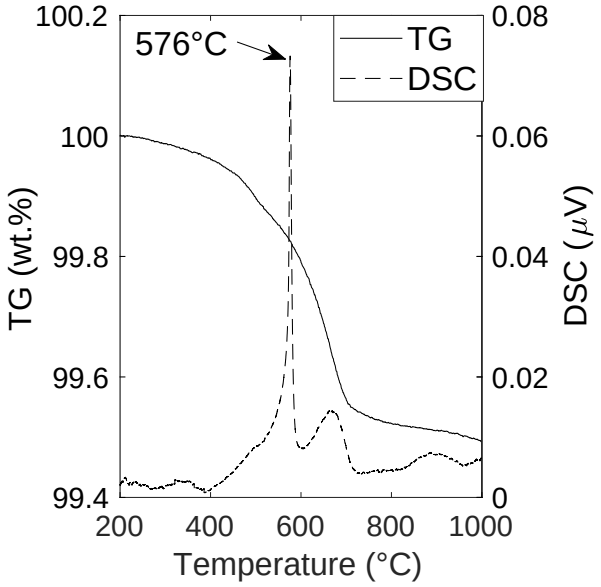

Fig. 4.2: DSC and TG curve (heating rate 10 K/min) of a bentonite moulding sand with a bentonite content of 8 wt.%. For the analysis, the reference sand was used, which previously was subject to a single drying (120°C), remoistening (3 wt.%), blending and ageing procedure. The α-quartz transformation starts at 573°C and reaches maximum transformation rate at 576°C.

4.3.2 Wet tensile strength of heat pre-treated and cyclically reused sands

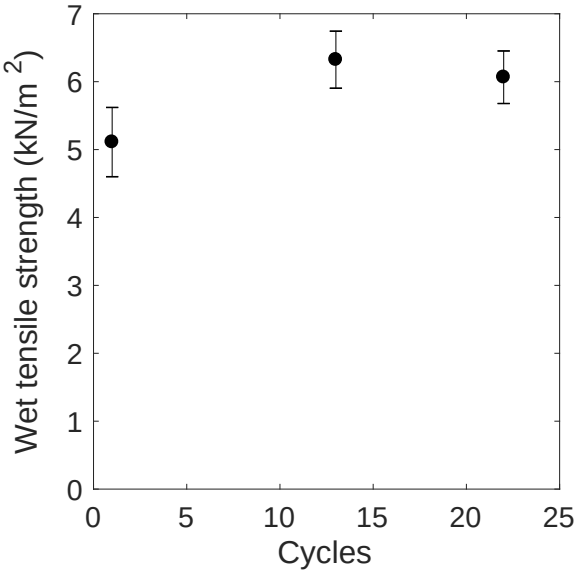

Fig. 4.3: Wet tensile strengths of moulding sands subjected to various numbers of drying-remoistening cycles.

In the reference sand, rupture occurred at the boundary between evaporation and condensation zone (Fig. 4.1c). This boundary coincided with the 100°C isotherm (Schiebel et al. 2018). The experiments with cyclically reused sands showed that the coincidence of the rupture position with this boundary was not significantly affected by the number of cycles. Likewise, the tensile strengths of cyclically reused sands revealed

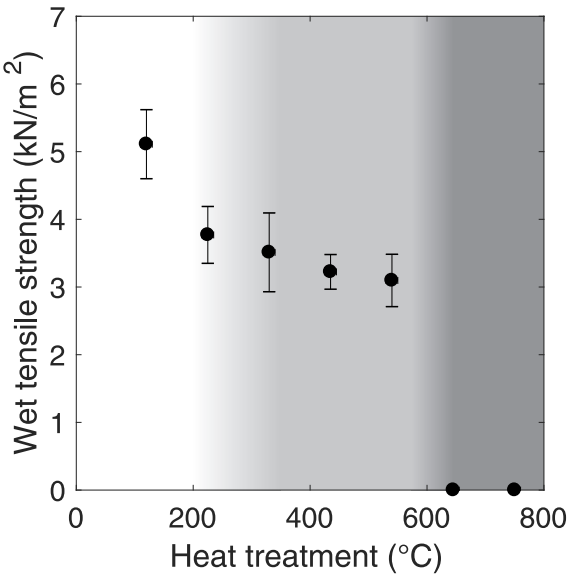

Fig. 4.4: Wet tensile strengths of moulding sands pre-treated at different temperatures. Different degrees of smectite dehydroxylation (Fig.4.2) are indicated by different greyscales.

no significant dependence on the number of cycles (Fig. 4.3) and remained close to the value of 5.2 $\pm$ 0.5 kN/m^2 which had been obtained for the reference sand.

The tensile strengths of heat pre-treated sands, however, were generally lower than the strength of the reference sand (Fig. 4.4). Sand pre-treated at 225°C revealed a tensile strength of 3.8 $\pm$ 0.4 kN/m^2. Pre-treatment at 540°C yielded a value of 3.1 $\pm$ 0.4 kN/m^2. For sands pre-treated at temperatures of 645°C and higher, tensile strengths were below detection limit. The sand in the dry zone of these samples just fell apart and disintegrated into grains upon pulling the upper part of the sample tube. This behaviour was different to all other sands examined here, which had significant tensile strengths in the dry zone.

4.3.3 Dehydration behavior of the sand with different pre-treatments

The drying rate increases continuously until it reaches a maximum. The maximum of the dehydration rate is for the reference sand between 115°C and 105°C for sandas pre-treated with 540°C. The dehydration of the reference sand is completed at 130°C. For sands pre-treated with 540°C the dehydration is finished at approx. 120°C.

The TG datas of the reference sand and the cyclic treated sand are identical (Fig. 4.5). Sands pre-treated with 225°C show in the TG measurements a faster dehydration. The TG curves and, therefore, the dehydration behaviour of sand treated with 330°C and 225°C are identical. A temperature pre-treatment of 540°C causes a further decrease of the dehydration temperature measured by TG.

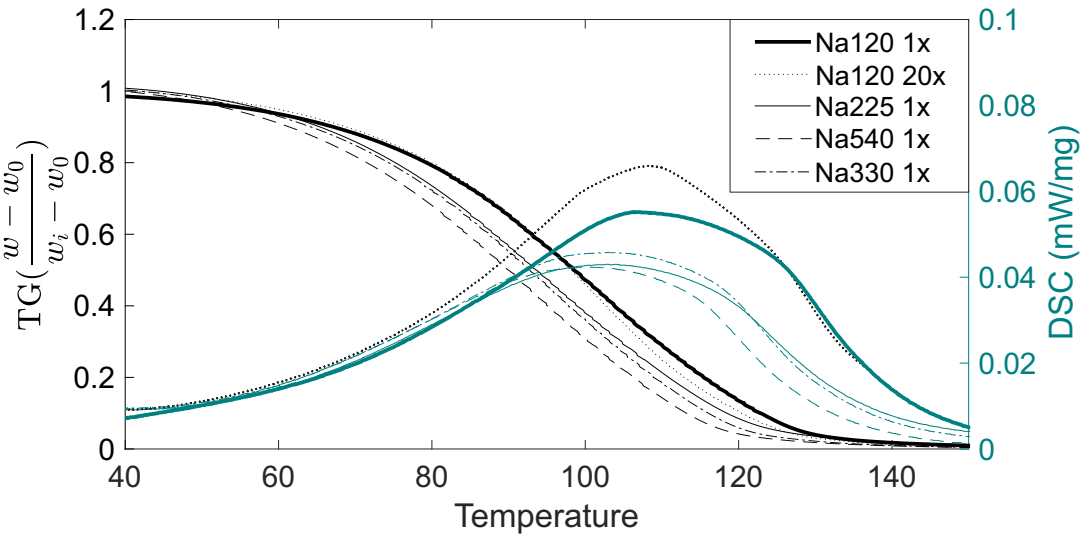

Fig. 4.5: TG (black lines) and DSC (turquoise lines) curves of the reference sand (thick solid lines), cyclic treated sands (dotted lines) and temperature pre-treated sands (solid lines-dashed lines).

4.3.4 Water kinematics in the sand column

Evaporation of water in the sand started instantaneously when contact to the heating plate had been established. The generated steam diffused into the lower parts of the specimen and condensed. At a given position within the sand column, therefore, the local moisture first increased and then decreased as the dry zone advanced further. This water transport behaviour was present in all samples examined here (Fig. 4.6). A more detailed evaluation of the transport by a quantitative comparison of the propagation constants of the zone boundaries, however, revealed some differences among the different sands (Fig. 4.7, 4.8).

The propagation constants of the reference sand were 0.15 ± 0.01 mm/$\sqrt{s}$, 0.85 ± 0.02 mm/$\sqrt{s}$, and 2.80 ± 0.15 mm/$\sqrt{s}$ for the boundaries between the dry zone and evaporation zone, the evaporation zone and condensation zone, and the condensation zone and external zone, respectively. With an increasing number of drying-remoistening cycles, the propagation constants of the zone boundaries did not significantly change (Fig. 4.7). Sands pre-treated at 225°C or 330°C also did not show relevant differences (Fig. 4.8). After a pre-treatment at 390°C, however, the propagation constant of the boundary between the condensation zone and external zone increased to 3.9 ± 0.1 mm/$\sqrt{s}$. Upon increasing the temperature of the heat pre-treatment to 750°C, the propagation of the boundary of the condensation zone and external zone increased to 6.4 mm/$\sqrt{s}$ (single measurement). In comparison to the propagation of the boundary of the condensation zone and external zone, the effect of pre-treatment on the propagation of the other two boundaries was less prominent.

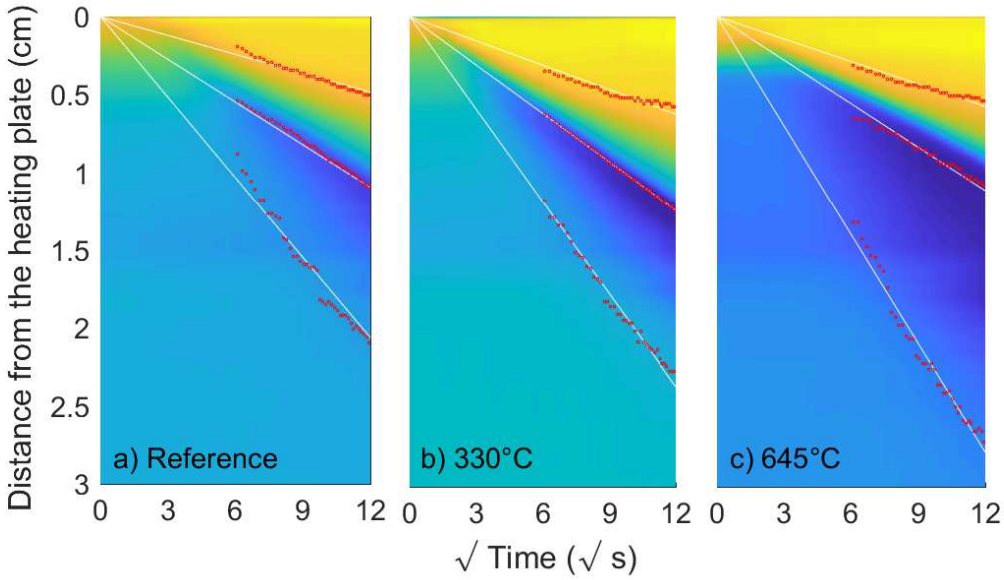

Fig. 4.6: Heat-driven movement of the water within the centre of the sample tube (same colour code as in Fig. 4.1) depicted by plotting a square root of time sequence of vertical profiles of neutron radiographs. a) Reference sand; b) Sand pre-treated at 330°C; c) Sand pre-treated at 645°C. The red dots mark the measured boundaries between (from top to bottom) the dry zone, evaporation zone, condensation zone, and the external zone. The white lines are the linear regressions of the measured data points.

The maximum water contents measured at the boundary between evaporation zone and condensation zone remained at 5 ± 0.5 wt.%, independent of cyclic reuse or of heat pre-treatment (Fig. 4.9) .

4.3.5 Water in smectite interlayers at temperatures up to 130°C

Reference sand

The 001-reflection of smectite was measured in all sands while applying a defined heating protocol. Before heating, the d_{001} value of the smectite in the reference sample was 17.1 Å (Fig. 4.10a). With increasing temperature, the *d* value decreased reflecting a release of interlayer water. The water release rate, however, was not constant. Heating to 100°C and keeping the temperature for about one hour caused only a slight decrease of the d_{001} value to 15.9 Å. Heating and keeping the sand at 110°C for almost one hour led to an almost continuous decrease of the *d* value to 13.1 Å. Heating to 120°C and keeping the temperature for another hour caused a further decrease of the *d* value. Upon reaching 130°C, the 001-refection disappeared in the background with a final *d* value of approximately 9.7 Å.

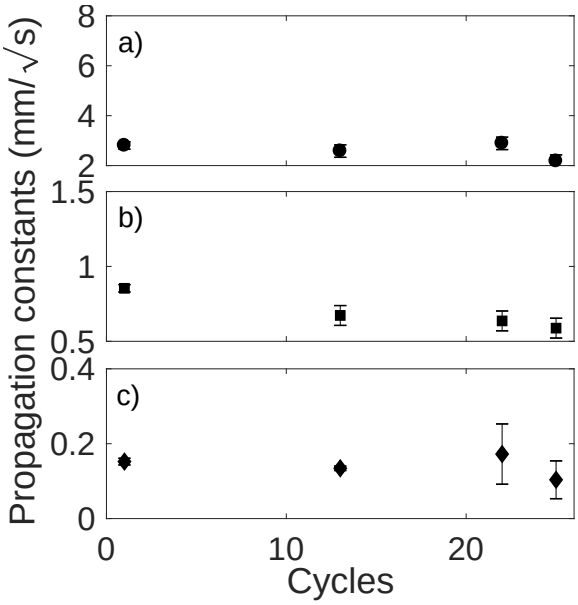

Fig. 4.7: Propagation constants of the zone boundaries calculated from neutron radiographs of cyclically reused sands plotted versus the number of cycles. a) Boundary of condensation and external zone; b) Boundary of evaporation zone and condensation zone; c) Boundary of dry zone and evaporation zone.

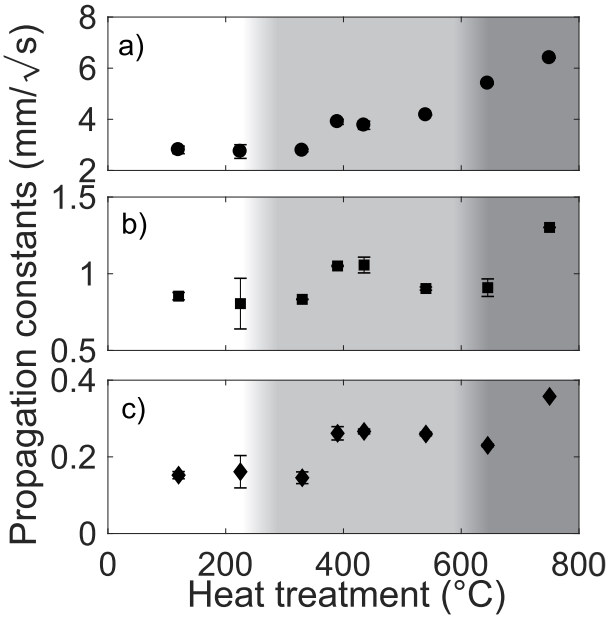

Fig. 4.8: Propagation constants of the zone boundaries calculated from neutron radiographs of heat pre-treated moulding sands plotted versus pre-treatment temperature. a) Boundary of condensation zone and external zone; b) Boundary of evaporation zone and condensation zone; c) Boundary of dry zone and evaporation zone. Different degrees of smectite dehydroxylation (Fig.4.2) are indicated by different greyscales.

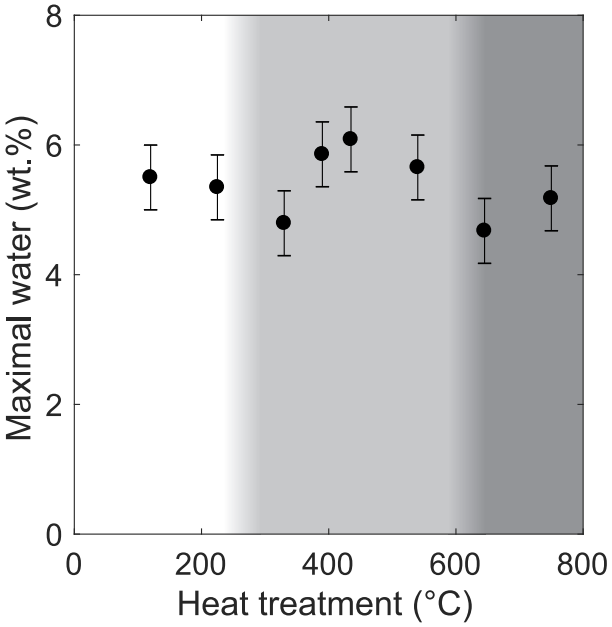

Fig. 4.9: Maximum water content at the boundary between evaporation zone and condensation zone for heat pre-treated sands during wet tensile strength testing. Different degrees of weight loss during heat pre-treatment as detected by thermal analyses (Fig. 4.3) were indicated by different greyscales.

Cyclically reused sands

The temperature dependence of d_{001} values of cyclically reused sands revealed some differences (Fig. 4.10b). During heating to 100°C, the d_{001} value was approx. 19.6 Å. Upon heating to 110°C, the *d* value decreased to approx. 14.9 Å, stayed for some period, then decreased to approx. 13.7 Å. Even after heating to 120°C, the *d* value remained at approx. 13.7 Å for some time before it dropped and stayed at 12.5 Å. Upon heating to 130°C, the 001-reflection disappeared in the background with a final *d* value of approx. 10.5 Å. In summary, cyclically reused sands showed significantly higher initial and final *d* value (19.6 and 10.5 Å).

Heat pre-treated sands

Sands pre-treated at T $\leq$ 435°C (Fig. 4.10c) showed a very large initial *d* value of approx. 20 Å. The spacing then decreased to approx. 15.7 Å where it remained until the temperature reached 115°C. At 115°C, the *d* value then dropped to 13 Å. Upon heating to 120°C, a further plateau was obtained at 12 Å. The reflection finally disappeared in the background with a *d* value of approx. 9.6 Å. In summary, a pre-treatment at *T* $\leq$ 435°C led to an initial *d* value, which was significantly higher than the one of the reference smectite. The final *d* value was similar to the one of the reference.

Amount of interlayer water

The *d* value of the smectites allowed a rough estimation of the amount of water, which is present within the smectite interlayers. Taking the results of Teich-McGoldrick et al. (2015), a d_{001} value of 16 Å (18 Å) corresponded to approximately 5 (6.5) molecules of water per $O_{10}(OH)_2$. Approximating the molar weight of the dry smectite with 370

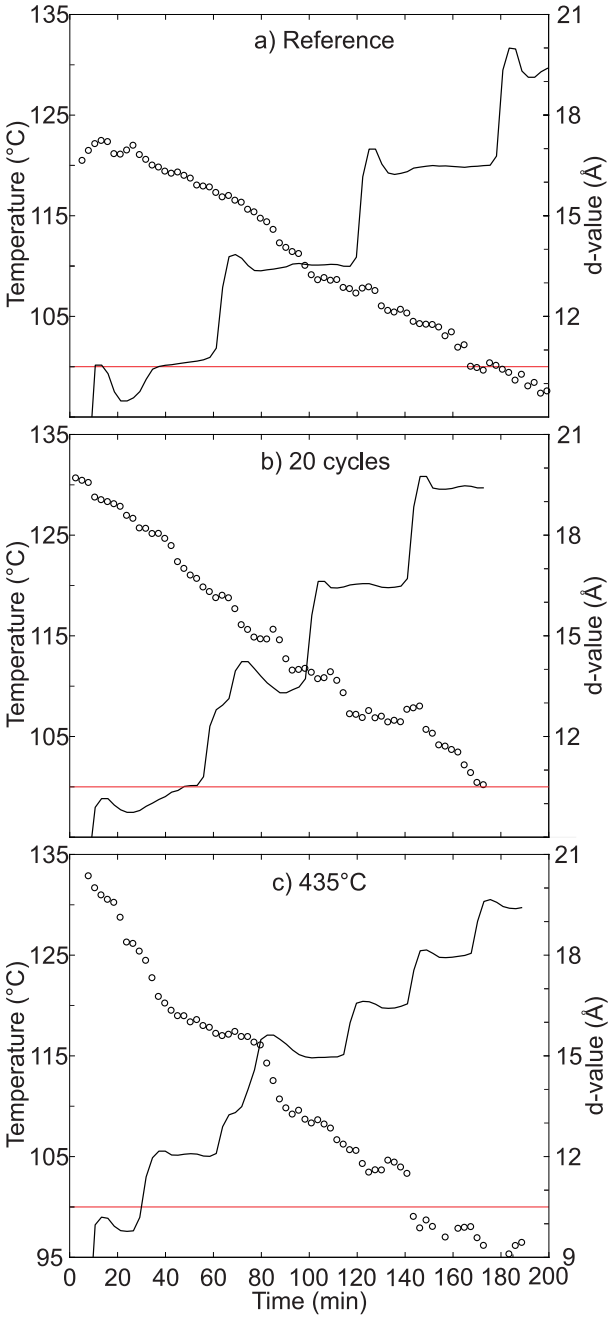

Fig. 4.10: Neutron diffractometer analyses conducted during thermal dehydration of the reference sand (a), cyclically reused sand (b), and sand pre-treated at 435°C (c). The d_{001} value of smectite (empty circles) and sample temperature (black line) are plotted versus time. The red lines mark the 100°C levels and illustrate the periods of the sample temperature exceeding 100°C.

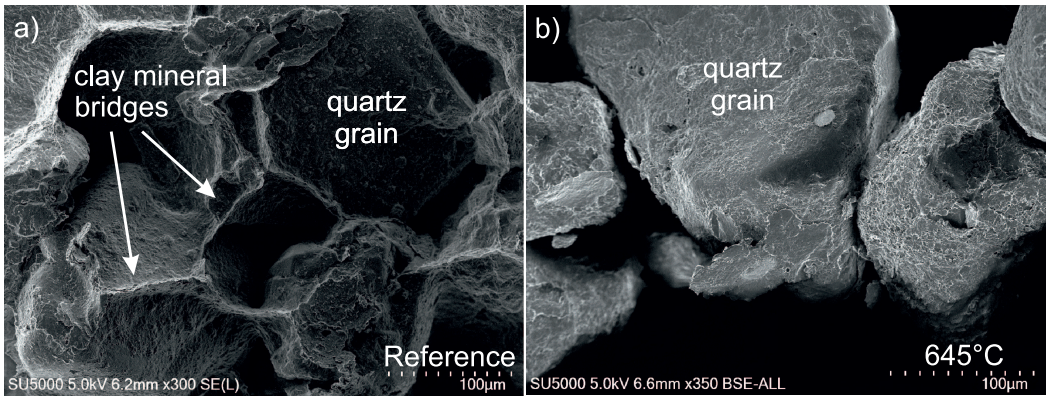

Fig. 4.11: SEM images of air-dried sand. a) Reference sand; b) Sand pre-treated at 645°C.

g/mol per formula unit, one gram of dry smectite absorbed approx. 0.25 g (0.31 g) in order to attain a layer-to-layer distance of 16 Å (18 Å). The moulding sand with a bentonite content of 8 wt.%, therefore, contained 1.7 (2.2) wt.% of water within the smectite interlayers at these swelling states.

4.3.6 Sand structure

The SEM images (Fig. 4.11) of the reference sand showed that the quartz grains were covered with smectite completely. The covering film interconnected neighbouring quartz grains and, thus, built up a three-dimensional framework in which the quartz grains were embedded. Contrarily, sands pre-treated with temperatures of 645°C lacked the interconnecting three-dimensional framework and were composed of only partially connected quartz grains.

4.4 Discussion

Temperature dependence of tensile strength

In unheated moist moulding sand, capillary force controls tensile strength (Munkholm & Kay 2002, Heibrock et al. 2005, Forsmo et al. 2006, Zeh & Witt 2007, Vanicek 2013). The capillary force is mainly depending on surface tension and can be assessed by sand suction (Lu et al. 2007). Furthermore, capillary force depends on the swelling state of the smectites, which in unheated sand affects the amount of water in the pore space. All in all, tensile strength, therefore, is affected by the strength of water sorption forces, the water-air interface energy within the pores (Kayser 1976, Wiebe et al. 1998), the relative pore humidity, and the pore structure, which changes with the swelling state of smectites (Wiebe et al. 1998).

In heated wet tensile testing as well as during casting, moulding sand develops a non-uniform temperature and moisture gradient (Kubo & Pehlke 1986). A zone with

low tensile strength, therefore, forms which becomes manifested by the rupture position in tensile tests. In all experiments except the ones with sands pre-heated at $T > 645°C$, rupture occurred at the 100°C isotherm (Fig. 4.2). This isotherm corresponded to the boundary between evaporation zone and condensation zone (Kubo & Pehlke 1986), where the pore water began to evaporate and the relative pore humidity was 100%. This pore water evaporation and the concomitant decrease in capillary force, therefore, can be regarded as the major causes for the decrease in tensile strength at this boundary. The retaining minimum tensile strength mainly depended on the stability of the clay mineral bridges (Fig. 4.11), which is related to the swelling state of the smectites (Laird 2006).

Although the location of weakest strength in the sand column correlated with the 100°C isotherm, the tensile strength at this weakest location was not always the same. The temperature dependence of the tensile strength, therefore, cannot explain the observed differences among the sands. The integrity of the smectite structure and composition has to be taken into account as well. The intactness of smectites may play a role by affecting the water contents of the different sands. In the sand, water resided in three different reservoirs: pores, surfaces, smectite interlayers. In order to understand the different tensile strengths of the sands, knowledge of the amounts of water within the respective reservoirs is important. These amounts were influenced by the heat-driven water kinematics within the sand column, and, on a smaller scale, by the retention capacity of the smectite interlayers or, from a more general perspective, by the water kinematics between the three reservoirs.

The comparision of the diffusion constant of water molecules in and out of the smectite interlayers ($\approx 9 \cdot 10^{-9}$ $m^2 s^{-1}$; Bourg & Sposito (2010), Holmboe & Bourg (2013)) with the propagation constant of the boundary between the evaporation zone and condensation zone ($\approx 8 \cdot 10^{-7}$ $m^2 s^{-1}$; Fig. 4.7, 4.8) shows that hydration and dehydration of the smectite interlayers is orders of magnitudes slower than the heat driven movement of water within the pore system of the moulding sand. This is confirmed by neutron diffraction, which showed that certain hydration states were stable for much longer time scales (Fig. 4.10) than relevant for moulding sand stability, both in wet tensile testing and in foundry industry. Therefore, absorption capacity of the smectite interlayers played an inferior role in buffering the rising supersaturation at the advancing condensation zone.

The maximum water content at the boundary between evaporation zone an condensation zone was predominantly controlled by the heat capacity of the moulding sand (Kubo & Pehlke 1986). Because smectite alteration did not strongly influence the specific heat of the sand, the maximum water contents of the different sands did not differ significantly (Fig. 4.9).

At the boundary between evaporation zone and condensation zone, therefore, not only the temperature and porosity but also the total water content was independent of the sand pre-treatment. Thus, the stability of the clay mineral bridges likely was the main factor determining the minimum tensile strength at the rupture plane.

Effects of temperature and water kinematics on tensile strength

In unheated moist moulding sand, capillary force controls tensile strength (Munkholm & Kay 2002, Heibrock et al. 2005, Forsmo et al. 2006, Zeh & Witt 2007, Vanicek 2013). The capillary force is mainly depending on surface tension and can be assessed by sand suction (Lu et al. 2007). Furthermore, capillary force depends on the swelling state of the smectites, which in unheated sand affects the amount of water in the pore space. All in all, tensile strength, therefore, is affected by the strength of water sorption forces, the water-air interface energy within the pores (Kayser 1976, Wiebe et al. 1998), the relative pore humidity, and the pore structure, which changes with the swelling state of smectites (Wiebe et al. 1998).

In heated wet tensile testing as well as during casting, moulding sand develops a non-uniform temperature and moisture gradient (Kubo & Pehlke 1986). A zone with low tensile strength, therefore, forms which becomes manifested by the rupture position in tensile tests. In all experiments except the ones with sands pre-heated at $T > 645°C$, rupture occurred at the 100°C isotherm (Fig. 4.2). This isotherm corresponded to the boundary between evaporation zone and condensation zone (Kubo & Pehlke 1986), where the pore water began to evaporate and the relative pore humidity was 100%. This pore water evaporation and the concomitant decrease in capillary force, therefore, can be regarded as the major causes for the decrease in tensile strength at this boundary. The retaining minimum tensile strength mainly depended on the stability of the clay mineral bridges (Fig. 4.11), which is related to the swelling state of the smectites (Laird 2006).

Although the location of weakest strength in the sand column correlated with the 100°C isotherm, the tensile strength at this weakest location was not always the same. The temperature dependence of the tensile strength, therefore, cannot explain the observed differences among the sands. The integrity of the smectite structure and composition has to be taken into account as well. The intactness of smectites may play a role by affecting the water contents of the different sands. In the sand, water resided in three different reservoirs: pores, surfaces, smectite interlayers. In order to understand the different tensile strengths of the sands, knowledge of the amounts of water within the respective reservoirs is important. These amounts were influenced by the heat-driven water kinematics within the sand column, and, on a smaller scale, by the retention capacity of the smectite interlayers or, from a more general perspective, by the water kinematics between the three reservoirs.

The comparision of the diffusion constant of water molecules in and out of the smectite interlayers ($\approx 9 \cdot 10^{-9}$ $m^2 s^{-1}$; Bourg & Sposito (2010), Holmboe & Bourg (2013)) with the propagation constant of the boundary between the evaporation zone and condensation zone ($\approx 8 \cdot 10^{-7}$ $m^2 s^{-1}$; Fig. 4.7, 4.8) shows that hydration and dehydration of the smectite interlayers is orders of magnitudes slower than the heat driven movement of water within the pore system of the moulding sand. This is confirmed by neutron diffraction, which showed that certain hydration states were stable for much longer time scales (Fig. 4.10) than relevant for moulding sand stability, both in wet tensile testing and

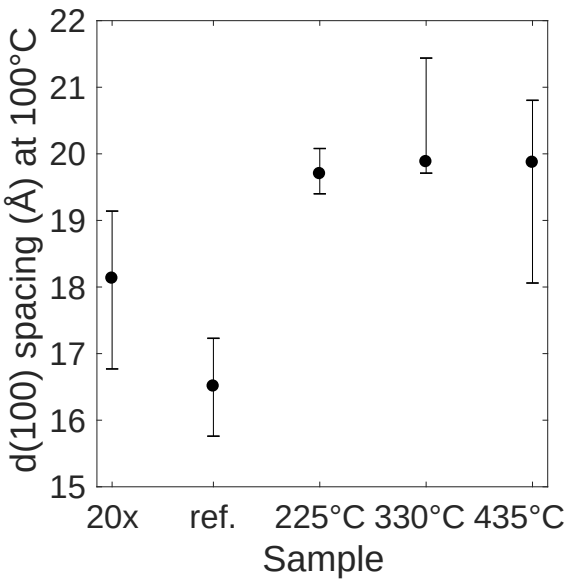

Fig. 4.12: Median d_{001} value at 100°C of the reference sand and temperature treated sand.

in foundry industry. Therefore, absorption capacity of the smectite interlayers played an inferior role in buffering the rising supersaturation at the advancing condensation zone.

The maximum water content at the boundary between evaporation zone an condensation zone was predominantly controlled by the heat capacity of the moulding sand (Kubo & Pehlke 1986). Because smectite alteration did not strongly influence the specific heat of the sand, the maximum water contents of the different sands did not differ significantly (Fig. 4.9).

At the boundary between evaporation zone and condensation zone, therefore, not only the temperature and porosity but also the total water content was independent of the sand pre-treatment. Thus, the stability of the clay mineral bridges likely was the main factor determining the minimum tensile strength at the rupture plane.

Tensile strength of cyclically reused sands

Comparing the propagation constants and the tensile strengths of the reference sand and the cyclically reused sands, no significant changes with an increasing number of drying and remoistening cycle could be observed (Fig. 4.7).

The neutron diffraction data at 100°C showed that the d_{001} value of smectites in the reference sand as well as in the cyclically reused sands roughly corresponded to three water layers (Zheng et al. 2010, Villar et al. 2012, Holmboe & Bourg 2013). The amount of water within these smectite interlayer was approximately between 1.7 and 2.2 wt.%. Thus, about the half of the total water at the boundary between evaporation zone and condensation zone (approx. 5 wt.% (Fig. 4.9)) was located within the smectite interlayers.

Note, the d values of the smectites in the cyclically reused sands were approx. 1.5 Å larger than in the reference sand (Fig. 4.10). In agreement with Heuser et al. (2014), we suggest that these higher initial d values were likely caused by mechanical effects

originating from repeated mixing (Oscarson et al. 1990, Alonso-Santurde et al. 2012) rather than by steam (Couture 1985, Oscarson & Dixon 1989). If steam were the cause, smectite in the reference sand would show a high d value, too, because a single steam treatment would likely be effective enough to expand the layers.

Tensile strength of sands pre-treated at T = 225-330°C

The effect of heat pre-treatment was investigated by a separate suite of experiments. Neutron radiography experiments with sand pre-treated at temperatures up to 330°C revealed no significant alteration of the propagation constants (Fig. 4.8). However, neutron diffraction analyses during dehydration of these pre-treated sands showed (Fig. 4.10) that the initial smectite d_{001} values at temperatures up to 100°C were significantly larger than in the reference sand. A mechanical cause for these increased initial d values (as in the case of cyclically reused sands) can be dismissed because the mechanical treatment was as long and strong as in the reference sand. Thus, the heat pre-treatment at T = 225-330°C has to be the reason for these increased d values. In agreement with the results obtained by thermal analysis, the pre-treatment may only have led to minor changes of the smectite structure if any. In the case of small interlayer cations such as Li, Cu, Zn, migration into tetrahedral sheets (McBride & Mortland 1974) or octahedral sites (Madejová et al. 1996) might be considered as an adequate structural modification. Larger cations (Na, Ca) migrate into these sites less likely (Calvet & Prost 1971). However, also for smectites with larger cations like Na^+, K^+, Ca^{2+} small changes in properties upon heating temperature were reported in literature (Chorom & Rengasamy 1996, Komadel et al. 2005). We propose that irreversible minor structural changes induced by the heat pre-treatment were apt to reduce the forces between the smectites bridging two quartz grains (Laird 2006) and, therefore, were responsible for the decrease in wet tensile strength, which was obtained for sands pre-treated at temperatures of 225-330°C.

Tensile strength of sands pre-treated at T > 330°C

Pre-treatments of sands at T > 330°C led to changes in water kinematics that were more substantial. All three propagation constants were increased in sands pre-treated at temperatures between 390 and 540°C (Fig. 4.8; range marked in pale greyscale). The increase of propagation constants correlated with the observed mass loss by TG and the endothermic DSC-peak reaching maximum at 500°C (Fig. 4.3). These thermal analysis results very likely reflect a loss of tightly bound water (Kuligiewicz & Derkowski 2017) or of an early loss of hydroxyl-groups (Emmerich et al. 1999), although for *cis*-vacant montmorillonites dehydroxylation was found to take place not below 600°C (Wolters & Emmerich 2007). Irrespective of the removal of tightly bound water or hydroxyl-groups, the changes of smectites by the heat pre-treatment were the likely cause of the observed tensile strength reduction.

It needs to be noted, however, that the smectites located at the rupture plane (i.e., at 100°C isotherm of the sample column) still contained three layers of water. This

high amount of interlayer water was likely facilitated by the high partial pressure of water in the pore space of the sand (c.f., Emmerich et al. 2015). This interlayer water is indicative of the existence of some layer charge and is a clear indication for only minor or moderate changes of the smectites at temperatures below 645°C.

Pre-treatments at $T \geq 645$°C caused a strong increase of the propagation constant of the boundary between the condensation zone and external zone (Fig. 4.8; range marked in dark greyscale). Pre-treatments at 750°C, led to significantly higher values of all propagation constants. The increased water transport rates and decreased tensile strengths correlated with the observed DSC-peak at 670°C (Fig. 4.3), which is typically for a dehydroxylation of *cis*-vacant montmorillonite (Emmerich et al. 2009).

SEM of these samples showed quartz grains being located individually rather than interconnected by smectite coatings (Fig. 4.11b). The most prominent property change, however, was that sand pre-treated at $T \geq 645$°C did not harden in dry state but transformed into loose grains. The tensile strengths of these sands, therefore, decreased to zero in all areas where the water bridges between the grains were evaporated completely. Consequently, the position of the rupture plane of these sands shifted into the dry zone.

5 Comparison of moulding sands bonded with sodium and calcium bentonites

5.1 Introduction

In smectites, the charge of the tetrahedral and octahedral layer is compensated by the interlayer cation. Depending on the kind of cation, the properties of montmorillonite strongly differ. Rheological properties such as viscosity, gel strength, yield stress, and thixotropic behaviour are affected by the layer charge (Christidis et al. 2006) as well as the cation exchange capacity and the ion exchange selectivity (Maes & Cremers 1977). The swelling behaviour and, therefore, the water uptake and release from the interlayer space of smectites are strongly affected by the charge of the exchangeable cations (MacEwan & Wilson 1980, Laird et al. 1995). Compared to montmorillonites without Ca^{2+}, montmorillonites containing Ca^{2+} have a considerable different swelling behaviour (Zheng et al. 2010). Thereby, it is of particular importance whether Ca^{2+} is incorporated into the montmorillonite structure or not.

The differences in swelling behaviour and rheological properties of smectites are reflected in the heat and water transport within moulding sands and the mechanical properties of the sands. Both green as well as wet tensile strength differ strongly depending on the chemical composition of the bentonite. In comparison to calcium bentonite bonded sand, sodium bentonite bonded sands have a significantly higher wet tensile strength (Odom 1984, Patterson & Boenisch 1961*a*). Consequently, Na-bentonite is the preferably used bonding agent in sand casting.

The study of the mechanical and transport properties of Ca-bentonite bonded quartz sands, however, can provide useful information about the interplay between the chemical composition of the bentonites on the one hand and the moulding sand properties on the other hand. Furthermore, the investigation of the property change of Ca-bonded sands by cyclic reuse or temperature pre-treatments provides also valuable insights into the binding mechanism of the more significant Na-bonded sand.

5.2 Specific experimental details

5.2.1 Materials

Quartz sand (average grain size approx. 0.3 mm) mixed with 8 wt.% natural calcium bentonite (Bavaria, Germany) was provided by S&B Minerals (Imerys, Marl, Germany). Grain size, bentonite content and sand moisture were equal to the Na-bentonite bonded sand used in the previous experiments (see foregoing chapters).
Three experimental suites were conducted:

- In the first suite of experiments, aliquots of approx. 1 kg sand were dried in a drying chamber at 120°C, re-moistened with 2, 3, 4 or 5 wt.% H_2O and mingled for 10 minutes in a kneading machine.
- In the second suite of experiments, aliquots of approx. 1 kg sand were cyclically dried in a drying chamber at 120°C, re-moistened with 3 wt.% H_2O and mingled for 10 minutes in a kneading machine. This procedure was repeated for 13 or 23 times, respectively, before the measurements of the sand properties were conducted.
- In the third suite, sand aliquots (approx. 1 kg) were treated in a muffle furnace at temperatures of 225, 330, 390, 435, 540, 645 or 750°C for 24 hours. After the heat treatment the sand mixture was remoistened with 3 wt.% water and mingled.

As a reference, untreated sand was used, which was dried once in a drying chamber at 120°C for 24 hours, moistened to 3 wt.%, and mingled. This single drying and moistening is indispensable to define the initial amount of water exactly. After the final moistening, all samples were aged for at least 24 hours in airtight bags before performing analyses.

5.2.2 Methods

The dehydration behaviour of heat pre-treated and cyclically reused Ca-bentonited bonded sands were investigated at the neutron diffraction beam line MIRA (FRM II, Heinz-Maier-Leibnitz-Zentrum, Germany; Georgii & Seemann (2015), Georgii et al. (2018)) in order to allocated the water in the smectite interlayers or the pore space. Moist sands (3wt.% H_2O) were filled into aluminium vials (Ø 18 mm, height 50 mm) and compressed with 1 MPa. The vials were immediately closed with a lid. For pressure release by venting air and water vapour, the lid had a hole (Ø 3 mm). Through a second hole, a thermocouple (Ø 2 mm) was placed in the centre of the sample. The semi-open vial design imitates the conditions within the moulding sand during casting, where ambient pressure is fairly maintained in the open pore system by transport of air and water vapour away from the hot mould cavity towards the neighbouring colder areas.

The filled vial was heated by a furnace mounted on the instrument. In-situ neutron diffraction was applied to measure the d_{001} peak of smectite from room temperature to

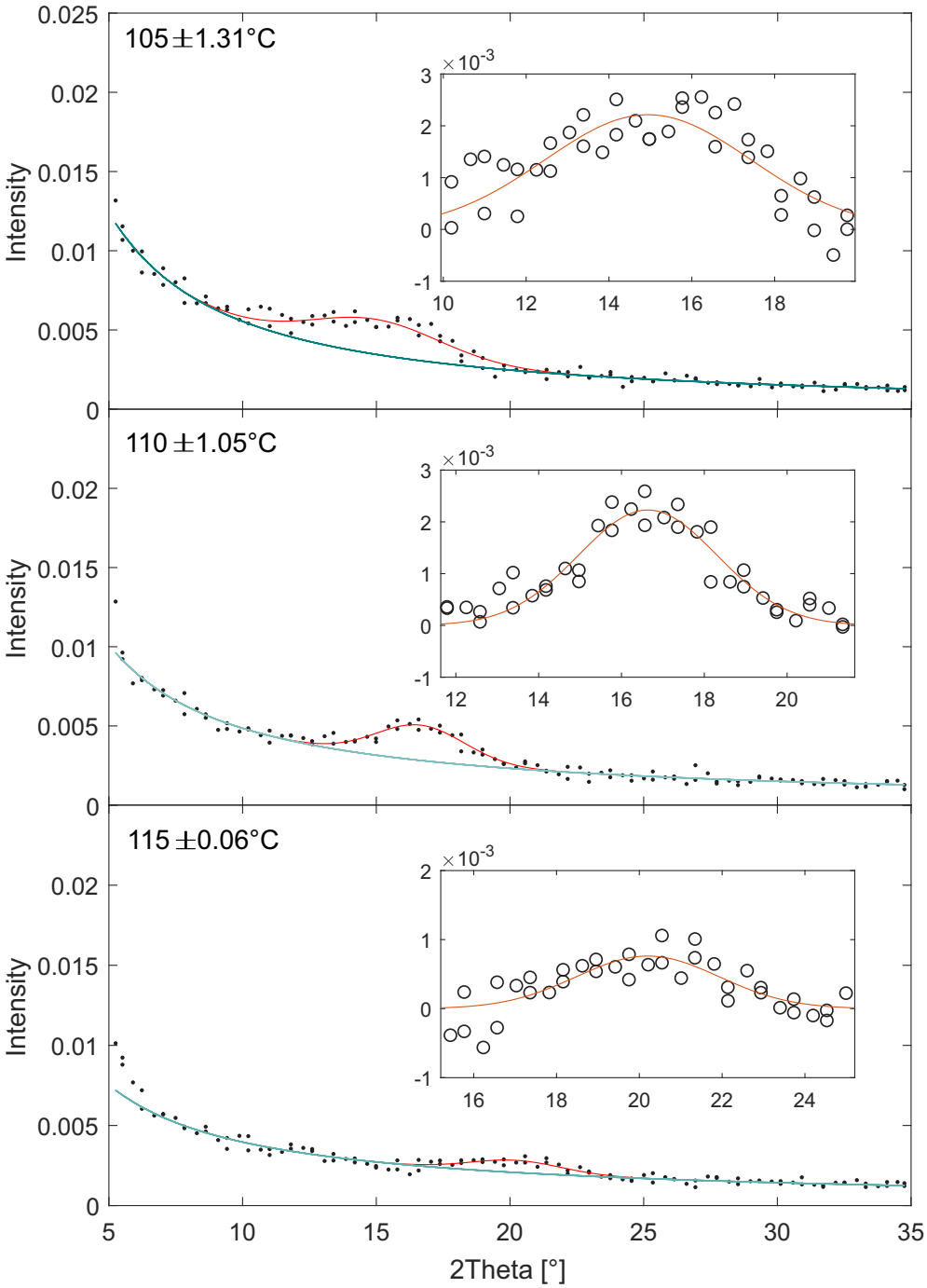

Fig. 5.1: Diffraction patterns of the reference Ca-bentonite bonded moulding sand taken at 105°C, 110°C and 115°C. The background fit is indicated by a turquoise line. The fit of the d_{001} peak of smectite is shown by a red line.

135°C. After each distinct heating step, the temperature was held constant to evaluate the swelling state of smectites. During both heating and holding, diffraction patterns were continuously taken at 5-35° two theta with a step width of 0.4° two theta and an exposure time of 2 s. Before heating and at the end of each experiment, diffraction patterns were taken from 5° to 120° two theta. From the quartz peaks positions (determined by basic Gaussian fitting after background subtraction), the wavelength (4.502 $\pm$ 0.009 Å) was calculated. The quartz reflexion data used for the calculation were taken from Ogata et al. (1987)(d_{100} = 4.2277 Å, d_{101} = d_{011} = 3.3230 Å). From each diffraction pattern taken during heating, the average d_{001} value of the smectite was calculated by fitting the diffraction peak with a single Gaussian function (5.1). Before fitting the peak, the background was fitted by an exponential function and subtracted from the diffraction pattern.

5.2.3 Tensile testing

For the determination of the mechanical properties of the calcium bentonite bonded sand both green and wet tensile testing were conducted. The sand specimens were filled into a two-part aluminium square tube. The lower prismatic part has a height of 100 mm and a cross section of 44 mm x 44 mm. The cross section of the upper pyramidal part (height 20 mm) increased from 44 mm x 44 mm to 54 mm x 54 mm (Fig.2.1). The two-part tube was filled from the bottom by turning the tube (Fig.2.1) upside down. The sand was sieved into the turned tube and compressed with 1 MPa.

Before wet tensile testing was conducted, a temperature and moisture gradient was induced in the tensile specimens by heating them from above with a heating plate (T = 310°C). After a defined heating period (120 or 180 s), tensile load was applied (loading ramp 50 N/s) and the tearing force was measured. The tensile strength σ_t was calculated by the quotient of tearing tension to the sectional area of the specimen neck according to Eqn.1.

5.2.4 Neutron radiography

Experiments were conducted at ICON (SINQ, Paul Scherrer Institute, Switzerland; Kaestner et al. (2011)) and ANTARES (FRM II, Heinz-Maier-Leibnitz-Zentrum, Germany; Schulz & Schillinger (2015)). The entire heating and tensile testing experiments were imaged successively in order to follow the water kinematics and to determine location and moisture of the rupture plane within the sand column. At ICON, samples with cyclically dried and remoistened sands were investigated using a CMOS camera (4 frames/s, spatial resolution = 0.05 mm/pixel). At ANTARES, tensile tests of heat pre-treated sands and different initial moistures were conducted using a CCD camera (0.55 frames/s, 2x2 binning, spatial resolution = 0.15 mm/pixel).

The radiographs were corrected for white and dark spots, background noise, and beam fluctuation according to the work of Hassanein et al. (2006). Within each radiography,

the local water content was calculated for each pixel according to Schiebel et al. (2017) by:

$$w(x,y,t) = \left(ln\left(\frac{\tau_s^{cor}}{g(y)}\right) - ln\left(\frac{\tau(x,y,t)^{cor}}{g(y)}\right)\right) / \Theta_W \tag{5.1}$$

where $w(x,y,t)$ is the water content w at pixel position x, y and time t. τ^{cor} is the corrected intensity of the transmitted neutron beam; τ_s^{cor} is the corrected transmission of the beam transmitting the dry sand; Θ_W is the correlation factor between water content and neutron transmission calculated from calibration measurements (Schiebel et al. 2017); $g(y)$ is the sample geometry normalisation factor, which takes account for the specific geometry of the two-part specimen tube.

In each radiograph, the local amount of water was measured a long a vertical profile in the centre of the sample tube. In each profile, the boundary between evaporation and condensation zone was assigned to the moisture maximum. The boundary between condensation and external zone was assigned to the first position with a constant water content following the maximum. The position of the boundary between dry and evaporation zone was assigned to the location of a water content of zero, which was most distant from the heating plate.

From the determined zone boundaries the propagation constants q of the zone boundaries were calculated according to Equation 3.6.

5.3 Results and comparison to Na-bonded sands

5.3.1 Sands with different initial water contents

Rupture position

Independent of the water content and the bentonite composition, the location of rupture can be pinpointed at the boundary between evaporation and condensation zone, where the temperature is exactly 100°C.

Water kinematics

The dependence of the water kinematics on initial moisture content within Ca-bentonite bonded sands was largely similar compared to Na-bentonite bonded sands (Fig. 5.2). The propagation constant of the boundary between dry zone and evaporation zone as well as the propagation constant of the boundary between evaporation zone and condensation zone stayed almost unchanged with an increasing initial water content. In contrast, the propagation of the boundary between condensation zone and external zone increased independent of the bentonite type. However, the degree of the increase of the propagation constant differed. While for Ca-bentonite bonded sand the propagation constant increased from approx. 1.9 mm/$\sqrt{}$t at 2 wt.% water to 3.4 mm/$\sqrt{}$t at 8 wt.%

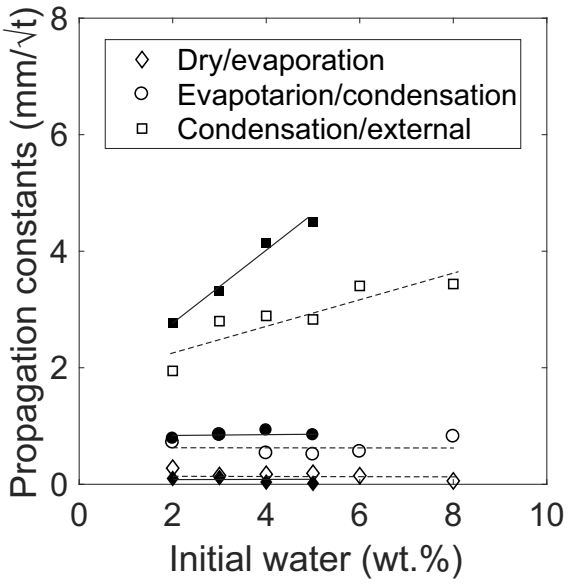

Fig. 5.2: Propagation constants of zone boundaries in moulding sands with different initial moisture contents. Filled dots denote Na-bentonite bonded sands, empty dots Ca-bentonite bonded sands.

water, the propagation constant of the sand containing Na-bentonite increased much faster from 2.7 mm/$\sqrt{}$t at 2 wt.% water to 4.5029 mm/$\sqrt{}$t at 5 wt.% water.

The maximum water content increased from 4.4 wt% (initial water 2 wt.%) to 11 wt.% (initial water 8 wt.%) (Fig. 5.3) in Ca-bentonite bonded sands. The linear increase in maximum water content was similar to the behaviour of Na-bentonite bonded sand.

5.3.2 Cyclically reused sands

Tensile strength

The wet tensile strengths of the reference Ca-bentonite bonded sand as well as of cyclic reused Ca-bentonite bonded sand were approximately 4.5 kN/m^2 and, therefore, 1 kN/m^2 lower than of Na-bonded sands of the same bentonite content and moisture (Fig.5.4). Like in the Na-bentonite bonded sand no substantial changes in the wet tensile strength could be observed with an increasing number of drying-remoistening cycles. The wet tensile strength stayed constant at around 4.5 kN/m^2.

Water kinematics

With an increased number of drying and remoistening cycles, no significant changes in the water kinematics could be observed. Both, the movement of the zone boundaries 5.5 (0.1 mm/$\sqrt{}$s boundary dry/evaporation zone; 0.75 mm/$\sqrt{}$s boundary evaporation/condensation zone; 3 mm/$\sqrt{}$s boundary condensation/external zone) and the maximum water content in the condensation zone (Fig. 5.6) stayed unchanged with an increasing number of drying and remoistening cycles. Thereby, the behaviour of the propagation constants and the maximum water contents of Ca-bentonite bonded sand and Na-bentonite bonded sand was identical.

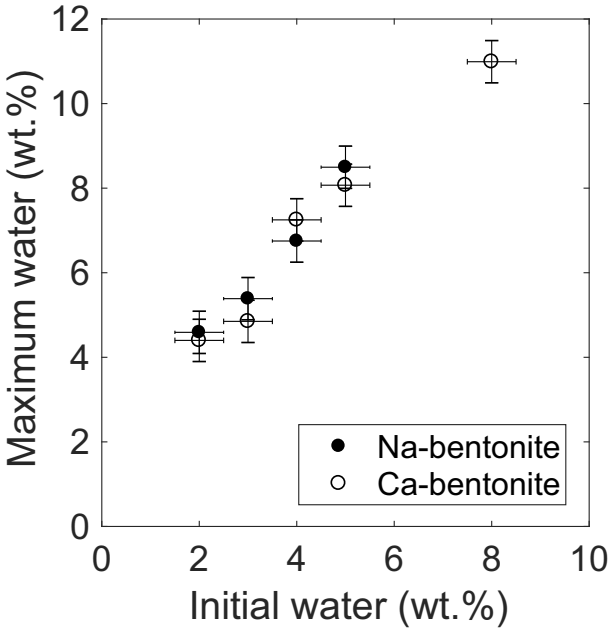

Fig. 5.3: Measured maximum water contents of Na-bentonite bonded sands (filled symbols) and Ca-bentonite bonded sand (empty symbols) versus initial moisture.

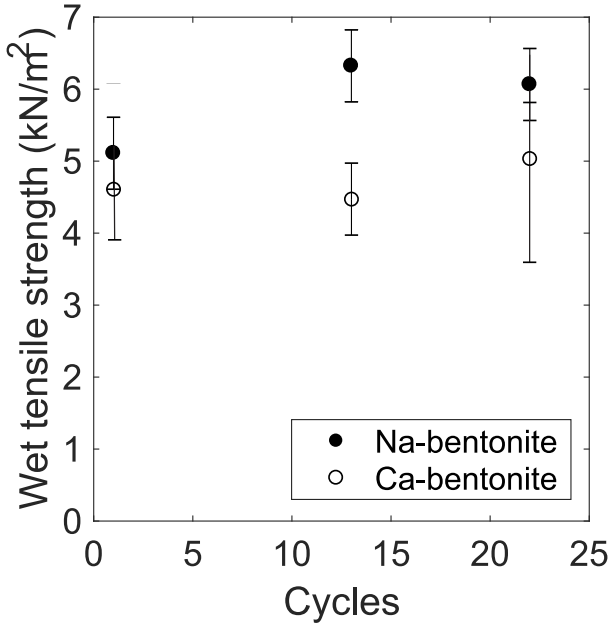

Fig. 5.4: Wet tensile strengths of bentonite bonded sands subjected to various numbers of drying-remoistening cycles. Filled dots denote Na-bentonite bonded sands, empty dots Ca-bentonite bonded sands

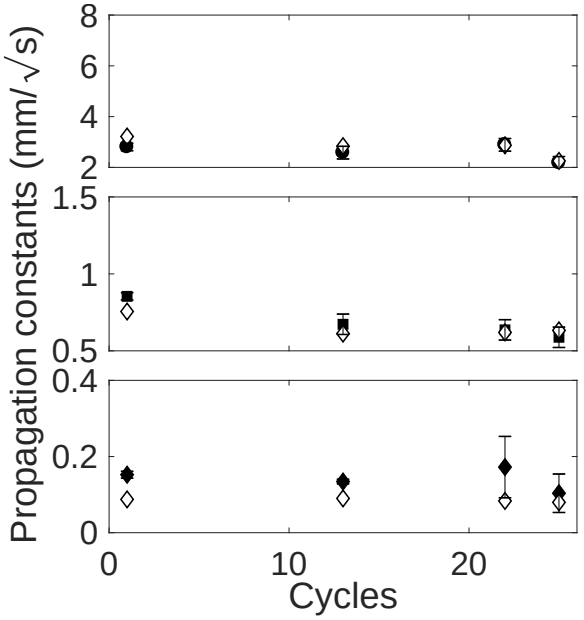

Fig. 5.5: Propagation constants of the zone boundaries calculated from neutron radiographs of cyclically reused sands plotted versus the number of cycles. a) Boundary of condensation zone and external zone; b) Boundary of evaporation zone and condensation zone; c) Boundary of dry zone and evaporation zone. Filled dots denote Na-bentonite bonded sands, empty dots Ca-bentonite bonded sands.

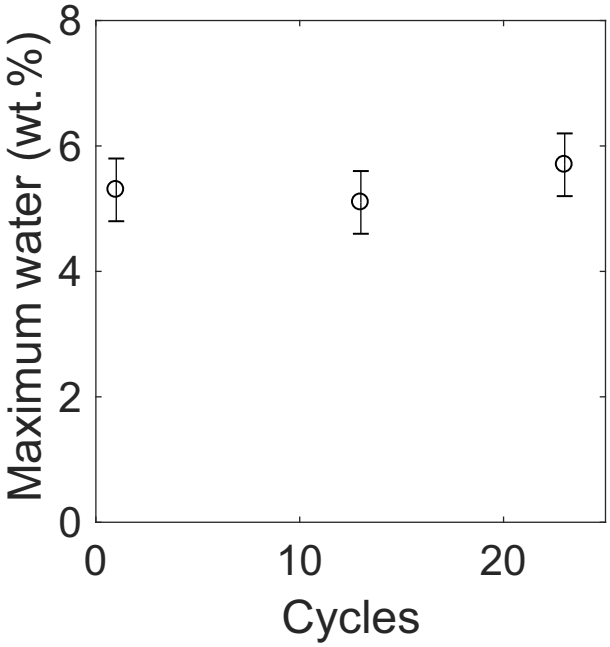

Fig. 5.6: Maximum water content versus number of drying-moistening cycles of Ca-bentonite bonded sands.

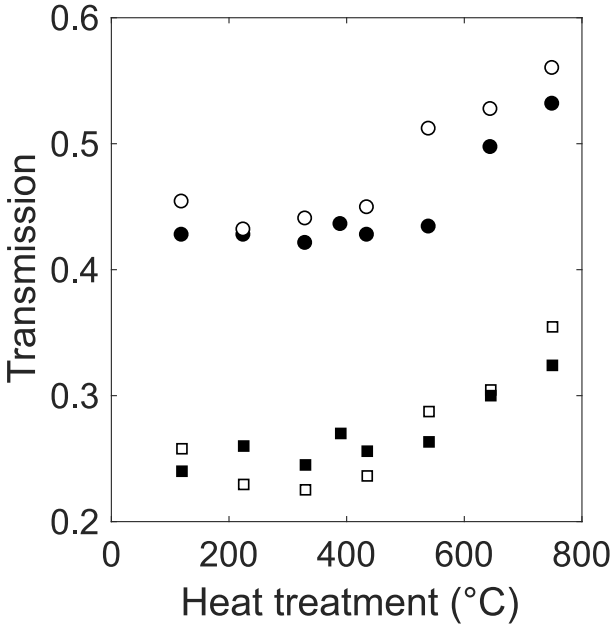

Fig. 5.7: Initial (squares) and maximum (dots) neutron transmission of Ca-bentonite bonded sand (empty symbols) and Na-bentonite bonded sand (filled symbols) depending on the temperature of the pre-treatment. The maximum transmission corresponds to the transmission of the dry sand next to the heating plate in the uppermost region of the sand column.

5.3.3 Heat pre-treated sands

Dehydroxylation

In the radiographs, the maximum neutron transmission corresponds to the transmission of the dehydrated sand in the upper part of the sand column next to the heating plate. The maximum transmission as well as the initial transmission increase with the release of any hydrogen by the smectites. Therefore, the initial and maximal transmission allow assumptions about the dehydroxylation state of the smectites of the heat pre-treated sands. The initial and the maximum transmission stayed unchanged up to a pre-treatment temperature of 435°C (Fig. 5.7). However, from 435°C to 750°C both, an increase of the initial as well as of the maximum neutron transmission could be observed, indicating a loss of OH-groups by the smectites. While for Ca-bonded sands, an increase of the initial and maximal transmission could be observed beginning at 435°C, the first increase in Na-bentonite bonded sands could be detected at 540°C portending on a release of the OH-groups at higher temperature.

Sand structure

In the SEM images of the reference Ca-bentonite bonded sand, it can be seen clearly that the quartz grains are completely covered with smectite. The covering film interconnects neighbouring quartz grains, which build a three-dimensional framework embedding the quartz grains. Compared to the Na-smectites of the moulding sand investigated in chapter 4, the Ca-smectites are bigger in size and adhere on the quartz grains worse. The framework formed by the Ca-smectites looks more fragmentary than the framework formed by Na-smectites (Fig. 5.8). Ca-bentonite bonded sands pre-treated with a temperature of 540°C still have a three dimensional smectite framework but the quartz

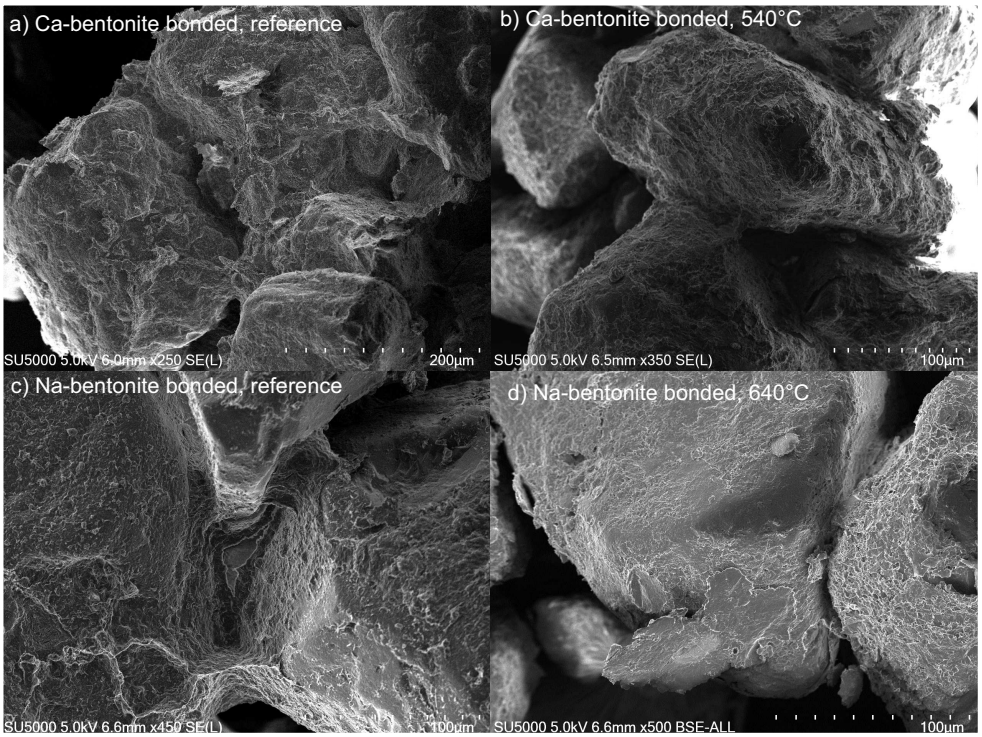

Fig. 5.8: SEM images of air-dried sand. a) Reference Ca-bentonite bonded sand; b) Ca-bentonite bonded sand pre-treated at 645°C. c) Reference Na-bentonite bonded sand; d) Na-bentonite bonded sand pre-treated at 645°C.

grains seem to be covered by the smectite less perfectly and the smectites seem to be less voluminous and less homogeneously distributed.

Ca-bentonite bonded sands as well as Na-bentonite bonded sands that have been pre-treated with temperatures of 645°C and higher lack the interconnecting three-dimensional framework. Consequently, these heat pre-treated sands were composed of quartz grains, which were connected only partially.

Interlayer water

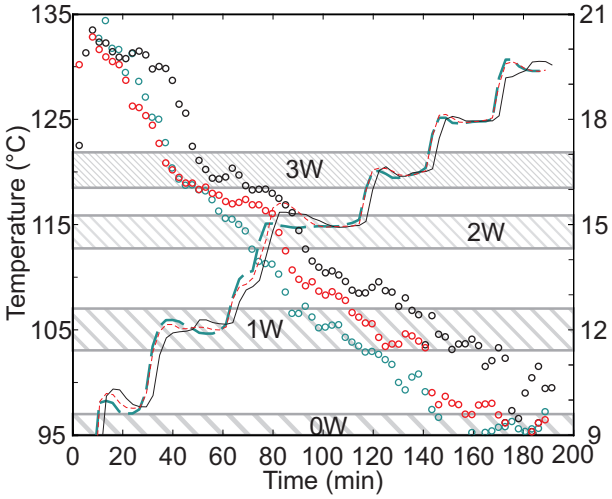

Fig. 5.9: Neutron diffractometer analyses conducted during thermal dehydration of the reference sand (black), sand pre-treated at 225°C (red), and sand pre-treated at 435°C (turquoise). The d_{001} values of smectite (empty circles) and sample temperature (line) are plotted versus time. The grey shaded areas indicate the ranges of d_{001} values, which, according to literature, are associated with smectites containing 0, 1, 2, and 3 layers of water within the smectite interlayer.

The temperature dependent d_{001} values were determined in-situ by exposing heat pre-treated samples to increasing temperatures within the neutron diffractometer. The initial d_{001} values of Ca-montmorillonite in the reference sand as well as in sands pre-treated with 225°C and 435°C were approx. 19.4 Å (Fig. 5.9). According to Collins et al. (1992) these *d* values correspond to three layers of interlayer water but after Zheng et al. (2010) these *d* values indicate an amount of water exceeding three layers. With an increase in temperature, the *d* values discontinuously decreased with the release of interlayer water. Independent of the heat pre-treatment of the samples, heating to 100°C and holding the temperature in the diffractometer for around 30 minutes caused no significant decrease of the d_{001} values.

Heating to 105°C and holding the temperature in the diffractometer for almost half an hour resulted in a continuous decrease of the *d* values down to approx. 16 Å for sands pre-treated at temperatures up to 435°C. These values correspond to three layers of water (Zheng et al. 2010). With increasing diffractometer temperature, the *d* values of the reference sand and the sand pre-treated at 225°C stayed unchanged until temperature in the diffractometer reached 115°C. In contrast, the *d* values of sand pre-treated at 435°C instantaneously decreased from approx. 16 Å to 12 Å when the diffractometer temperature exceeded 105°C. At the end of the 115°C holding period, the *d* values of all three samples (reference as well as samples pre-treated at 225°C and 435°C) reached a plateau that corresponded to one layer of water (Collins et al. 1992, Ferrage et al. 2007,

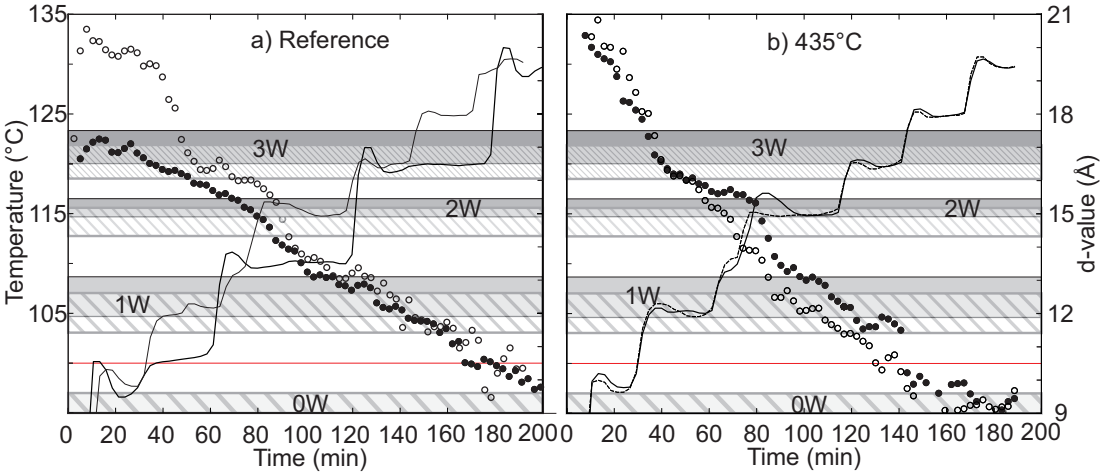

Fig. 5.10: Neutron diffractometer analyses conducted during thermal dehydration of the reference sand (a) and sand pre-treated at 435°C (b). The d_{001} values of smectite (filled circles for Na-bentonite bonded sand, empty circles for Ca-bentonite bonded sand) and sample temperature (solid lines Na-bentonite bonded sand, dashed lines for Ca-bentonite bonded sand) are plotted versus time. The red lines mark the 100°C levels and illustrate the periods of the sample temperature exceeding 100°C. The grey areas indicate the ranges of d_{001} values, which, according to literature, are associated with smectites containing 0, 1, 2, and 3 layers of water (from bright to dark greyscales) within the smectite interlayer for Na-bentonite bonded sand. The grey shaded areas indicate the ranges of d_{001} values, which, according to literature, are associated with smectites containing 0, 1, 2, and 3 layers of water (from slightly to heavily shaded) within the smectite interlayer for Na-bentonite bonded sand.

Zheng et al. 2010).For higher pre-treatment temperatures, the *d* values measured under the same conditions were significantly smaller.

Finally, heating the sand specimens within the diffractometer to 130°C, the 001-reflections disappeared in the background with final *d* values of approximately 10 Å for the reference sand and 9.5 Å for the pre-treated sands, indicating the complete dehydration of the smectites (Collins et al. 1992, Ferrage et al. 2007, Zheng et al. 2010).

Compared to not pre-treated Na-bentonite bonded sands, the initial *d* values of all Ca-bentonite bonded sands were bigger (Fig. 5.10 a). At diffractometer temperatures of 100°C, the different *d* values were still evident. Heating the samples in the diffractometer up to 105°C, different *d* values between Na- and Ca-bonded could not be detected any longer. If a heat pre-treatment was performed, the behaviour of the *d* values with increasing temperature was quite similar for both Ca- and Na-bentonite bonded sands (Fig. 5.10 b), and even the initial *d* values were of the same magnitude.

Tensile strength

For sand heat pre-treated at 330°C, the wet tensile strength decreased from of 4.7 kN/m^2 to 2.4±0.4 kN/m^2. The wet tensile strength stayed unchanged at 2.8±0.4 kN/m^2 with an increasing pre-treatment temperature up to 435°C. Pre-treating the sand at 540°C, a

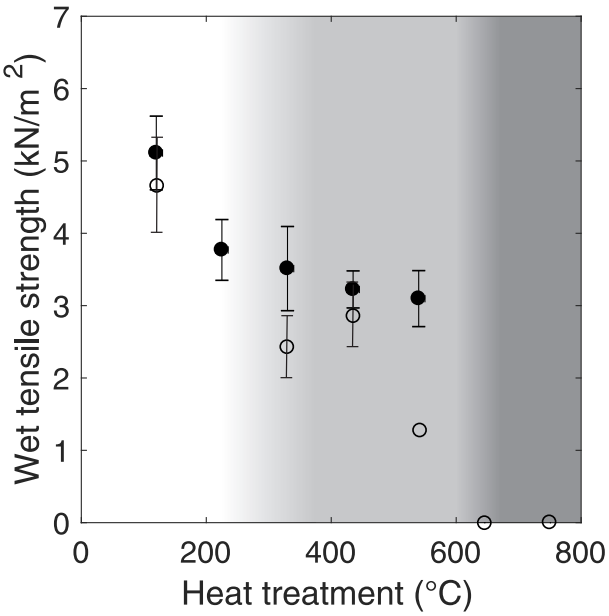

Fig. 5.11: Wet tensile strengths of bentonite bonded sands pre-treated at different temperatures. Filled dots denote Na-bentonite bonded sands, empty dots Ca-bentonite bonded sands. Different degrees of smectite dehydroxylation (Fig.4.2) are indicated by different greyscales.

second decrease of the wet tensile strength down to 1.2 kN/m^2 was measurable. Pre-treatments with temperatures above 645°C caused a decrease of the tensile strengths below the detection limit and a movement of the position of rupture into the dry zone. value Therefore, the behaviour of the wet tensile strength with temperature of Ca-bentonite bonded sand is comparable to the behaviour of Na-bonded sand. Only the decrease in tensile strength for Ca-bonded sands pre-treated at 540°C could not be detected in Na-bonded sand.

Water kinematics

Compared to Na-bentonite bonded sands, the water kinematics of Ca-bentonite bonded sands changed considerably with higher pre-treatment temperatures. While an increase of all propagation constants could be observed for pre-treated Na-bentonite bonded sands (particularly at temperatures of 645°C and higher) none of the propagation constants of Ca-bonded sand changed significantly with an increasing pre-treatment temperature. The propagation constants of Ca-bentonite bonded sand were approximately 0.1 mm/$\sqrt{}$s (boundary of dry zone and evaporation zone), 0.75 mm/$\sqrt{}$s (boundary of evaporation zone and condensation zone), and 3 mm/$\sqrt{}$s (boundary of condensation zone and external zone). Only an increase of the propagation constant of the boundary between the evaporation zone and condensation zone from 0.9 to 1.1 mm/$\sqrt{}$s starting at a temperature pre-treatment of 435°C could be detected.

Just as the dependence of the propagation constants on pre-treatment temperature, no change in the maximum water amount (occurring at the boundary between dry zone and evaporation zone) could be observed.

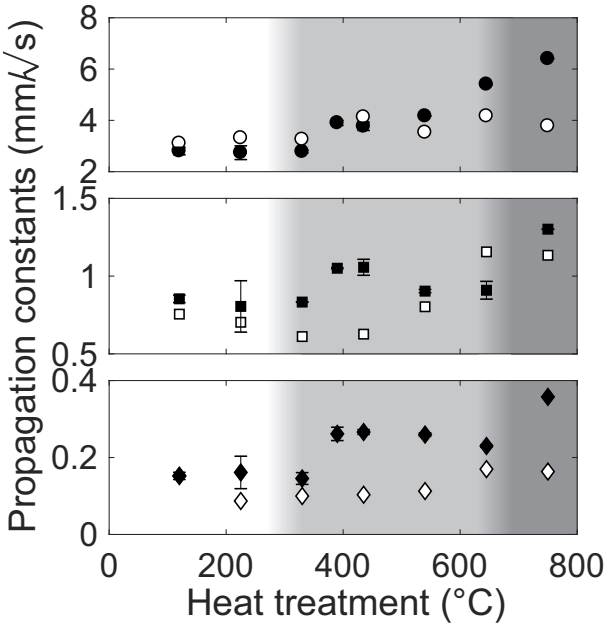

Fig. 5.12: Propagation constants of the zone boundaries calculated from neutron radiographs of heat pre-treated moulding sands plotted versus pre-treatment temperature. a) Boundary of condensation zone and external zone; b) Boundary of evaporation zone and condensation zone; c) Boundary of dry zone and evaporation zone. Filled dots denote Na-bentonite bonded sands, empty dots Ca-bentonite bonded sands. Different degrees of smectite dehydroxylation are indicated by different greyscales.

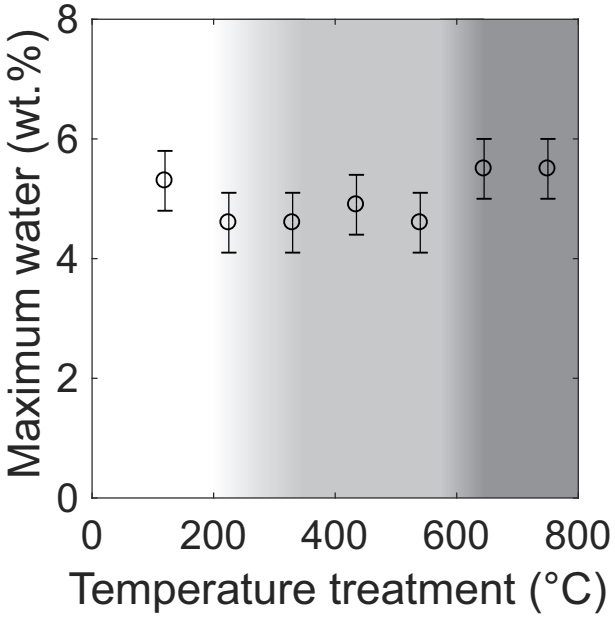

Fig. 5.13: Maximum water content versus temperature of the heat pre-treatment. Different degrees of smectite dehydroxylation are indicated by different greyscales.

5.4 Discussion

5.4.1 Sands with different initial water contents

At the boundary between the evaporation zone and condensation zone, the water content reaches a maximum (w_{max}). This maximum water content is predominantly controlled by the heat capacity of the moulding sand (Kubo & Pehlke 1986, Patterson & Boenisch 1961*a*).

$$w_{max} = w_0 + (w_0 C_w + (1 - w_0) C_s) \frac{373 - T_0}{L_W} \tag{5.2}$$

where w_0 is the initial water, C_W the specific heat of water (approx. 4.2 kJ/(kg K)), C_s the specific heat of moulding sand, T_0 the initial temperature, and L_W the latent evaporation heat (kJ/kg). Since the changes in the bentonite composition did barely influence the specific heat of the sand, the maximum water contents of (not pre-treated and not reused) Ca-bentonite bonded and Na-bentonite bonded sands do not differ from each other significantly.

However, the heat capacity of the moulding sand increases with increasing initial moisture and causes an increase of the heat flux (Fan & Wen 2002). This relation can be regarded as the reason for the increased movement of the condensation zone front (Popielarski & Ignaszak 2016).

5.4.2 Cyclically reused sands

Neither significant changes of the propagation constants (Fig. 5.5) nor changes in tensile strength (Fig. 5.6) could be observed with an increasing number of drying and remoistening cycles. This observation for Ca-bentonite corresponds well to the results of Na-bentonite bonded sand. A strong impact of steam on the montmorillonite structure and on its swelling behaviour such as postulated by Couture (1985) and Oscarson & Dixon (1989), therefore, could not be confirmed by this experiments.

5.4.3 Heat pre-treated sands

Differences in the interlayer water

At a temperature of 100°C within the diffractometer the d_{001} values of the smectites of the reverence sand and of sands pre-treated with 225°C or 435°C were of the same size. This indicates that the d_{001} value and, consequently, the swelling capacity are not the main factors being responsible for the decrease in tensile strength, which was observed for the pre-treated sands.

In contrast to the initial swelling state, sands heat pre-treated at temperatures of up to 225°C revealed a significantly increased rate of water release (Fig. 5.9). This increased water release rate may be caused by a decrease of the layer charge (Juhász 1989). Such a reduction in layer charge has been suggested to be caused by an irreversible migration

of small interlayer cations (such as Li, Cu, Zn) into the tetrahedral layers (McBride & Mortland 1974) or the octahedral sites (Madejová et al. 1996). Although larger cations (Na, Ca) are less likely migrating into these sites (Calvet & Prost 1971), a minor amount of migration maybe sufficient for the changes of water release rates as observed here. The increased rate of water release of sands heat pre-treated at temperatures of 435°C (Fig. 5.9) is likely a consequence of dehydroxylation, which has been reported to take place ar temperatures of approx. 300-750°C (Földvári 2013).

The comparison of heat pre-treated Ca-bentonite and Na-bentonite bonded sands at 435°C revealed a slightly faster dehydration for the Ca-bentonite bonded sands above 105°C (Fig. 5.10b). This slightly faster release rate may reflect a slightly different diffusivity of water molecules within the smectite interlayers above 105 °C (c.f. Zabat & Van Damme 2000).

Water kinematics

The fact that the water kinematics of Ca-bentonite bonded sands did not change with increasing pre-treatment temperatures is remarkable. The neutron diffraction data showed that the water release of the smectites changed with higher pre-treatment temperatures. However, the increased release rate was not reflected by a change of the propagation constants. The boundary movement neither between the dry zone and evaporation zone nor between the evaporation zone and condensation zone changed. In addition, no major changes in the propagation constant of the boundary between condensation zone and external zone could be observed. Thus, the steam absorption and adsorption rates seemed to remain unchanged. A reason for this might be the higher specific surface area of the altered Ca-smectites as observed in the SEM analyses (Fig. 5.8. This larger specific surface area may provide more adsorption sites compared to Na-smectites. This higher site-density may allow the steam to condensate on the pre-treated Ca-smectite surfaces more rapidly than on the respective Na-smectites surfaces. It has to be noted, however, that the heat pre-treatment exerted no influence on the amount of maximum water at the boundary between evaporation and condensation zone. This is not remarkable, as the smectite alteration caused by the heat pre-treatment has no strong influence on the specific heat of the entire moulding sand.

Differences in tensile strength

Even if the general behaviour of the tensile strength on increasing pre-treatment temperatures was similar for both Na- and Ca-bentonite bonded sands, the strong decrease of tensile strength at 540°C in Ca-bentonite bonded sand stands out. This decrease corresponds well with the observed increase in initial neutron transmission of Ca-bentonite bonded sand at 540°C (Fig. 5.7), caused by a loss of hydrogen of the smectites which cannot be observed in Na-bentonite bonded sands. The observed loss of hydrogen is concomitant to a decreased layer charge of the smectites, which leads to a decrease of the water sorption energy (Juhász 1989) and, consequently, to a decrease of the wet tensile strength. Because dehydroxylation of Ca-smectites, differently to Na-smectites,

is a pronounced two-step reaction (Földvári 2013), wet tensile strength of Ca-bentonite bonded sand decreased in a stepwise manner (Fig. 5.11), too.

5.4.4 Higher tensile strength of Na-bentonite bonded sands

In general, the wet tensile strength of Ca-bentonite bonded sand is lower than of Na-bentonite bonded sand (Fig. 5.11), (Patterson & Boenisch 1961*a*). Patterson & Boenisch (1961*a*) and Odom (1984) mentioned that the reason for this different tensile strength lies in the different arrangement of water. In Na-rich montmorillonites, water is arranged in a more ordered and rigid way than in in Ca-rich montmorillonites. However, the higher order of water molecules in Na-montmorillonites could not be confirmed by (Sposito & Prost 1982). Furthermore, the observation of Pons et al. (1980) that the structure of water within Na-montmorillonite and Ca-montmorillonite is predominantly liquid-like contradicts the postulations of Odom (1984) and Patterson & Boenisch (1961*a*).

At the temperature of the rupture plane (100°C) in tensile strength testing, both Ca- and Na-bentonite bonded sands did show similar smectite d-001 values and, therefore, similar water release behaviour of the smectites. The observed differences in wet tensile strength (Fig. 5.11), thus, cannot be related to different dehydration behaviour of these different smectites. The maximum water content at the boundary between evaporation and condensation zone remained unchanged with both pre-treatment temperature (Fig. 5.13) and bentonite composition (Fig. 5.3). Therefore, changes in the capillary strength due to major changes in the saturation can also be excluded as causes for the different tensile strengths.

Anyhow, the diffusion of water molecules in and out of the smectite interlayers ($\approx 9 \cdot 10^{-9}$ $m^2 s^{-1}$ Bourg & Sposito (eg 2010), Holmboe & Bourg (eg 2013)) is orders of magnitudes smaller than the propagation of the boundary of the evaporation zone and condensation zone ($\approx 8 \cdot 10^{-7}$ $m^2 s^{-1}$; Fig. 5.5). Therefore, absorption capacity of the smectite plays an inferior role in buffering the rising supersaturation at the boundary between evaporation and condensation zone.

Besides hydration of interlayer cations, water can adsorb on the external surfaces of the smectites and can condense in moulding sand micropores. Prost (1975) showed that the fraction of smectite surface covered by water molecules at a given water content depends strongly on the nature of the interlayer cation. The larger the solvation energy of the cation, the larger is the hydration of the surfaces. The wettability of Na-montmorillonites, therefore, is smaller than for Ca-montmorillonites. This lower wettability causes an increased in the strength of the clay bridges and, consequently, leads to a higher green and wet tensile strength of Na-bentonite bonded sands.

At water content within the smectite interlayers corresponding to less than three layers, the arrangement of the water molecules surrounding the exchangeable cations depends mainly on the type of cations. Studies on water structure Hertz & Franks (1973) and Enderby & Neilson (1981) show that the mean residence time of a water molecule in the first solvation layer around a monovalent cation like Na^+ is about 10^{-11}

s. Around bivalent cations like Ca^{2+}, the residence time is about 10^{-8} s. In bulk water the residence time in the first layer is about 10^{-12} s. Therefore, a further reason for the better performance of Na-bentonite bonded sands might be that higher release rate of water from the interlayer space of Na-montmorillonites at 100°C can contribute to a slight delay of the evaporation the capillary bridges.

6 Conclusions

6.1 Effect of moisture on the sand properties

Neutron radiography imaging was successfully applied to follow wet tensile strength testing in-situ during heat application. Radiography enabled for both quantification of the water kinematics and determination of the location of lowest strength in the moisture profile. The preferred fracture position was pinpointed at the boundary between evaporation and condensation zone. This location of minimum tensile strength could be explained by the negative correlation of the surface tension of water and temperature (Kayser 1976), which reaches minimum value at 100°C. Additionally, the onset of the boiling of the water within the water bridges lowers the capillary force further and leads to the observed minimum of tensile strength (Fig. 6.1). The results refute common postulations (Odom 1984, Campbell 2011, Patterson & Boenisch 1961*a*) that the fracture is located within the condensation zone and is exclusively caused by the supersaturation of the sand.

6.2 Effect of heat pre-treatment and cyclic reuse on the properties of Na-bentonite bonded sand

Although there were small differences in the d_{001} values of smectites between the reference sand and sands subjected to 22 drying and remoistening cycles, significant changes in water kinematics and tensile strength could not be detected. Thus, the observed effects caused by the cyclic reuse were not yet strong enough to affect the attractive forces in a magnitude leading to a substantial reduction of the quality of the moulding sand. This finding agrees with empiric practice in foundry industry, where moulding sand is replaced after approx. 20 cycles. The fact that slight alterations were detected, however, may indicate that a higher number of cycles eventually will lead to a decrease of sand quality. In this context, it needs to be noted that in our experiments the maximum temperature during cyclic reuse was 120°C. A high-temperature impact, as it typically occurs during casting, was not part of these cycles.

The influences of heat pre-treatment on the water transport and binding properties of moulding sands were investigated for the first time. Alterations were detected already at T = 225°C, i.e. at a temperature, which supposedly is well below the dehydroxylation threshold of smectites. The alterations mainly comprised of an increased water transport

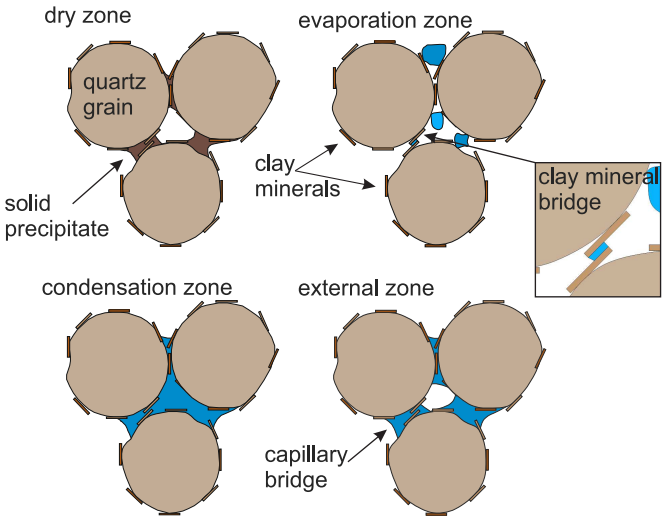

Fig. 6.1: Illustration of the different transport zones. The Quartz grains in the dry zone were connected by a solid precipitate which had been formed after the water was evaporated. In the evaporation zone, the quartz grains were hold together by clay mineral bridges. In the condensation zone and the external zone, capillary bridges were mainly responsible for the cohesion of the quartz grains. With increasing saturation, the bridges merged and the capillary forces decreased

rate in the moulding sand column. We suggest that this modified water kinematics is a consequence of minor changes of the compositional and structural integrity of the smectites and is causally related to the observed degradation of the mechanical properties of the moulding sands. Upon an early dehydroxylation of the the smectites or a progressive release of tightly bound water at $T > 330$°C, further irreversible decrease of the binding quality of moulding sands occurred. With completing dehydroxylation of the smectites above 670°C, the total loss of wet tensile strength of the pre-heated sands took place.

6.3 Ca-bentonite bonded sands

Different behaviour of Ca- and Na-bentonite bonded moulding sands was detected after heat pre-treatment. The detected differences in tensile strength correspond well with the different dehydroxylation behaviour of the smectites. In contrast, the maximum water content and the smectite swelling capacity seem not to be among the major causes responsible for the change in tensile strength. Ca- and Na-bentonite bonded moulding sands did not show significant differences in the maximum water content at high pre-treatment temperatures. Differences in swelling capacity at pre-treatment temperatures below 545°C likely are too low for a significant impact on the tensile strength. Close to the heat source, moreover, the propagation rate of the water in the condensation zone is likely too fast for the smectites to absorb significant amounts of the incoming water and steam.

Acknowledgements

The work is based upon experiments performed at ANTARES and MIRA operated by Heinz Maier-Leibnitz Zentrum (MLZ, Garching Germany) as well as at ICON (Paul-Scherrer-Institute, Villigen, Switzerland). Funding from DFG (JO301/5-1) is gratefully acknowledged. Furthermore, the I would like to kindly thank Erika Grießhaber (LMU München) for SEM analyses. Gratefully acknowledged are the mineralogical and chemical analyses of the bentonite performed by Helge Stanjek (RWTH Aachen). I thank Sandra Böhmke providing the moulding sand on behalf of S&B minerals. Furthermore, I appreciate the DSC and TG measurements performed by Kai-Uwe Hess, and thank him and W.W. Schmahl for there great suggestions helping to improve the manuscript and this work. My warm thanks go to Sophie Wunderlich and especially to Guntram Jordan, working together with you was a pleasure.

Appendix

Pretreatment		Water amount (wt.%)		Tensile strength (kN/m^2)		Porosity	Saturation	
Cycles	Temperature	Initial	Maximal	Green	Wet		Initial	Maximal
1	120	2	4.6	5.0	1.5	0.46	0.06	0.14
1	120	3	5.4	12.3	5.4	0.47	0.08	0.15
1	120	4	6.8	10.4	6.7	0.48	0.11	0.18
1	120	5	8.5	8.9	6.8	0.49	0.13	0.22
1	120	3	5.5	/	5.1	0.47	0.09	0.17
1	225	3	4.8	/	3.8	0.47	0.09	0.14
1	330	3	5.5	/	3.6	0.48	0.09	0.15
1	435	3	6.1	/	3.2	0.47	0.09	0.18
1	540	3	5.7	/	3.1	0.45	0.09	0.17
1	645	3	4.7	/	0.0	0.48	0.09	0.14
1	750	3	5.2	/	0.0	0.52	0.08	0.13
1	120	3	4.7	/	5.1	0.46	0.06	0.14
13	120	3	5.0	/	6.3	0.45	0.8	0.16
22	120	3	4.9	/	6.0	0.44	0.7	0.17
24	120	3	/	/	/	0.46	0.9	0.15

Table 1: Tensile strength and saturation of moulding sands bonded with natural sodium bentonite from Wyoming

Pretreatment		Water amount (wt.%)		Tensile strength (kN/m^2)		Porosity	Saturation	
Cycles	Temperature	Initial	Maximal	Green	Wet		Initial	Maximal
1	120	2	4.4	/	/	0.43	0.05	0.11
1	120	3	4.9	/	/	0.45	0.09	0.15
1	120	5	7.3	/	/	0.44	0.13	0.19
1	120	8	11.1	/	/	0.45	0.16	0.22
1	120	3	5.5	/	/	0.46	0.08	0.15
1	225	3	5.3	/	/	0.43	0.07	0.12
1	330	3	4.8	/	2.4	0.42	0.08	0.13
1	435	3	6.1	/	2.9	0.41	0.07	0.14
1	540	3	5.7	/	1.1	0.42	0.08	0.15
1	645	3	4.7	/	0	0.42	0.07	0.11
1	750	3	5.2	/	0	0.47	/	/
13	120	3	5.3	/	6.3	0.42	0.07	0.12
22	120	3	5.1	/	6.0	0.42	0.08	0.14
24	120	3	5.7	/	/	/	0.07	0.13

Table 2: Tensile strength and saturation of moulding sands bonded with natural calcium bentonite from Bavaria

Pretreatment		Water amount (wt.%)		Propagation constants (mm/$\sqrt{s}$)		
Cycles	Temperature (°C)	Initial	Maximal	Dry/Evaporation	Evaporation/Condensation	Condensation External
1	120	2	4.5	0.10	0.79	2.77
1	120	3	5.3	0.11	0.84	3.32
1	120	4	6.9	0.03	0.92	4.15
1	120	5	8.4	0.01	0.85	4.50
1	120	3	5.5	0.15	0.85	2.80
1	225	3	5.3	0.16	0.80	2.73
1	330	3	4.8	0.15	0.83	2.78
1	390	3	5.9	0.26	1.05	3.90
1	435	3	6.1	0.27	1.06	3.77
1	540	3	5.7	0.26	0.9	4.17
1	645	3	4.7	0.23	0.9	5.40
1	750	3	5.2	0.36	1.3	6.40
13	120	3	/	0.17	0.59	2.58
22	120	3	/	0.13	0.67	2.89
24	120	3	/	0.15	0.85	2.18

Table 3: Propagation constants of moulding sands bonded with natural sodium bentonite from Wyoming

Pretreatment		Water amount (wt.%)		Propagation constants (mm/$\sqrt{s}$)		
Cycles	Temperature (°C)	Initial	Maximal	Dry/Evaporation	Evaporation/Condensation	Condensation External
1	120	2	4.4	0.28	0.78	1.95
1	120	3	4.9	0.11	0.53	2,8
1	120	4	7.9	0.17	0.51	2.89
1	120	5	7.3	0.19	0.53	2.83
1	120	6	8.1	0.15	0.56	4.40
1	120	8	11	0.06	0.82	3.43
1	120	3	5.5	0.15	0.76	3.10
1	225	3	5.3	0.09	0.61	3.31
1	330	3	4.8	0.09	0.70	3.25
1	435	3	6.1	0.10	0.63	4.13
1	540	3	5.7	0.11	0.80	3.53
1	645	3	4.7	0.17	1.156	4.17
1	750	3	5.2	0.16	1.13	3.78
13	120	3	5.3	0.09	0.61	2.84
22	120	3	5.1	0.08	0.62	2.89
24	120	3	5.7	0.08	0.63	2.18

Table 4: Propagation constants of quartz sands bonded with natural calcium bentonite from Bavaria

Bibliography

Alonso-Santurde, R., Coz, A., Viguri, J. & Andrés, A. (2012), 'Recycling of foundry by-products in the ceramic industry: Green and core sand in clay bricks', *Construction and Building Materials* **27**(1), 97–106.

Anthony, J. W., Bideaux, R. A., Bladh, K. W. & Nichols, M. C. (2000), 'Handbook of mineralogy, volume IV, arsenates, phosphates, vanadates', *1-680, Mineralogical Society of America, Chantilly, Virginia* .

Barry, M. M., Jung, Y., Lee, J.-K., Phuoc, T. X. & Chyu, M. K. (2015), 'Fluid filtration and rheological properties of nanoparticle additive and intercalated clay hybrid bentonite drilling fluids', *Journal of Petroleum Science and Engineering* **127**, 338–346.

Barshad, I. (1949), 'The nature of lattice expansion and its relation to hydration in montmorillonite and vermiculite', *The American Mineralogist* **34**(9-10), 675–684.

BDG (1997), VDG - Merkblatt p38: Prüfung von tongebundenen Formstoffen Bestimmung der Festigkeit, Technical report, Bundesverband der Deutschen Gießerei-Industrie BDG.

Beer, A. (1852), 'Bestimmung der Absorption des rothen Lichts in farbigen Flüssigkeiten', *Ann. Physik* **162**, 78–88.

Bergaya, F. & Lagaly, G. (2006), 'General introduction: clays, clay minerals, and clay science', *Developments in clay science* **1**, 1–18.

Bird, P. (1984), 'Hydration-phase diagrams and friction of montmorillonite under laboratory and geologic conditions, with implications for shale compaction, slope stability, and strength of fault gouge', *Tectonophysics* **107**(3-4), 235–260.

Bobrowski, A. & Grabowska, B. (2012), 'The impact of temperature on furan resin and binders structure', *Metallurgy and Foundry Engineering* **38**, 73–80.

Boon, J. J., Hendrickx, R., Eijkel, G., Cerjak, I., Kaestner, A. & Ferreira, E. S. B. (2015), 'Neutron radiography for the study of water uptake in painting canvases and preparation layers', *Applied Physics A* **121**(3), 837–847.

Bourg, I. C. & Sposito, G. (2010), 'Connecting the molecular scale to the continuum scale for diffusion processes in smectite-rich porous media', *Environmental Science & Technology* **44**(6), 2085–2091.

Bragg, W. H. & Bragg, W. L. (1913), 'The reflection of X-rays by crystals', *Proceedings of the Royal Society of London. Series A, Containing Papers of a Mathematical and Physical Character* **88**(605), 428–438.

Bray, H. & Redfern, S. (1999), 'Kinetics of dehydration of Ca-montmorillonite', *Physics and Chemistry of Minerals* **26**(7), 591–600.

Calvet, R. & Prost, R. (1971), 'Cation migration into empty octahedral sites and surface properties of clays', *Clays and Clay Minerals* **3**, 175–186.

Campbell, J. (2011), *Complete Casting Handbook, 1st Edition*, Elsevier.

Carslaw, H. S. & Jaeger, J. C. (1959), 'Conduction of heat in solids', *Oxford: Clarendon Press, 1959, 2nd ed.* .

Chorom, M. & Rengasamy, P. (1996), 'Effect of heating on swelling and dispersion of different cationic forms of a smectite', *Clays and Clay Minerals* **44**(6), 783–790.

Christidis, G. E., Blum, A. E. & Eberl, D. (2006), 'Influence of layer charge and charge distribution of smectites on the flow behaviour and swelling of bentonites', *Applied Clay Science* **34**(1), 125–138.

Collins, D. R., Fitch, A. N. & Catlow, C. R. A. (1992), 'Dehydration of vermiculites and montmorillonites: a time-resolved powder neutron diffraction study', *Journal of Materials Chemistry* **2**(8), 865–873.

Couture, R. A. (1985), 'Steam rapidly reduces the swelling capacity of bentonite', *Nature* **318**(6041), 50–52.

Dobbs, H. & Yeomans, J. (1992), 'Capillary condensation and prewetting between spheres', *Journal of Physics: Condensed Matter* **4**(50), 10133.

Drits, V., Besson, G. & Muller, F. (1995), 'An improved model for structural transformation of heat-treated aluminous dioctahedral 2: 1 layer silicates', *Clays and Clay Minerals* **43**(6), 718–731.

Einstein, A. (1916), 'Die Grundlage der Allgemeinen Relativitätstheorie', *Annalen der Physik* **354**(7), 769–822.

Emmerich, K. (2000), *Die geotechnische Bedeutung des Dehydroxylierungsverhaltens quellfähiger Tonminerale*, Vol. 13508, vdf Hochschulverlag AG.

Emmerich, K. & Kahr, G. (2001), 'The cis-and trans-vacant variety of a montmorillonite: an attempt to create a model smectite', *Applied Clay Science* **20**(3), 119–127.

Emmerich, K., Koeniger, F., Kaden, H. & Thissen, P. (2015), 'Microscopic structure and properties of discrete water layer in Na-exchanged montmorillonite', *Journal of Colloid and Interface Science* **448**, 24 – 31.

Emmerich, K., Madsen, F. T. & Kahr, G. (1999), 'Dehydroxylation behavior of heat-treated and steam-treated homoionic *cis*-vacant montmorillonites', *Clays and Clay Minerals* **47**(5), 591–604.

Emmerich, K., Wolters, F., Kahr, G. & Lagaly, G. (2009), 'Clay profiling: the classification of montmorillonites', *Clays and Clay Minerals* **57**(1), 104–114.

Enderby, J. & Neilson, G. (1981), 'The structure of electrolyte solutions', *Reports on Progress in Physics* **44**(6), 593.

Falode, O., Ehinola, O. & Nebeife, P. (2008), 'Evaluation of local bentonitic clay as oil well drilling fluids in Nigeria', *Applied Clay Science* **39**(1-2), 19–27.

Fan, J. & Wen, X. (2002), 'Modeling heat and moisture transfer through fibrous insulation with phase change and mobile condensates', *International Journal of Heat and Mass Transfer* **45**(19), 4045–4055.

Ferrage, E., Kirk, C. A., Cressey, G. & Cuadros, J. (2007), 'Dehydration of Ca-montmorillonite at the crystal scale. Part I: Structure evolution', *American Mineralogist* **92**(7), 994–1006.

Ferrage, E., Lanson, B., Michot, L. J. & Robert, J.-L. (2010), 'Hydration properties and interlayer organization of water and ions in synthetic Na-smectite with tetrahedral layer charge. Part 1. Results from X-ray diffraction profile modeling', *The Journal of Physical Chemistry C* **114**(10), 4515–4526.

Fiore, S. & Zanetti, M. C. (2007), 'Foundry wastes reuse and recycling in concrete production', *American Journal of Environmental Sciences* **3**(3), 135–142.

Fischer, W. (1997), 'Sinq—the spallation neutron source, a new research facility at PSI', *Physica B: Condensed Matter* **234**, 1202–1208.

Fisher, R. (1926), 'On the capillary forces in an ideal soil; correction of formulae given by wb haines', *The Journal of Agricultural Science* **16**(3), 492–505.

Földvári, M. (2013), 'Handbook of the thermogravimetric system of minerals and its use in geological practice: Occasional papers of the Geological Institute of Hungary, vol. 213, Budapest, 2011, 180 p.'.

Forsmo, S., Apelqvist, A., Björkman, B. & Samskog, P.-O. (2006), 'Binding mechanisms in wet iron ore green pellets with a bentonite binder', *Powder Technology* **169**(3), 147–158.

Georgii, R. & Seemann, K. (2015), 'Mira: Dual wavelength band instrument', *Journal of Large-Scale Research Facilities JLSRF* **1**, 3.

Georgii, R., Weber, T., Brandl, G., Skoulatos, M., Janoschek, M., Mühlbauer, S., Pfleiderer, C. & Böni, P. (2018), 'The multi-purpose three-axis spectrometer (TAS) MIRA at FRM II', *Nuclear Instruments and Methods in Physics Research Section A: Accelerators, Spectrometers, Detectors and Associated Equipment* **881**, 60–64.

Gražulis, S., Chateigner, D., Downs, R. T., Yokochi, A. F. T., Quirós, M., Lutterotti, L., Manakova, E., Butkus, J., Moeck, P. & Le Bail, A. (2009), 'Crystallography Open Database – an open-access collection of crystal structures', *Journal of Applied Crystallography* **42**(4), 726–729.

Gražulis, S., Daskevic, A., Merkys, A., Chateigner, D., Lutterotti, L., Quirós, M., Serebryanaya, N. R., Moeck, P., Downs, R. T. & Le Bail, A. (2012), 'Crystallography open database (cod): an open-access collection of crystal structures and platform for world-wide collaboration', *Nucleic Acids Research* **40**(D1), D420–D427.

Greene-Kelly, R. (1955), 'Dehydration of montmorillonite minerals', *Mineralogical Magazine* **30**(228), 604–615.

Grim, R. E. & Guven, N. (1978), *Bentonites - Geology, mineralogy, properties and uses*, Elsevier, Amsterdam.

Guney, Y., Sari, Y. D., Yalcin, M., Tuncan, A. & Donmez, S. (2010), 'Re-usage of waste foundry sand in high-strength concrete', *Waste Management* **30**(8), 1705–1713.

Haines, W. B. (1925), 'Studies in the physical properties of soils: Ii. a note on the cohesion developed by capillary forces in an ideal soil', *The Journal of Agricultural Science* **15**(4), 529–535.

Hall, S. A. (2013), 'Characterization of fluid flow in a shear band in porous rock using neutron radiography', *Geophysical Research Letters* **40**(11), 2613–2618.

Hassanein, R. (2006), Correction methods for the quantitative evaluation of thermal neutron tomography, PhD thesis, Swiss Federal Institute of Technology Zürich.

Hassanein, R., Meyer, H. O., Carminati, A., Estermann, M., Lehmann, E. & Vontobel, P. (2006), 'Investigation of water inbibition in porous stone by thermal neutron radiography', *Journal of Physics D: Applied Physics* **39**, 4284–4291.

Hasse, S. (2007), *Giesserei-Lexikon 2008*, Fachverlag Schiele & Schoen.

Heibrock, G., Zeh, R. M. & Witt, K. J. (2005), Tensile strength of compacted clays, *in* T. Schanz, ed., 'Unsaturated Soils: Experimental Studies', Springer, Berlin, pp. 395–412.

Heller-Kallai, L. & Rozenson, I. (1980), 'Dehydroxylation of dioctahedral phyllosilicates', *Clays Clay Minerals* **28**(5), 355.

Hendricks, S. B. & Jefferson, M. E. (1938), 'Structures of kaolin and talc-pyrophyllite hydrates and their bearing on water sorption of the clays', *American Mineralogist* **23**, 863–875.

Hertz, H. & Franks, F. (1973), 'Water: A comprehensive treatise', *by F. Franks, Plenum Press, New York* **3**.

Heuser, M., Weber, C., Stanjek, H., Chen, H., Jordan, G., Schmahl, W. W. & Natzeck, C. (2014), 'The interaction between bentonite and water vapor. I: Examination of physical and chemical properties', *Clays and Clay Minerals* **62**(3), 188–202.

Hofmann, U. & Klemen, R. (1950), 'Verlust der Austauschfähigkeit von Lithiumionen an Bentonit durch Erhitzung', *Zeitschrift für anorganische und allgemeine Chemie* **262**(1-5), 95–99.

Holmboe, M. & Bourg, I. C. (2013), 'Molecular dynamics simulations of water and sodium diffusion in smectite interlayer nanopores as a function of pore size and temperature', *The Journal of Physical Chemistry C* **118**(2), 1001–1013.

Holtzer, M., Bobrowski, A. & Żymankowska-Kumon, S. (2011), 'Temperature influence on structural changes of foundry bentonites', *Journal of Molecular Structure* **1004**(1), 102–108.

Hubbell, J. H. & Seltzer, S. M. (1995), Tables of X-ray mass attenuation coefficients and mass energy-absorption coefficients 1 keV to 20 MeV for elements z= 1 to 92 and 48 additional substances of dosimetric interest, Technical report, National Inst. of Standards and Technology-PL, Gaithersburg, MD (United States). Ionizing Radiation Div.

Israelachvili, J. N. (2011), *Intermolecular and surface forces*, Academic press.

Jordan, G., Eulenkamp, C., Calzada, E., Schillinger, B., Hoelzel, M., Gigler, A., Stanjek, H. & Schmahl, W. W. (2013), 'Quantitative in-situ study of the dehydration of bentonite-bounded moulding sands', *Clays and Clay Minerals* **61**(2), 133–144.

Juhász, A. (1989), 'Water vapor adsorption and capillary reactions of silicates', *Colloid & Polymer Science* **267**(11), 1036–1054.

Kaestner, A., Hartmann, S., Kühne, G., Frei, G., Grünzweig, C., Josic, L., Schmid, F. & Lehmann, E. (2011), 'The ICON beamline – a facility for cold neutron imaging at SINQ', *Nuclear Instruments and Methods in Physics Research Section A: Accelerators, Spectrometers, Detectors and Associated Equipment* **659**(11), 387–393.

Kaestner, A., Lehmann, E. & Stampanoni, M. (2008), 'Imaging and image processing in porous media research', *Advances in Water Recources 31* pp. 1174–1187.

Kang, M., Bilheux, H., Voisin, S., Cheng, C., Perfect, E., Horita, J. & Warren, J. (2013), 'Water calibration measurements for neutron radiography: Application to water content quantification in porous media', *Nuclear Instruments and Methods in Physics Research Section A: Accelerators, Spectrometers, Detectors and Associated Equipment* **708**, 24–31.

Kayser, W. V. (1976), 'Temperature dependence of the surface tension of water in contact with its saturated vapor', *Journal of Colloid and Interface Science* **56**(3), 622–627.

Khanna, S. & Swarup, D. (1961), 'The role of wet-tensile strength of foundry sands in the surface finish of aluminium sand casting'.

Kohonen, M. M., Geromichalos, D., Scheel, M., Schier, C. & Herminghaus, S. (2004), 'On capillary bridges in wet granular materials', *Physica A: Statistical Mechanics and its Applications* **339**(1-2), 7–15.

Komadel, P., Madejová, J. & Bujdák, J. (2005), 'Preparation and properties of reduced-charge smectites–a review', *Clays and Clay Minerals* **53**(4), 313–334.

Kubo, K. & Pehlke, R. D. (1986), 'Heat and moisture transfer in sand molds containing water', *Metallurgical Transactions B* **17**(4), 903–911.

Kuligiewicz, A. & Derkowski, A. (2017), 'Tightly bound water in smectites', *American Mineralogist* **102**(5), 1073–1090.

Laird, D. A. (2006), 'Influence of layer charge on swelling of smectites', *Applied Clay Science* **34**(1-4), 74–87.

Laird, D. A., Shang, C. & Thompson, M. L. (1995), 'Hysteresis in crystalline swelling of smectites', *Journal of Colloid and Interface Science* **171**(1), 240–245.

Lambert, J. H. (1760), *Photometria sive de mensura et gradibus luminis, colorum et umbrae*, Klett.

Lechman, J., Lu, N. & Wu, D. (2006), 'Hysteresis of matric suction and capillary stress in monodisperse disk-shaped particles', *Journal of Engineering Mechanics* **132**(5), 565–577.

Lian, G., Thornton, C. & Adams, M. J. (1993), 'A theoretical study of the liquid bridge forces between two rigid spherical bodies', *Journal of Colloid and Interface Science* **161**(1), 138–147.

Likos, W. J. & Lu, N. (2004), 'Hysteresis of capillary stress in unsaturated granular soil', *Journal of Engineering Mechanics* **130**(6), 646–655.

Lindner, M., Nagle, R. & Landrum, J. (1976), 'Neutron capture cross sections from 0.1 to 3 MeV by activation measurements', *Nuclear Science and Engineering* **59**(4), 381–394.

Loto, C. & Adebayo, H. (1990), 'Effects of variation in water content, clay fraction and sodium carbonate additions on the synthetic moulding properties of igbokoda clay and silica sand', *Applied Clay Science* **5**(2), 165–181.

Lu, N., Godt, J. W. & Wu, D. T. (2010), 'A closed-form equation for effective stress in unsaturated soil', *Water Resources Research* **46**(5).

Lu, N., Kim, T.-H., Sture, S. & Likos, W. J. (2009), 'Tensile strength of unsaturated sand', *Journal of engineering mechanics* **135**(12), 1410–1419.

Lu, N., Wu, B. & Tan, C. P. (2007), 'Tensile strength characteristics of unsaturated sands', *Journal of Geotechnical and Geoenvironmental Engineering* **133**(2), 144–154.

MacEwan, D. M. & Wilson, M. (1980), 'Interlayer and intercalation complexes of clay minerals', *Crystal structures of clay minerals and their X-ray identification* **5**, 197–248.

Madejová, J., Bujdák, J., Komadel, P. & Gates, W. (1996), 'Preparation and infrared spectroscopic characterization of reduced-charge montmorillonite with various Li contents', *Clay Minerals* **31**(2), 233–241.

Maeda, N., Israelachvili, J. N. & Kohonen, M. M. (2003), 'Evaporation and instabilities of microscopic capillary bridges', *Proceedings of the National Academy of Sciences* **100**(3), 803–808.

Maes, A. & Cremers, A. (1977), 'Charge density effects in ion exchange. part 1.—heterovalent exchange equilibria', *Journal of the Chemical Society, Faraday Transactions 1: Physical Chemistry in Condensed Phases* **73**, 1807–1814.

McBride, M. & Mortland, M. (1974), 'Copper (II) interactions with montmorillonite: Evidence from physical methods', *Soil Science Society of America Journal* **38**(3), 408–415.

Mehrotra, V. & Sastry, K. (1980), 'Pendular bond strength between unequal-sized spherical particles', *Powder Technology* **25**(2), 203–214.

Melcher, R. E. & Schaefer, F. W. (1978), 'Additive for green molding sand'. US Patent 4,131,476.

Mering, J. (1946), 'On the hydration of montmorillonite', *Transactions of the Faraday Society* **42**, B205–B219.

Molenkamp, F. & Nazemi, A. (2003), 'Interactions between two rough spheres, water bridge and water vapour', *Geotechnique* **53**(2), 255–264.

Momma, K. & Izumi, F. (2008), 'Vesta: a three-dimensional visualization system for electronic and structural analysis', *Journal of Applied Crystallography* **41**(3), 653–658.

Momma, K. & Izumi, F. (2011), 'Vesta 3 for three-dimensional visualization of crystal, volumetric and morphology data', *Journal of Applied Crystallography* **44**(6), 1272–1276.

Munkholm, L. J. & Kay, B. D. (2002), 'Effect of water regime on aggregate-tensile strength, rupture energy, and friability', *Soil Science Society of America Journal* **66**, 702–709.

Odom, I. E. (1984), 'Smectite clay minerals: Properties and uses', *Philosophical Transactions of the Royal Society of London A: Mathematical, Physical and Engineering Sciences* **311**(1517), 391–409.

Ogata, K., Takeuchi, Y. & Kudoh, Y. (1987), 'Structure of α-quartz as a function of temperature and pressure', *Zeitschrift für Kristallographie-Crystalline Materials* **179**(1-4), 403–414.

Orr, F., Scriven, L. & Rivas, A. P. (1975), 'Pendular rings between solids: meniscus properties and capillary force', *Journal of Fluid Mechanics* **67**(4), 723–742.

Oscarson, D. & Dixon, D. (1989), 'The effect of steam on montmorillonite', *Applied Clay Science* **4**(3), 279–292.

Oscarson, D., Dixon, D. & Gray, M. (1990), 'Swelling capacity and permeability of an unprocessed and a processed bentonitic clay', *Engineering Geology* **28**(3-4), 281–289.

Paluszkiewicz, C., Holtzer, M. & Bobrowski, A. (2008), 'FTIR analysis of bentonite in moulding sands', *Journal of Molecular Structure* **880**(1-3), 109–114.

Parappagoudar, M., Pratihar, D. & Datta, G. (2008), 'Neural network-based approaches for forward and reverse mappings of sodium silicate-bonded, carbon dioxide gas hardened moulding sand system', *Materials and Manufacturing Processes* **24**(1), 59–67.

Patterson, W. & Boenisch, D. (1961*a*), 'Die Bedeutung der Festigkeit feuchter, tongebundener Formsande insbesondere der Naßfestigkeit', *Giesserei* **3**, 157–193.

Patterson, W. & Boenisch, D. (1961*b*), 'Eigenschaften und Eigenschaftsänderungen der Tonmineralien in Formsanden', *Forschungsberichte des Landes Nordrhein-Westfalen* **961**.

Patterson, W. & Boenisch, D. (1964), 'Das Schülpendiagramm für Naßzugsande', *Giesserei* **51**(21), 634–641.

Patterson, W. & Boenisch, D. (1966), 'Die Wasserbindung an Tonen und ihre Bedeutung für die Festigkeit des Gießereiformsandes', *Forschungsberichte des Landes Nordrhein-Westfalen* **1659**.

Pierrat, P. & Caram, H. S. (1997), 'Tensile strength of wet granula materials', *Powder Technology* **91**(2), 83–93.

Pons, C., Brahim, J. B., Yucel, A., Tchoubar, D. & Tchoubar, C. (1980), 'Détermination à l'échelle absolue de l'intensité diffractée aux rayons x par les argiles', *Clay Minerals* **15**(2), 111–120.

Popielarski, P. & Ignaszak, Z. (2016), *Drying and Energy Technologies*, Springer International Publishing, Cham, chapter Effective Modelling of Phenomena in Over-Moisture Zone Existing in Porous Sand Mould Subjected to Thermal Shock, pp. 181–206.

Prost, R. (1975), Interactions between adsorbed water molecules and the structure of clay minerals: Hydration mechanism of smectites, *in* 'Proc. 5th Int. Clay Conf., Mexico City', p. 353.

Rabinovich, Y. I., Esayanur, M. S. & Moudgil, B. M. (2005), 'Capillary forces between two spheres with a fixed volume liquid bridge: theory and experiment', *Langmuir* **21**(24), 10992–10997.

Raupp-Pereira, F., Hotza, D., Segadães, A. & Labrincha, J. (2006), 'Ceramic formulations prepared with industrial wastes and natural sub-products', *Ceramics International* **32**(2), 173–179.

Schiebel, K., Jordan, G., Kaestner, A., Schillinger, B., Boehnke, S. & Schmahl, W. W. (2017), 'Neutron radiographic study of the effect of heat-driven water transport on the tensile strength of bentonite-bonded moulding sand', *Transport in Porous Media* . **URL:** *https://doi.org/10.1007/s11242-017-0968-z*

Schiebel, K., Jordan, G., Kaestner, A., Schillinger, B., Boehnke, S. & Schmahl, W. W. (2018), 'Neutron radiographic study of the effect of heat-driven water transport on the tensile strength of bentonite-bonded moulding sand', *Transport in Porous Media* **121**(2), 369–387.

Schillinger, B., Calzada, E., Eulenkamp, C., Jordan, G. & Schmahl, W. W. (2011), 'Dehydration of moulding sand in simulated casting process examined with neutron radiography', *Nuclear Instruments and Methods in Physics Research Section A: Accelerators, Spectrometers, Detectors and Associated Equipment* **651**(1), 312–314.

Schillinger, B., Calzada, E. & Lorenz, K. (2006), 'Modern neutron imaging: Radiography, tomography dynamic and phase contrast imaging with neutrons', *Solid State Phenomena* **112**, 66–72.

Schnetzer, F., Thissen, P., Giraudo, N. & Emmerich, K. (2016), 'Unraveling the coupled processes of (de) hydration and structural changes in Na_+-saturated montmorillonite', *The Journal of Physical Chemistry C* **120**(28), 15282–15287.

Schröder, A. & Macherauch, E. (1977), 'Zur Temperaturverteilung in strahlungsbeheizten ebenen Formdecken aus tongebundenem Quartzsand', *Giessereiforschung* **29**(1), 41–46.

Schubert, H. (1968), 'Experimentelle Bestimmung von Haftkraft und Randwinkel am System einer Flüssigkeitsbrücke zwischen zwei Kugeln', *Chemie Ingenieur Technik* **40**(15), 745–747.

Schultz, L. G. (1969), 'Lithium and potassium absorption, dehydroxylation temperature, and structural water content of aluminous smectites', *Clays and Clay Minerals* **17**(3), 115–149.

Schulz, M. & Schillinger, B. (2015), 'Antares: Cold neutron radiography and tomography facility', *Journal of Large-Scale Research Facilities* **1**(A17), 1–4.

Sears, V. F. (1992), 'Neutron scattering lengths and cross sections', *Neutron News* **3**(3), 26–37.
URL: *https://doi.org/10.1080/10448639208218770*

Sedighi-Gilani, M., Wakili, K. G., Koebel, M., Hugi, E., Carl, S. & Lehmann, E. (2013), 'Visualizing moisture realese and migration in gypsum plaster board during and beyond dehydration by neutron radiography', *International Journal of Heat and Mass Transfer* **60**, 248–290.

Shokri, N., Lehmann, P., Vontobel, P. & Or, D. (2008), 'Drying front and water content dynamics during evaporation from delineated by neutron radiography', *Water resources research* **44**, W06418.

Shokri, N. & Or, D. (2013), 'Drying patterns of porous media containing wettabillity contrasts', *Journal of Colloid and Interface Science* **391**, 135–141.

Siddique, R., De Schutter, G. & Noumowe, A. (2009), 'Effect of used-foundry sand on the mechanical properties of concrete', *Construction and Building Materials* **23**(2), 976–980.

Song, Y.-S., Hwang, W.-K., Jung, S.-J. & Kim, T.-H. (2012), 'A comparative study of suction stress between sand and silt under unsaturated conditions', *Engineering Geology* **124**, 90–97.

Sposito, G. & Prost, R. (1982), 'Structure of water adsorbed on smectites', *Chemical Reviews* **82**(6), 553–573.

Starobin, A., Hirt, T., Lang, H. & Todte, M. (2011), 'Core drying simulation and validation', *American Foundry Society Proceedings* **11-28**, 1–5.

Tang, C.-S., Pei, X.-J., Wang, D.-Y., Shi, B. & Li, J. (2015), 'Tensile strength of compacted clayey soil', *Journal of Geotechnical and Geoenvironmental Engineering* **141**(4), 04014122.

Teich-McGoldrick, S. L., Greathouse, J. A., Jove-Colon, C. F. & Cygan, R. T. (2015), 'Swelling properties of montmorillonite and beidellite clay minerals from molecular simulation: comparison of temperature, interlayer cation, and charge location effects', *The Journal of Physical Chemistry C* **119**(36), 20880–20891.

Thirumalai, K., Singh, A. & Ramesh, R. (2011), 'A matlab^{TM} code to perform weighted linear regression with (correlated or uncorrelated) errors in bivariate data', *Journal of the Geological Society of India* **77**(4), 377–380.

Udell, K. S. (1983), 'Heat transfer in porous media heated from above with evaporation, condensation, and capillary effects', *Journal of Heat Transfer* **105**(3), 485–492.

Vanicek, I. (2013), 'The importance of tensile strength in geotechnical engineering', *Acta Geotechnica Slovenica* **1**, 5–9.

Villar, M., Gómez-Espina, R. & Gutiérrez-Nebot, L. (2012), 'Basal spacings of smectite in compacted bentonite', *Applied Clay Science* **65**, 95–105.

Villman, B., Slowik, V., Wittmann, F. H., Vontobel, P. & Hovinid, J. (2014), 'Time-dependent moisture distribution in drying cement mortars - results of neutron radiography and inverse analysis of drying tests', *Restoration of Buildings and Monuments* **20**(1), 49–62.

Wang, Y., Huang, H., Cannon, F. S., Voigt, R. C., Komarneni, S. & Furness, J. C. (2007), 'Evaluation of volatile hydrocarbon emission characteristics of carbonaceous additives in green sand foundries', *Environmental Science & Technology* **41**(8), 2957–2963.

Wersin, P., Johnson, L. & McKinley, I. (2007), 'Performance of the bentonite barrier at temperatures beyond 100 C: A critical review', *Physics and Chemistry of the Earth, Parts A/B/C* **32**(8), 780–788.

Wiebe, B., Graham, J., Tang, G. X. & Dixon, D. (1998), 'Influence of pressure, saturation, and temperature on the behaviour of unsaturated sand-bentonite', *Canadian Geotechnical Journal* **35**(2), 194–205.

Wilhelm, P. & Dietmar, B. (1964), 'Device for ascertaining the operational behavior of molding substances'. US Patent 3,159,018.

Wolters, F. & Emmerich, K. (2007), 'Thermal reactions of smectites—relation of dehydroxylation temperature to octahedral structure', *Thermochimica Acta* **462**(1-2), 80–88.

York, D., Evensen, N. M., Martinez, M. L. & De Basabe Delgado, J. (2004), 'Unified equations for the slope, intercept, and standard errors of the best straight line', *American Journal of Physics* **72**(3), 367–375.

Young, F. & Harkins, W. D. (1928), *International Critical Tables of Numerical Data, Physics, Chemistry and Technology*, Vol. 4, McGraw-Hill, New York.

Zabat, M. & Van Damme, H. (2000), 'Evaluation of the energy barrier for dehydration of homoionic (Li, Na, Cs, Mg, Ca, Ba, Al_x $(OH)_y^{z+}$ and La)-montmorillonite by a differentiation method', *Clay Minerals* **35**(2), 357–363.

Zanetti, M. & Godio, A. (2006), 'Recovery of foundry sands and iron fractions from an industrial waste landfill', *Resources, Conservation and Recycling* **48**(4), 396–411.

Zeh, R. M. & Witt, K. J. (2007), 'The tensile strength of compacted clays as affected by suction and soil structure', *Experimental Unsaturated Soil Mechanics* pp. 219–226.

Zheng, Y., Zaoui, A. & Shahrour, I. (2010), 'Evolution of the interlayer space of hydrated montmorillonite as a function of temperature', *American Mineralogist* **95**(10), 1493–1499.

Żymankowska-Kumon, S., Holtzer, M., Olejnik, E. & Bobrowski, A. (2012), 'Influence of the changes of the structure of foundry bentonites on their binding properties', *Materials Science* **18**(1), 57–61.